11-3-2016

Optimal and Miniaturized Strongly Coupled Magnetic Resonant Systems

Hao Hu
Florida International University, hhu005@fiu.edu

DOI: 10.25148/etd.FIDC001209

FLORIDA INTERNATIONAL UNIVERSITY

Miami, Florida

OPTIMAL AND MINIATURIZED STRONGLY COUPLED MAGNETIC RESONANT SYSTEMS

A dissertation submitted in partial fulfillment of

the requirements for the degree of

DOCTOR OF PHILOSOPHY

in

ELECTRICAL ENGINEERING

by

Hao Hu

2016

To: Interim Dean Ranu Jung
College of Engineering and Computing

This dissertation, written by Hao Hu, and entitled Optimal and Miniaturized Strongly Coupled Magnetic Resonant Systems, having been approved in respect to style and intellectual content, is referred to you for judgment.

We have read this dissertation and recommend that it be approved.

_____
Kang K. Yen

_____
Jean H. Andrian

_____
Berrin Tansel

_____
Manos M. Tentzeris

_____
Stavros V. Georgakopoulos, Major Professor

Date of Defense: November 3, 2016.

The dissertation of Hao Hu is approved.

_____
Interim Dean Ranu Jung
College of Engineering and Computing

_____
Andres G. Gil
Vice President for Research and Economic Development
and Dean of the University Graduate School

Florida International University, 2016

DEDICATION

I dedicate this dissertation to my lovely family. Without their love, patience, understanding and support, the completion of this work would never have been possible.

ACKNOWLEDGMENTS

I would like to express my sincerest gratitude to my major professor, Dr. Stavros V. Georgakopoulos, for his excellent guidance and support through my Ph.D. program at FIU. He was always patient and gave me tremendous constructive academic advice for my research. He also provided the most favorable research environment with the latest research tools. His hard-working, gentle and earnest way of life and research sets up a role model for me, and I sincerely thank him for his help and patience during these five important years of my life. I also appreciate Dr. Kang K. Yen, Dr. Jean H. Andrian, Dr. Berrin Tansel, and Dr. Manos M. Tentzeris for serving on my dissertation defense committee and for their illuminating comments.

I am sincerely thankful for my family who encouraged me throughout the research. Thanks for their love, understanding, encouragement and advice. I also thank all the members of FIU Electrical and Computing Engineering Department and special thanks to Shun Yao, Kun Bao, Daerhan Liu, Xueli Liu, John Gibson, Elad Siman Tov, Karina Quintana, Pablo Gonzalez, Dr. Shan Jiang, Dr. Yipeng Qu, Dr. Olutola Jonah, Dr. Xinyu Jin, Dr. Qi Zhou, and Oscar Silveira for their help and friendship.

Finally, I would like to greatly thank the Graduate School of FIU for awarding me the Dissertation Year Fellowship, which supported me in the last year of my Ph.D. research. I would also like to recognize the supported by the National Science Foundation under grant ECCS 1307984, and the Army Research Office under grant W911NF-13-1-0149. I would like to thank the Air Force Office of Scientific Research for their support of this work through ARO grant W911NF-13-1-0149.

ABSTRACT OF THE DISSERTATION

OPTIMAL AND MINIATURIZED STRONGLY COUPLED MAGNETIC RESONANT SYSTEMS

by

Hao Hu

Florida International University, 2016

Miami, Florida

Professor Stavros. V. Georgakopoulos, Major Professor

Wireless power transfer (WPT) technologies for communication and recharging devices have recently attracted significant research attention. Conventional WPT systems based either on far-field or near-field coupling cannot provide simultaneously high efficiency and long transfer range. The Strongly Coupled Magnetic Resonance (SCMR) method was introduced recently, and it offers the possibility of transferring power with high efficiency over longer distances. Previous SCMR research has only focused on how to improve its efficiency and range through different methods. However, the study of optimal and miniaturized designs has been limited. In addition, no multiband and broadband SCMR WPT systems have been developed and traditional SCMR systems exhibit narrowband efficiency thereby imposing strict limitations on simultaneous wireless transmission of information and power, which is important for battery-less sensors. Therefore, new SCMR systems that are optimally designed and miniaturized in size will significantly enhance various technologies in many applications.

The optimal and miniaturized SCMR systems are studied here. First, analytical models of the Conformal SCMR (CSCMR) system and thorough analysis and design

methodology have been presented. This analysis specifically leads to the identification of the optimal design parameters, and predicts the performance of the designed CSCMR system. Second, optimal multiband and broadband CSCMR systems are designed. Two-band, three-band, and four-band CSCMR systems are designed and validated using simulations and measurements. Novel broadband CSCMR systems are also analyzed, designed, simulated and measured. The proposed broadband CSCMR system achieved more than 7 times larger bandwidth compared to the traditional SCMR system at the same frequency. Miniaturization methods of SCMR systems are also explored. Specifically, methods that use printable CSCMR with large capacitors, novel topologies including meandered, SRRs, and spiral topologies or 3-D structures, lower the operating frequency of SCMR systems, thereby reducing their size. Finally, SCMR systems are discussed and designed for various applications, such as biomedical devices and simultaneous powering of multiple devices.

TABLE OF CONTENTS

TABLE OF TABLES

TABLE PAGE

TABLE OF FIGURES

FIGURE PAGE

CHAPTER 1

INTRODUCTION

1.1 Problem Statement

Wireless power transfer technologies for communication and recharging devices have recently attracted significant research attention. The increased interest stems from current society needs in various areas such as, transportation, civil engineering, sensors, biomedical systems, microelectronics, and wireless communications [1-7]. Wireless powering is useful in cases where instantaneous or continuous energy is needed and where wired connections are difficult, expensive, or impossible [1-3]. By using wireless powering, mobile phones, laptop computers, mp3 players, electric and hybrid vehicles, household robots, and other portable electronics are capable of charging themselves without ever being plugged in, eliminating powering wires or bulky batteries which are currently heavy and expensive to operate [4-5]. Also, wireless powering technologies are very important for embedded sensors, implantable medical devices, and operating machines. However, the majority of mature wireless technologies are not suitable for efficient energy transfer, since most of the energy is wasted into free space and their efficiency drops dramatically when the distance increases [5].

Recently, the Strongly Coupled Magnetic Resonance (SCMR) method was introduced, which is based on resonant inductive coupling operating principle, offering the possibility of transferring power with high efficiency in relative larger distance (mid-range) [3-7]. The crucial advantage of using the non-radiative field is that most of the power not picked up by the receiving coil remains bound to the vicinity of the sending

unit, instead of being radiated into the environment [4]. Another advantage of SCMR is that is safer for humans, because it relies on magnetic near-fields which interact very weakly with biological tissues [8].

In the last few decades, wireless sensors have been widely adopted in numerous applications [9-12]. However, wireless sensors are still mostly powered by batteries which impose strict limitations on the lifetime of sensors. WPT systems that can wirelessly charge or power sensors are very useful, especially for embedded sensors that cannot be easily accessed to replace their battery. Also, WPT systems that are multiband are of great interest as they can power multiple sensors for different applications. Furthermore, broadband WPT systems can support simultaneous powering and communication through the same wireless link thereby enabling autonomous (i.e., battery-less) sensors.

However, since the SCMR is a new method developed recently, there are limited studies on optimal designs of SCMR system. The study of multiband and broadband WPT systems has been very limited. In fact, it has been found that only [13-14] examined two-band and three-band SCMR WPT systems. However, no analytical models of such systems and no thorough analysis and design methodology for such systems have been presented. In addition, no broadband SCMR WPT systems have been developed and traditional SCMR systems exhibit narrowband efficiency thereby imposing strict limitations on simultaneous wireless transmission of information and power, which is important for battery-less sensors. Also, according to our knowledge no work has been done on the miniaturization of SCMR systems. In fact, only loops or coils have been utilized to design SCMR systems in previous work [3-8, 13-16]. Therefore, other SCMR

element shapes are needed in order to meet the requirements of various wireless powering applications. New SCMR topologies (e.g., planar) that are optimally designed and miniaturized in size will significantly enhance various technologies, such as, mobile phones, Integrated Circuit chips (ICs), sensors, microelectronics and biomedical implants [17-20].

1.2 Research Objectives and Contributions

Most portable electronic devices and sensors require batteries that need to be recharged often through wired connections. In order to eliminate wires and replaceable batteries, wireless powering technologies have been developed which can charge electronic devices and support continuous autonomous operation [1-5]. This research focuses on developing models and methodologies for designing optimal SCMR systems based on novel element geometries. Our analytical models will provide a straightforward way to design SCMR systems that are optimal (in terms of their efficiency) at the desired frequency of operation. Also, our research will develop miniaturized designs that are suitable for various applications, where maintaining a small size for a device is critical. Specifically, this research performs the following tasks:

(i) Develop optimal and cost effective SCMR systems for wireless power transmission in various applications. Optimal designs of SCMR systems need to satisfy size and power transfer requirements.

(ii) Derive analytical model for SCMR systems. The effects of dimension parameters on performance and frequency will be formulated. The efficiency of SCMR systems is calculated using the proposed analytical model as a function of

geometrical and material parameters. Therefore, this analysis leads to the identification of geometrical parameters of SCMR WPT systems that provide maximal efficiency and without severe frequency splitting.

(iii) Design multiband SCMR systems that use multiple pairs of different size loop resonators resonating at different frequencies thereby transferring power efficiently at multiple bands. WPT systems that can efficiently transmit power in different bands, may be used for applications where a single WPT transmitting system needs to power devices or sensors of different sizes at different distances. Also, multiband WPT systems can be used to provide compatibility with different WPT standards. Therefore, multiband WPT systems can be very useful for accommodating multiple standards as well as different receiver sizes and ranges.

(iv) Design broadband SCMR systems and develop design guidelines for optimal broadband CSCMR systems. This design can be particularly useful when power and data need to be wirelessly transferred through the same wireless link. Traditional SCMR systems exhibit narrowband efficiency thereby imposing strict limitations on simultaneous wireless transmission of information and power, which is important for battery-less sensors.

(v) Pursue miniaturization of SCMR systems. A comprehensive analysis of novel resonator geometries (such as, split-ring resonators [21] and spiral resonators) and substrate effect will be carried out in order to reduce the dimension of SCMR systems and maintain high power transfer efficiency. The miniaturization of SCMR systems will significantly enhance the field of biomedical implants by providing small, highly efficient wireless powering systems that can support safe

and wireless operation of bio-implants, thereby eliminating transcutaneous wires that can lead to discomfort and infection.

(vi) Develop SCMR systems in various applications. The performance of our SCMR designs will be examined under different environments. SCMR systems for biomedical devices are developed. The human safety standards and human tissue environment are taken into consideration. Misalignment effects in SCMR systems are also studied.

1.3 Methodology

This dissertation addresses the problem of optimized and miniaturized SCMR systems for various applications. This work demonstrates that rigorous analysis performed with our analytical model is critical for identifying the optimum conditions for wireless power transmission, such as, operation frequency, frequency splitting, geometrical and material parameters, etc. These conditions will contribute to the optimum design of wireless power transmission systems.

In order to make optimal designs and realize the miniaturization of SCMR systems, analytical as well as computational methods will be used in this research. Besides inductance and capacitance values, three types of loss mechanisms will also be analyzed to find the optimum frequency range: (a) the resistance loss, (b) the radiative loss [22], and (c) the propagation loss in substrate. The equivalent circuit of an SCMR is accurately described by a lumped RLC circuit. This circuit can be used for deriving analytical models that describe the SCMR systems' resonant frequency as well as the frequency where the Q-factor is maximum. Our research will develop such models based

on quasi-static formulations of the distributed inductance and capacitance of various SCMR elements, such as, loops and spirals [23-24]. Simulation software ANSYS HFSS will be used to validate our analytical models for the resistance and inductance. Finally, the efficiency and Q-factor will be calculated based on our analytical and simulation models.

In order to derive the relations that SCMR elements have to satisfy in order to achieve optimal efficiency calculus analysis will be performed with mathematical tools, such as, Mathematica. Then, the performance of entire SCMR systems will be simulated in electromagnetic software, such as, ANSYS HFSS and Designer, in order to validate our analytical formulations and verify that our designs achieve optimal efficiency. Their electrical behavior using S-parameters will be described. Miniaturized SCMR systems will also be designed by using novel element topologies and advanced materials. These systems will also be analyzed using EM simulation software. Finally, measurements using Vector Network Analyzer (VNA) will be conducted to verify our designs and theoretical models.

1.4 Dissertation Outline

The dissertation is organized as follows. Chapter 2 reviews the existing literature related to the issues involved in wireless power transmission and strongly coupled magnetic resonance technologies. In Chapter 3, accurate analytical models of SCMR WPT system with multiple resonators are developed in order to predict the performance of the WPT system. Using the theoretical analysis, novel multiband and broadband SCMR WPT systems are proposed in Chapter 4. Chapter 5 describes several

miniaturization methods for SCMR WPT systems. In Chapter 6, practical SCMR systems are discussed and developed for various applications, such as biomedical devices and simultaneous powering of multiple devices. Finally, Chapter 7 provides the conclusions of our research and identifies future research directions.

CHAPTER 2

BACKGROUND AND RELATED WORK

In this chapter, we review existing literature related to the issues involved in Wireless Power Transmission (WPT) and Strongly Coupled Magnetic Resonance (SCMR). Several WPT methods are presented and compared in Section 2.1. The recent methods that used SCMR technology are described in detail in Section 2.2.

2.1 Wireless Power Transmission (WPT) Techniques

WPT is the process in which electrical energy is transmitted from a power source to an electric load, without the use of artificial conductors. The advances of wireless power technology have been applied across a broad spectrum of applications nowadays [25-27]. The portable electronic devices (e.g., mobile phones, laptops), electric vehicles, embedded sensors and biomedical implant devices need instantaneous or continuous energy [28-29]. The traditional powering wires or bulky batteries are heavy and expensive to operate.

Wireless powering was first proposed by Nikola Tesla, whose goal was to distribute power wirelessly to the entire earth from his Wardenclyffe Tower [1-3] via the electric field in 1901. However, typical embodiments involved undesirably large electric fields which may cause permanent damage to electrical devices in the vicinity due to the enormous amount of voltage being transmitted [1]. Due to a lack of funds and techniques, his experiment was not finished. In 1964, William C. Brown proposed the first wireless power transfer scheme via microwave beams [25]. In 1970, Peter Glaser conceived that space solar energy could be converted into electrical energy, which would be transferred

via microwaves [30-31]. In the late 1970s, the WPT technique via radiative EM wave for long-distance attracted interest in industrial, telecommunication, and medical applications [32-34]. Later, in the early 21st century, non-radiative wireless power techniques via EM inductive coupling were developed greatly [35-39]. In 2007, the Strongly Coupled Magnetic Resonance (SCMR) method was discovered by a team of MIT scientists [3] who in their original experiment transferred 60 watts of power at a distance of 200 cm to illuminate a light bulb [4]. Later, this technique was extended to power multiple devices simultaneously in air, and 60% efficiency was reported for a distance of 200 cm [35]. Based on different working ranges, wireless powering technologies can be categorized into two types: far-field and near-field techniques [9].

2.1.1 Far-field Technique

The WPT technologies based on EM radiation used radiative energy or field for transmission. At high frequencies of the spectrum, optical techniques are used to send power via collimated beams of light to remote detectors. The received photons are finally converted to electrical energy. At microwave frequencies, there are two types of far-field approaches based on different propagation directions: Omni-directional and Uni-directional methods [40].

The Omni-directional method works as the broadcast way, transmitting power in a omni-direction pattern However, its omni-directional properties, allowing for power transfer anywhere in the coverage area, make such radiation excellent for wireless communication but hardly able to achieve high efficiencies for wireless powering. The power density will decrease with a $1/r^2$ dependence. The received power levels will be

many orders of magnitude less than what is transmitted [15]. Therefore, the efficiency will dramatically fall over distance. The omni-directional method can only be used for charging some ultra-low power sensors for environmental monitoring.

The Uni-directional method transfers the power from an antenna like radios. This method has been widely used in some RFID techniques. Using high gain antennas, some RF and microwave systems can transfer power over kilometers with up to 90% efficiency [15]. However, these systems need sophisticated tracking and alignment mechanism. Therefore, these devices usually occupy large space and are not convenient to use in some daily applications.

2.1.2 Near-field Technique

Near-field techniques use the principle of magnetic induction to wirelessly transfer power from one device to other devices on near field, where the generated electromagnetic field dominates the region close to the transmitter or scattering object [41]. The distance is generally within 20 cm and the operating frequency is typically in kHz [42-43]. This technology is used in some electric toothbrushes or mobile phones. Near-field techniques achieve higher efficiencies but only for short transmission distances (e.g., 1 cm) because their efficiency of these inductive links drops rapidly with distance (decays as $1/ r^3$) [22],[44]. Also, the magnetic coupling has less freedom in positioning the transmitting device and receiving device. They need to be positioned carefully in order to achieve high transfer efficiency.

2.2 Strongly Coupled Magnetic Resonance (SCMR)

Recently, the Strongly Coupled Magnetic Resonance (SCMR) method was introduced, which is based on resonant inductive coupling. SCMR can achieve highly efficient wireless power transfer to larger distances [2-7]. The SCMR method works in mid-range, i.e., 10-300 cm. Compared to traditional WPT methods based on inductive coupling, the SCMR method is based on high resonant coupling, which is more efficient and reliable over distance, flexible in orientations and easy to simultaneously power multiple devices [6],[45].

2.2.1 Basic Principle of SCMR System

The SCMR method is based on the resonant coupling between two high Quality-factor (*Q*-factor) resonators. In fact, resonance phenomena occur in various forms in nature, such as mechanical resonance, acoustic resonance, electromagnetic resonance, etc. The resonance occurs when a system is able to store and easily transfer energy between two or more different storage modes. The *Q*-factor is a measure of how well the resonator can store energy. It defined as the ratio of the energy stored in the oscillating resonator to the energy dissipated per cycle by the damping processes. Higher *Q* indicates a lower rate of energy loss relative to the stored energy of the oscillator. Figure 2.1 shows an example of an electromagnetic resonator, which consists of a resistor, an inductor and a capacitor.

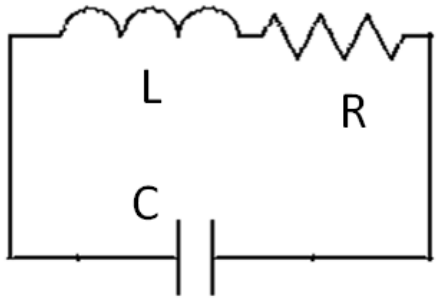

Figure 2.1. A typical equivalent circuit of a LC resonator.

Energy oscillates between the inductor (in form of magnetic field) and the capacitor (in form of electric field) at the resonant frequency. Since the magnitudes of inductive reactance and the capacitive reactance are equal, $wL=1/wC$, the resonant frequency can be described as:

$$\omega_0 = \frac{1}{\sqrt{LC}} \ . \tag{2.1}$$

In this LC circuit, the stored energy is the sum of energies stored in lossless inductors and capacitors. The lost energy is the sum of the energies dissipated in resistors per cycle. Therefore, the *Q*-factor can be written as [46]:

$$Q = \omega_0 \frac{W_m + W_e}{P_{loss}} = \omega_0 \frac{2W_m}{P_{loss}} = \frac{\omega_0 L}{R} = \frac{1}{\omega_0 RC} \ . \tag{2.2}$$

In a typical SCMR system, resonators must be high *Q*-factor in order to efficiently transfer energy at greater distances or with more positional freedom. Therefore, the design of high *Q*-factor resonator is the critical part for the design of the SCMR WPT system. From formula (2.2), it shows that reducing the loss in the circuit, such as the resistance of the resonator, will increase the Q-factor of the system.

A typical SCMR WPT system is described in Figure 2.2. The whole system is formed by four elements: a source loop, a load loop, a transmitting (TX) resonator and a receiving (RX) resonator. In Kurs' experiment, see Figure 2.2 (a), the TX and RX resonators are realized by coils, which have self-capacitance and inductance. TX and RX resonators are also formed by single loops connected to lumped capacitors, see Figure 2.2 (b). The TX and RX resonators operate at the same frequency, where their Q-factor is maximum. The power is initially applied to the source loop, which is inductively coupled to the TX element. Then the power is transferred between the TX loop and RX loop with high resonance over the distance, l_2. Other surrounded devices that do not resonant at the same frequency will not capture any energy from this SCMR system. Finally, the power is inductively coupled to the load loop. Therefore, energy can be transferred efficiently between the source and load.

(a)

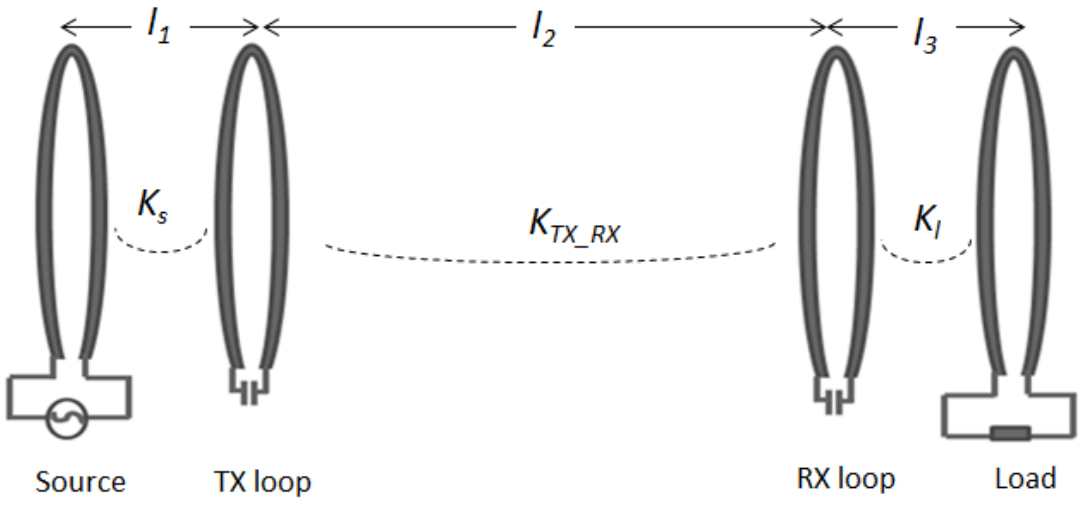

(b)

Figure 2.2. Two typical SCMR WPT systems. (a) TX and RX resonators are coil. (b) TX and RX loops with lumped capacitors.

In order to achieve high efficiency for the whole system operation, impedance matching designs between the generator and the TX resonator, as well as the load and the RX resonator, are often needed. The traditional method is directly connecting the generator and load to the respective resonators with a variety of impedance matching networks. This method usually includes a complicated circuit, which occupies more space. Another method is realized by inductively coupling between the source loop and TX resonator, as well as between the RX resonator and the load loop. The impedance matching is accomplished by tuning the input (K_s) and output coupling (K_l). Therefore, the coupling can be changed by adjusting the distances (l_1, l_3) or the alignment between source loop and TX resonator, as well as between the RX resonator and load loop.

2.2.2 Efficiency and Range

Efficiency and range are two important issues for WPT systems. The efficiency is defined as the ratio of the power delivered to the load over the power sent by the source. The system between the source and load can be modelled as a two-port network, as shown in Figure 2.3.

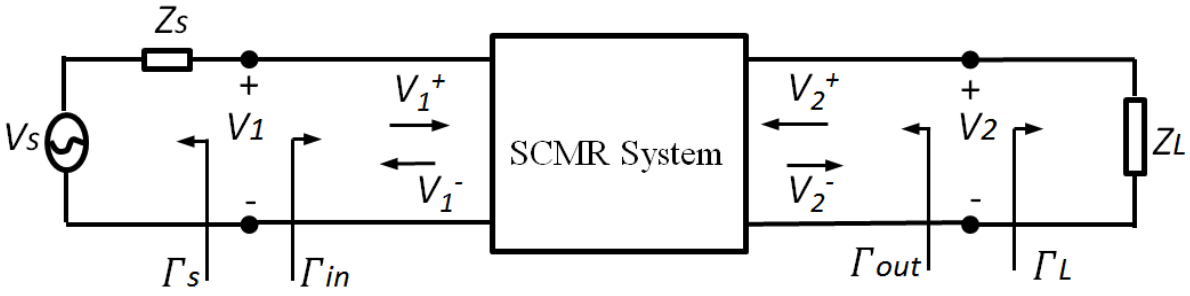

Figure 2.3. A two-port network model of a tested SCMR system.

Such networks can be characterized by various equivalent circuit parameters, such as impedance matrix, transfer matrix, and scattering matrix.

$$\begin{bmatrix} V_1^- \\ V_2^- \end{bmatrix} = \begin{bmatrix} S_{11} & S_{12} \\ S_{21} & S_{22} \end{bmatrix} \begin{bmatrix} V_1^+ \\ V_2^+ \end{bmatrix}. \tag{2.3}$$

Therefore the voltage can be presented as

$$V_1^- = S_{11}V_1^+ + S_{12}V_2^+ \tag{2.4}$$

$$V_2^- = S_{21}V_1^+ + S_{22}V_2^+ \tag{2.5}$$

The reflection coefficient seen looking toward the load and the source are

$$\Gamma_L = \frac{Z_L - Z_0}{Z_L + Z_0} \tag{2.6}$$

$$\Gamma_S = \frac{Z_S - Z_0}{Z_S + Z_0} \tag{2.7}$$

The reflection coefficient looking into port 1 and 2 of the terminated network are described as

$$\Gamma_{in} = \frac{V_1^-}{V_1^+} = S_{11} + \frac{S_{12}S_{21}\Gamma_L}{1 - S_{22}\Gamma_L} \tag{2.8}$$

$$\Gamma_{out} = \frac{V_2^-}{V_2^+} = S_{22} + \frac{S_{12}S_{21}\Gamma_S}{1 - S_{11}\Gamma_S} \tag{2.9}$$

The power transfer efficiency of the SCMR WPT system is defined as the power received by the load over the maximum available power from the generator. The powers can be expressed in terms of the S-parameters as follows [46-47]:

$$P_{avs} = \frac{|V_S|^2}{8Z_0}\frac{|1-\Gamma_S|^2}{1-|\Gamma_S|^2} \tag{2.10}$$

$$P_L = \frac{|V_S|^2}{8Z_0}\frac{\left(1-|\Gamma_L|^2\right)|1-\Gamma_S|^2|S_{21}|^2}{\left|(1-S_{11}\Gamma_S)(1-S_{22}\Gamma_L)-S_{12}S_{21}\Gamma_S\Gamma_L\right|^2}. \tag{2.11}$$

Therefore, the efficiency of the SCMR WPT system can be expressed in terms of the two-port S-parameters as follows:

$$\eta = \frac{P_L}{P_{avs}} = \frac{\left(1-|\Gamma_S|^2\right)|S_{21}|^2(1-|\Gamma_L|^2)}{\left|(1-S_{11}\Gamma_S)(1-S_{22}\Gamma_L)-S_{12}S_{21}\Gamma_S\Gamma_L\right|^2} \tag{2.12}$$

When the source and load impedances are matched to the reference impedance Z_0, so that $Z_S = Z_L = Z_0$ and $\Gamma_S = \Gamma_L = 0$, then the power transfer efficiency is equal to the squared magnitude of S_{12}. In this dissertation, it is assumed that the internal resistance of the source and the resistance of the load are equal to 50 Ohm. Therefore, SCMR's efficiency can be simplified as follows [15]:

$$\eta = |S_{21}|^2 . \tag{2.13}$$

In the following discussion, we use formula (2.13) to evaluate the efficiency performance of the SCMR WPT system.

The operating range of the SCMR WPT system is the distance between the SCMR's Transmitter and Receiver. Compared to the inductive coupling method, the SCMR WPT system has longer range, which is often several times of the size of the resonators.

2.2.3 Human Safety Consideration

Recently, WPT technologies are widely used in implantable biomedical devices and other aspects in daily life. Human safety is therefore taken into consideration. From the recent literature review, there is no evidence that shows the electromagnetic (EM) fields will cause cancer. SCMR is safer for humans, because it relies on magnetic near-fields which interact very weakly with biological tissues. However, long time exposure to the EM field will cause heat and increase temperature for body tissues. Therefore, there is some recommendation of safety levels defined by the Institute of Electrical and Electronic Engineers (IEEE), International Commission on Non-Ionizing Radiation Protection (ICNIRP), and the Federal Communications Commission (FCC) in order to avoid overheating of living tissue. The IEEE and ICNIRP determine a general public Specific Absorption Rate (SAR) limit of 4 W/kg for limbs and 2 W/kg for the head and trunk in 10 g of tissue. The FCC claims the exposure to radio frequency (RF) energy should be limited to a maximum SAR value of 1.6W/kg for 1g of tissue [48-52].

When developing a SCMR WPT system for biomedical implants, the human body model is used in ANSYS HFSS, and SAR distributions are discussed to assess whether compliance with the IEEE or FCC restrictions.

2.2.4 Applications

Wireless power transfer systems based on the SCMR are being developed for numerous applications based on their advantages, such as efficient, flexible, safe, and over long distances. Application areas including mobile devices, household appliances, medical applications, and electrical vehicles are discussed in the following parts.

The SCMR method can be firstly applied to charge mobile devices or household appliances, such as mobile phone, laptop, and vacuum cleaner. This makes devices more convenient and reliable to use because of getting rid of the power cord or battery replacement. In [15], authors successfully wirelessly powered a laptop computer without a battery. A peak power consumption of 12 W was delivered over a 70 cm distance. Also, the benefits of charging over distance and with spatial freedom will promote the adoption of SCMR technologies in mobile devices.

In medical applications, wireless charging technologies are greatly needed for portable or implantable medical devices, such as pacemakers, Left Ventricular Assist Device (LVAD) heart pumps, infusion pumps, surgical power tools, and handheld diagnostic instruments [52-53]. Traditional LVADs are powered by a set of external batteries that connected by a drive line routed into the body through the skin percutaneously [53]. The tissue where the drive line enters is easy to infection and replacement of batteries requires a surgical operation that imposes risks to patients' health.

In 2011, Thoratec and Witricity developed a fully implantable LVAD that would move the battery inside the body to be recharged wirelessly using SCMR method [53]. This development enables the charging process over 10 in with the flexibility in alignment and orientation. Other medical implantable devices, such as neurostimulators, pacemakers, implantable drug-delivery pumps, electronic ophthalmic and cochlear implants can also be benefited by the SCMR technologies. Also, by eliminating the charging cords and batteries, the surgical power tools and handheld diagnostic instruments can be hermetically sealed, easier to sterilize and less prone to failures associated with repeated connector insertion and battery replacement.

Another useful application for SCMR technology is the charging electric vehicles. Due to the higher wattage necessary, wireless charging of cars is more difficult than mobile phone. A connection between a transmitting pad on the ground (such as in a garage) and a receiving pad integrated on the bottom of the vehicle is created for wireless charging. Researchers and engineers from companies such as, Hyundai, Audi, and Qualcomm have made a lot of progress in this area. Oak Ridge National Laboratory and Hyundai America Technical Center Inc. have been working since 2012 to demonstrate wireless charging on a variety of vehicles [54]. In 2013 Utah State's Energy Dynamics Laboratory demonstrated a 20-passenger bus powered with a 20-25 kW stationary wireless charger, with efficiency greater than 90% [55]. Right now, engineers are developing systems that take about 4 to 6 hours to charge most all-electric vehicles with a transfer of more than 6.6 kilowatts (kW). In the future, the engineers hope to reach 10 kW and eventually 19 kW to facilitate faster charging [54].

2.3 Recent Progress

Since SCMR method was proposed by MIT scientist in 2007, related studies have been done on various applications. In fact, only loop or coil SCMR elements have been used in previous designs and other types of SCMR elements, such as, planar, are needed in order to satisfy the requirements of different applications. Since SCMR is a new method, there are limited studies on optimal configurations of SCMR systems and according to our knowledge no miniaturization of SCMR systems has been achieved.

Previous SCMR research has focused on how to improve its efficiency and range through different methods [56-65]. For example, adaptive frequency tuning methods and automated impedance matching systems have been developed to achieve maximum efficiency [15], [58]. Optimized compensate capacitors with a switching controller or transmitters and receivers with two resonators have also been utilized to increase SCMR's efficiency [59-61]. The relationship between the maximum efficiency and range was examined in [62]. Furthermore, a WPT system with frequency-insensitive antiparallel resonant loops was proposed in order to address the variation of SCMR's efficiency with distance [63]. Also, repeaters between SCMR's transmitter and receiver have been used to increase SCMR's range [64-65].

Recently, optimal WPT systems with multiple transmitters or multiple receivers have been developed [16],[45],[66-67]. Equivalent circuit models of WPT systems with multiple transmitters or multiple receivers have been also studied [16],[45],[66]. In addition, optimal adjustment of coupling between transmitters or between receivers has been applied in order to increase the efficiency of WPT systems [67]. However, the study of multiband and broadband WPT systems has been very limited. In fact, it has been

found that only [13-14] examined two-band and three-band SCMR WPT systems. However, no analytical models of such systems and no thorough analysis and design methodology for such systems have been presented. In addition, no broadband SCMR WPT systems have been developed and traditional SCMR systems exhibit narrowband efficiency thereby imposing strict limitations on simultaneous wireless transmission of information and power, which is important for battery-less sensors.

CHAPTER 3

OPTIMAL DESIGN OF CSCMR SYSTEMS

In this chapter, optimal design of Conformal SCMR (CSCMR) WPT system is investigated. Our analysis relies on equivalent circuit models. SCMR WPT systems can be described as equivalent RLC circuits. The circuit theory based on mutual inductance model was used for analyzing SCMR systems. Section 3.1 describes the analytical models for SCMR systems with one and multiple pairs of resonators, which can be used to study and predict the performance of such systems. Optimal designs for choosing parameters of the SCMR system with one or multiple pairs of resonators are discussed in Section 3.2 and Section 3.3, respectively.

3.1 Theoretical Model of CSCMR WPT Systems

A conventional Strongly Coupled Magnetic Resonance (SCMR) system consists of four elements: source loop, transmitting (TX) resonator, receiving (RX) resonator and load loop, as shown in Figure 3.1. Based on the theory of SCMR, the TX and RX resonators are designed to operate at the same frequency where their *Q*-factor of the loop is maximum. Energy is strongly coupled between the TX and RX at the resonant frequency. Therefore, energy is transmitted efficiently between the source loop and load loop. However, conventional SCMR systems require certain distance, *t*, between the source and the TX resonator as well as between the load and the RX resonator (see Figure 3.1). Depending on the dimension of each element, this distance, *t*, can be relatively large. Therefore, traditional SCMR systems occupy significant volume and they cannot be easily incorporated in modern communication systems.

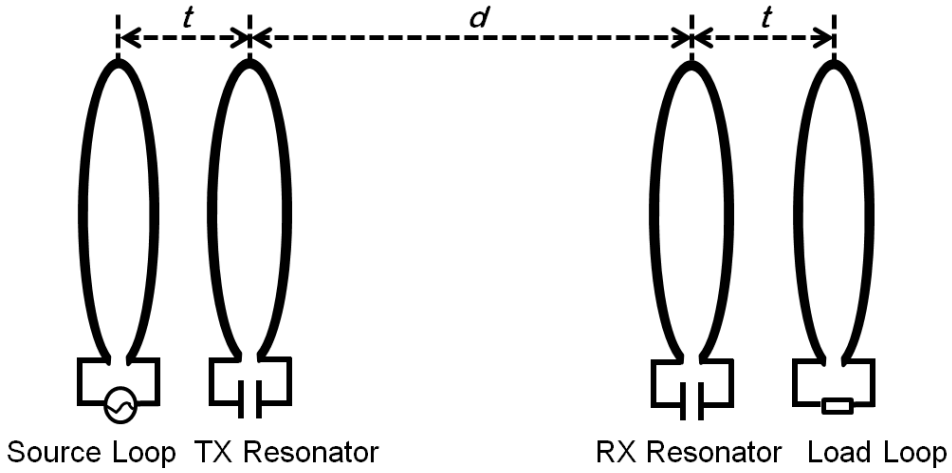

Figure 3.1. Schematic of a traditional SCMR system.

In order to develop planar WPT systems, the source loop and load loop were embedded into the TX and RX resonators, respectively. The concept of Conformal SCMR (CSCMR) system was introduced here. Figure 3.2 illustrates a typical CSCMR system with one pair of resonators. The CSCMR method has been previously proposed and developed in [68-69].

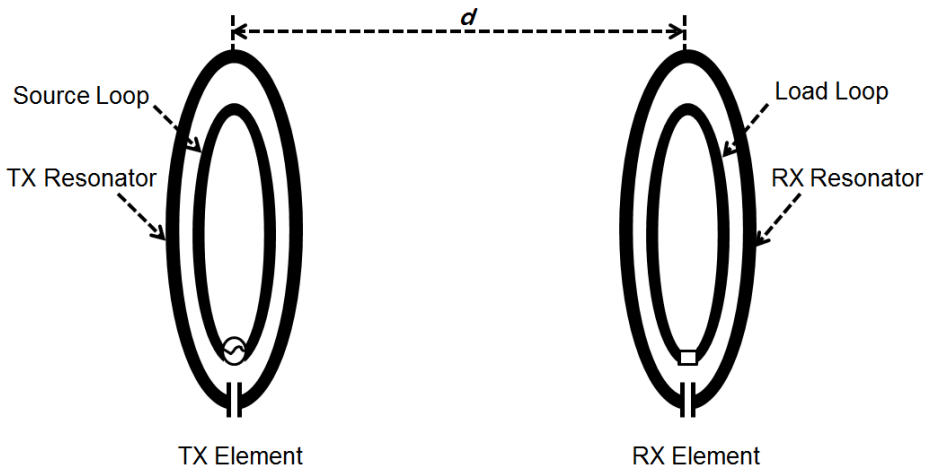

Figure 3.2. Schematic of a CSCMR system.

3.1.1 SCMR Model with One Pair of Resonators

An equivalent circuit model with one pair of resonators, one source loop and one load loop is developed, as shown in Figure 3.3. This equivalent circuit can represent either the SCMR model of Figure 3.1 or the CSCMR model of Figure 3.2.

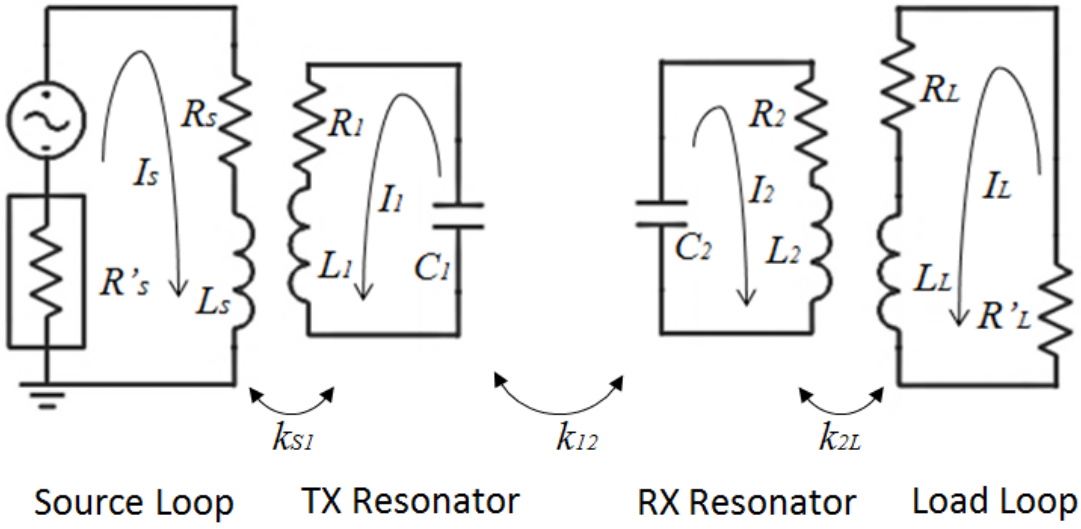

Figure 3.3. Equivalent circuit diagram of a CSCMR WPT system with one pair of resonators, one source loop and one load loop.

R_S' and R_L' are the internal resistance of the source and the resistance of the load, respectively (here, they are both assumed to be 50 Ohm); The total resistance of the TX resonator, the RX resonator, source loop and load loop are represented as R_1, R_2, R_s and R_L respectively (the total resistance includes the radiation resistance, R_{rad}, and loss resistance, R_{ohm}); The equivalent inductance of each loop is L_i. The formulas of these parameters are as follows [70-71]:

$$R_i = R_{iohm} + R_{irad} \tag{3.1}$$

$$R_{iohm} = \frac{r_i}{r_{ci}} \sqrt{\mu_0 \rho \pi f_{i\max}} \tag{3.2}$$

$$R_{irad} = 320\pi^6 \left(\frac{f_{i\max} r_i}{c} \right)^4 \tag{3.3}$$

$$L_i = \mu_0 r_i \left[\ln\left(\frac{8r_i}{r_{ci}} \right) - 2 \right] \tag{3.4}$$

where μ_0 is the permeability of free space and ρ is the material resistivity; r_i and r_{ci} are the radius and cross-sectional radius of the loop. Also, based on the theory of traditional SCMR, the resonators need to be designed so that they resonate at the frequency where the *Q*-factor of the resonating loop is maximum. The frequency, f_{imax}, where this maximum occurs, can be written as [70]:

$$f_{i\max} = \frac{c^{8/7} \mu_0^{1/7} \rho^{1/7}}{4 \cdot 15^{2/7} \pi^{11/7} r_{ci}^{2/7} r_i^{6/7}} . \tag{3.5}$$

The required capacitance to resonate a loop is calculated by

$$C_i = \frac{1}{4\pi^2 f_{\max}^2 L_i} . \tag{3.6}$$

Based on Kirchhoff's Voltage Law (KVL), in a closed loop, the algebraic sum of the products of the mutual- and self-impedances with their corresponding currents is equal to the total *electromotive force* available in that loop. Therefore, the equivalent circuits of all the loops (source, resonator 1, resonator 2, and load) can be described by the formulas below [16]:

$$
\begin{aligned}
V_s &= \left(R_s^{'} + R_s + j\omega L_s\right) I_s + j\omega M_{s,1} I_1 + j\omega M_{s,2} I_2 + j\omega M_{S,L} I_L \\
0 &= j\omega M_{1,s} I_S + \left(R_1 + j\omega L_1 - j\frac{1}{\omega C_1}\right) I_1 + j\omega M_{1,2} I_2 + j\omega M_{1,L} I_L \\
0 &= j\omega M_{2,s} I_S + j\omega M_{2,1} I_1 + \left(R_2 + j\omega L_2 - j\frac{1}{\omega C_2}\right) I_2 + j\omega M_{2,L} I_L \\
0 &= j\omega M_{L,S} I_S + j\omega M_{L,1} I_1 + j\omega M_{L,2} I_2 + \left(R_L^{'} + R_L + j\omega L_L\right) I_L
\end{aligned}
\tag{3.7}
$$

The equivalent circuit (3.7) can be written in matrix form as follows:

$$
\begin{bmatrix} V_S \\ 0 \\ 0 \\ 0 \end{bmatrix} = \begin{bmatrix} Z_S & j\omega M_{S1} & j\omega M_{S2} & j\omega M_{SL} \\ j\omega M_{1S} & Z_1 & j\omega M_{12} & j\omega M_{1L} \\ j\omega M_{2S} & j\omega M_{21} & Z_2 & j\omega M_{2L} \\ j\omega M_{LS} & j\omega M_{L1} & j\omega M_{L2} & Z_L \end{bmatrix} . \begin{bmatrix} I_S \\ I_1 \\ I_2 \\ I_L \end{bmatrix} \tag{3.8}
$$

where:

$$Z_S = R_S + R_S^{'} + j\omega L_S \tag{3.9}$$

$$Z_L = R_L + R_L^{'} + j\omega L_L \tag{3.10}$$

$$Z_1 = R_1 + j\omega L_1 - j\frac{1}{\omega C_1} \tag{3.11}$$

$$Z_2 = R_2 + j\omega L_2 - j\frac{1}{\omega C_2} \tag{3.12}$$

In order to have maximum coupling, all loops are assumed to be parallel and are placed along the z-axis at a distance, *d*, from each other, as shown in Figure 3.4. The magnetic field flux density, B_i, at a distance of *d*, from the primary loop (r_i) along the *Z*-axis is expressed based on the Biot–Savart law as follows [22]:

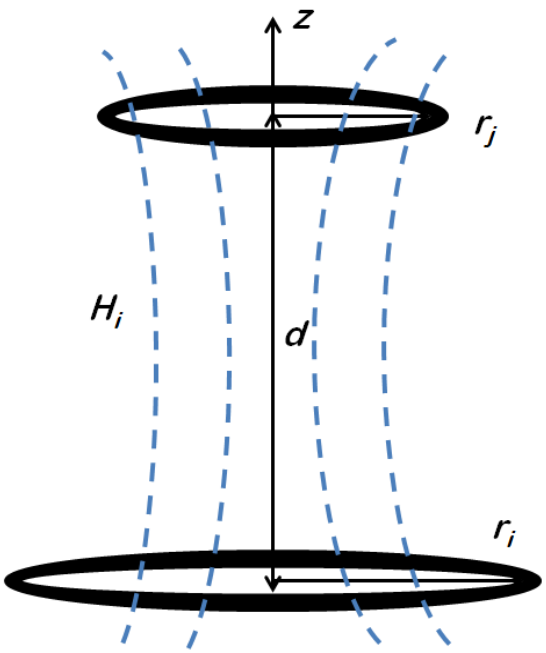

Figure 3.4. Two coaxial loops are placed along the z-axis at a distance, *d*, from each other.

$$B_i = \mu_0 H_i = \frac{\mu_0 I_i r_i^2}{2\left(r_i^2 + d^2\right)^{3/2}}. \tag{3.13}$$

When a secondary loop (r_j) is located near the primary loop, the mutual inductance between the two loops is derived as [19-22],[71-72]

$$M_{j,i} = \frac{\psi_{j,i}}{I_i} = \frac{B_i A_j}{I_i} = \frac{\mu_0 \pi r_i^2 r_j^2}{2\sqrt{\left(r_i^2 + d^2\right)^3}} \tag{3.14}$$

where A_j is the area enclosed by the j^{th} loop. When the two loops are placed concentrically on the same plane, the distance, *d*, decreases to zero. In this case, the mutual inductance should be calculated using the larger loop as the exciting loop [73]. Therefore, the mutual inductance between two coplanar loops can be written as

$$\begin{cases} M_{j,i} = \dfrac{\mu_0 \pi r_j^2}{2r_i}, \left(r_i > r_j, d = 0\right) \\ M_{j,i} = M_{i,j} = \dfrac{\mu_0 \pi r_i^2}{2r_j}, \left(r_i < r_j, d = 0\right) \end{cases}. \tag{3.15}$$

The solution of the circuit, which is shown in Figure 3.3, can be derived from (3.8) as

$$[I] = [Z]^{-1}[V]. \tag{3.16}$$

The voltage across the load can be written as

$$V_L = -I_L R_L^{'}. \tag{3.17}$$

Also, the WPT efficiency is defined as the ratio of the power delivered to the load over the power sent by the source. The system between the source and load can be modeled as a two-port network and the power transfer efficiency can be expressed in terms of the two-port S-parameters as follows, [46-47]:

$$\eta = \frac{\left(1-\left|\Gamma_S\right|^2\right)\left|S_{21}\right|^2 \left(1-\left|\Gamma_L\right|^2\right)}{\left|\left(1-S_{11}\Gamma_S\right)\left(1-S_{22}\Gamma_L\right)-S_{12}S_{21}\Gamma_S\Gamma_L\right|^2} \tag{3.18}$$

When the source and load impedances are matched to the reference impedance Z_0, so that $Z_S = Z_L = Z_0$ and $\Gamma_S = \Gamma_L = 0$, then the power transfer efficiency is equal to the squared magnitude of S_{12}. Here, it is assumed that the internal resistance of the source and the resistance of the load are equal to 50 Ohm. Therefore, SCMR's efficiency can be written as follows [15]:

$$\eta = \left|S_{21}\right|^2 = \left|2\frac{V_L}{V_S}\left(\frac{R_S^{'}}{R_L^{'}}\right)^{1/2}\right|^2 = \left|4\frac{I_L^2 R_L^{'} R_S^{'}}{V_S^2}\right|. \tag{3.19}$$

By solving the matrix of equivalent circuit (3.8), the current in the load loop can be derived as

$$I_L = \frac{-(j\omega M_{LS}A + j\omega M_{L2}B + j\omega M_{L3}C)}{D}$$

$$\begin{cases} A = ei - fh \\ B = (fg - di) \\ C = (dh - eg) \\ D = aA + bB + cC \end{cases}, \quad \begin{cases} a = Z_S Z_L + \omega^2 M_{SL} M_{LS} \\ b = j\omega M_{S1} Z_L + \omega^2 M_{SL} M_{L1} \\ c = j\omega M_{S2} Z_L + \omega^2 M_{SL} M_{L2} \\ d = j\omega M_{1S} Z_L + \omega^2 M_{1L} M_{LS} \\ e = Z_1 Z_L + \omega^2 M_{1L} M_{L1} \\ f = j\omega M_{12} Z_L + \omega^2 M_{1L} M_{L2} \\ g = j\omega M_{2S} Z_L + \omega^2 M_{2L} M_{LS} \\ h = j\omega M_{21} Z_L + \omega^2 M_{2L} M_{L1} \\ i = Z_2 Z_L + \omega^2 M_{2L} M_{L2} \end{cases} \tag{3.20}$$

If we ignore the smaller part, $M_{S2}=M_{2S}=M_{SL}=M_{LS}=M_{1L}=M_{L1}=0$, the I_L can be simplified as:

$$I_L = \frac{-jM_{1S}M_{21}M_{L2}V_S\omega^3}{Z_S Z_1 Z_2 Z_L + M_{S1}M_{1S}Z_2 Z_L w^2 + M_{12}M_{21}Z_S Z_L w^2 + M_{2L}M_{L2}Z_S Z_1 w^2 + M_{S1}M_{1S}M_{2L}M_{L2}w^4} \tag{3.21}$$

Based on the formulas (3.16), (3.19), the efficiency can be derived as:

$$\eta = \frac{4w^6 M_{1S}^2 M_{21}^2 M_{L2}^2 R_S^{'} R_L^{'}}{\left(Z_S Z_1 Z_2 Z_L + M_{S1}M_{1S}Z_2 Z_L w^2 + M_{12}M_{21}Z_S Z_L w^2 + M_{2L}M_{L2}Z_S Z_1 w^2 + M_{S1}M_{1S}M_{2L}M_{L2}w^4\right)^2} \tag{3.22}$$

When the resonance takes place, the impedance of each loop is presented as following:

$$Z_S = R_S + R_S^{'} \approx R_S^{'} \tag{3.23}$$

$$Z_1 = R_1 \tag{3.24}$$

$$Z_2 = R_2 \tag{3.25}$$

$$Z_L = R_L + R_L^{'} \approx R_L^{'} \tag{3.26}$$

Based on formulas of:

$$M_{i,j} = k_{i,j}\sqrt{L_i L_j} \tag{3.27}$$

$$Q_i = \frac{w_i L_i}{R_i} \Leftrightarrow w_i L_i = Q_i R_i \tag{3.28}$$

The equation of efficiency also can be derived by substituting the term for series *Q*-factor and coupling coefficient:

$$\eta = \frac{4k_{1S}^2 k_{21}^2 k_{L2}^2 Q_1^2 Q_2^2 Q_S Q_L}{\left(1 + k_{S1}k_{1S}Q_S Q_1 + k_{12}k_{21}Q_1 Q_2 + k_{2L}k_{L2}Q_2 Q_L + k_{S1}k_{1S}k_{2L}k_{L2}Q_S Q_1 Q_2 Q_L\right)^2} \tag{3.29}$$

Therefore, through our analytical model, we can derive the relationship between system efficiency and coupling coefficients, circuit impedance or *Q*-factor. This clearly illustrates that the system efficiency can be written as a function of self and mutual impedances or as a function of the coupling coefficients and *Q*-factors.

In what follows, optimal designs are developed using a theoretical analysis based on the proposed equivalent circuit models of CSCMR systems. The efficiency of CSCMR WPT systems is calculated using the proposed analytical model as a function of geometrical and material parameters. Therefore, this analysis leads to the identification of geometrical parameters of CSCMR WPT systems that provide maximal efficiency and without severe frequency splitting.

3.1.2 SCMR Model with Multiple Pairs of Resonators

When a SCMR system included multiple pairs of resonators, the mutual couplings between each two resonators are more complicated. An equivalent circuit model with *n*

pairs of resonators, one source loop and one load loop is developed, as shown in Figure 3.5. In this system, the mutual coupling between all the different loops is included.

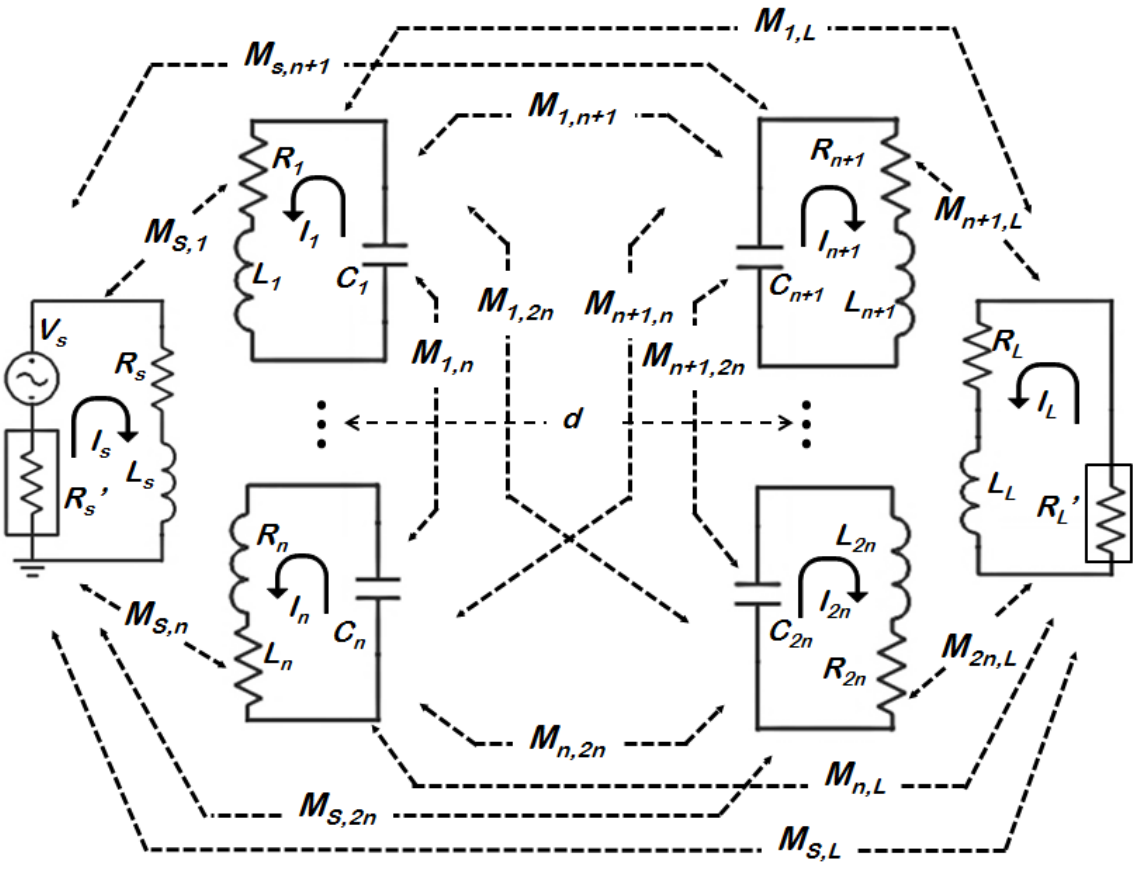

Figure 3.5. Equivalent circuit diagram of a CSCMR WPT system with *n* pairs of resonators, one source loop and one load loop.

Based on Kirchhoff's Voltage Law (KVL), in a closed loop, the algebraic sum of the products of the mutual- and self-impedances with their corresponding currents is equal to the total *electromotive force* available in that loop. Therefore, the equivalent circuits of all the loops (source, resonator 1, resonator 2, …, load) can be described by the formulas below [16]:

$$
\begin{aligned}
V_s &= \left(R_s^{'} + R_s + j\omega L_s\right) I_s + j\omega M_{s,1} I_1 + \cdots + j\omega M_{S,L} I_L \\
0 &= j\omega M_{1,s} I_S + \left(R_1 + j\omega L_1 - j\frac{1}{\omega C_1} \right) I_1 + \cdots + j\omega M_{1,L} I_L \\
&\vdots \qquad \vdots \qquad\qquad \vdots \qquad\qquad\qquad \vdots \\
0 &= j\omega M_{L,S} I_S + j\omega M_{L,1} I_1 + \cdots + \left(R_L^{'} + R_L + j\omega L_L\right) I_L
\end{aligned}
\tag{3.30}
$$

Equation (3.30) can be written in matrix form as follows:

$$
\begin{bmatrix} V_S \\ 0 \\ \vdots \\ 0 \\ \vdots \\ 0 \\ 0 \end{bmatrix} =
\begin{bmatrix}
Z_S & j\omega M_{S,1} & \cdots & j\omega M_{S,i} & \cdots & j\omega M_{S,2n} & j\omega M_{S,L} \\
j\omega M_{1,S} & Z_1 & \cdots & j\omega M_{1,i} & \cdots & j\omega M_{1,2n} & j\omega M_{1,L} \\
\vdots & \vdots & \ddots & \vdots & \ddots & \vdots & \vdots \\
j\omega M_{i,S} & j\omega M_{i,1} & \cdots & Z_i & \cdots & j\omega M_{i,2n} & j\omega M_{i,L} \\
\vdots & \vdots & \ddots & \vdots & \cdots & \vdots & \vdots \\
j\omega M_{2n,S} & j\omega M_{2n,1} & \cdots & j\omega M_{2n,i} & \cdots & Z_{2n} & j\omega M_{2n,L} \\
j\omega M_{L,S} & j\omega M_{L,1} & \cdots & j\omega M_{L,i} & \cdots & j\omega M_{L,2n} & Z_L
\end{bmatrix}
\begin{bmatrix} I_S \\ I_1 \\ \vdots \\ I_i \\ \vdots \\ I_{2n} \\ I_L \end{bmatrix}
\tag{3.31}
$$

where V_S, I_S, and Z_S, are the input voltage, current and impedance of the source loop, respectively; I_L and Z_L are the input current and impedance of the load loop, respectively; I_i and Z_i represent the input current and impedance of the i^{th} resonator ($1 \leq i \leq 2n$), respectively; $M_{S,i}$ represents the mutual inductance between the source loop and the i^{th} resonator, $M_{L,i}$ represents the mutual inductance between the load loop and the i^{th} resonator, and $M_{i,j}$ represents the mutual inductance between the i^{th} and j^{th} resonators ($1 \leq j \leq 2n$, $i \neq j$). Also, Z_S, Z_L and Z_i can be written as follows:

$$
Z_S = R_S + R_S^{'} + j\omega L_S \tag{3.32}
$$

$$
Z_L = R_L + R_L^{'} + j\omega L_L \tag{3.33}
$$

$$
Z_i = R_i + j\omega L_i - j\frac{1}{\omega C_i} \tag{3.33}
$$

All the calculations of loop resistance (R_i), loop impedance (Z_i), equivalent inductance (L_i), lumped capacitance (C_i), the mutual inductance between the two loops ($M_{i,j}$) can be found in formulas (3.1)-(3.4), (3.6), (3.14) and (3.15).

Using similar procedure of the SCMR system with one pair of resonator, the efficiency of the SCMR system with multiple pairs of resonators can also be expressed by solving formula (3.31) and using the formula (3.19). Since the calculation is very complex, MATLAB program is used to solve the equations and deduced the efficiency of the SCMR system.

3.2 Optimal Design of SCMR WPT Systems with One Pair of Resonators

For each SCMR WPT system, the self-inductance of each loop resonator is solely determined by its geometric parameters. Therefore, each loop can resonate at the frequency where its Q-factor is maximum when it is connected to the appropriate capacitor. The radius of each CSCMR loop that resonates at a certain resonant frequency, f_i, can be derived from (3.5) as

$$r_i = \frac{c^{4/3}\mu_0^{1/6}\rho^{1/6}}{4^{7/6}\ 15^{1/3}\pi^{11/6}r_{ci}^{1/3}\ f_i^{7/6}} \tag{3.33}$$

where r_{ci} is the cross-sectional radius of the loop. The lumped capacitance used to resonate this loop can be written as

$$C_i = \frac{4\cdot 15^{4/7}\pi^{8/7}r_{ci}^{4/7}r_i^{5/7}}{c^{16/7}\mu_0^{9/7}\rho^{2/7}\left[\ln\left(\frac{8r_i}{r_{ci}}\right)-2\right]}. \tag{3.34}$$

The TX and RX resonator loops of CSCMR systems can be designed using (3.33) and (3.34). However, no guidelines on how to pick the other geometrical parameters of CSCMR systems, such as, the radius of the source and load loops, r_1, and distance between the TX and RX subsystems, d. Therefore, an analysis is performed based on our analytical models to design optimal CSCMR systems that exhibit maximum efficiency.

In order to validate the analytical model and theoretical analysis, simulated models using ANSYS HFSS (as shown in Figure 3.6) and measurement are used to compare. In the simulated model, the red loops are the source and load loops with radius as r_1. The loops in blue color are the TX and RX resonators with radius represented as r_2. The distance between the TX element and RX element is expressed as d. In the following part, effects of different radius and various ranges on efficiency performance will be studied.

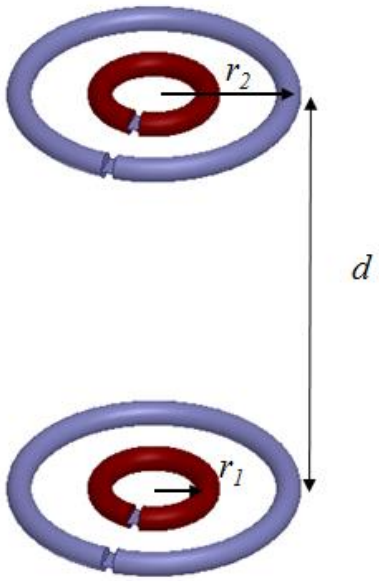

Figure 3.6. Simulated model of a CSCMR system with one pair of resonators.

3.2.1 Effect of Radius

Specifically, a CSCMR system is designed to operate at 158 MHz. First, the parameters of the TX and RX resonators are determined based on (3.33). Their cross-sectional radius, r_c, is chosen as 2.1 mm based on the copper used in the experiment. The radius of the outer loop, r_2, is calculated as 22.5 mm. The capacitance required to resonate these loops is calculated based on (3.34) as 14.94 pF. Using the analytical model discussed in section 3.1, the performance of designed CSCMR system can be predicted in terms of efficiency under various radii of the source and load loops. Figure 3.7 illustrates the dependence of CSCMR's efficiency on r_1. It can be seen that when r_1 is equal to 9 mm, the efficiency is maximum (i.e., 90%). Therefore, there is an optimal value for the radius of the source and load loops.

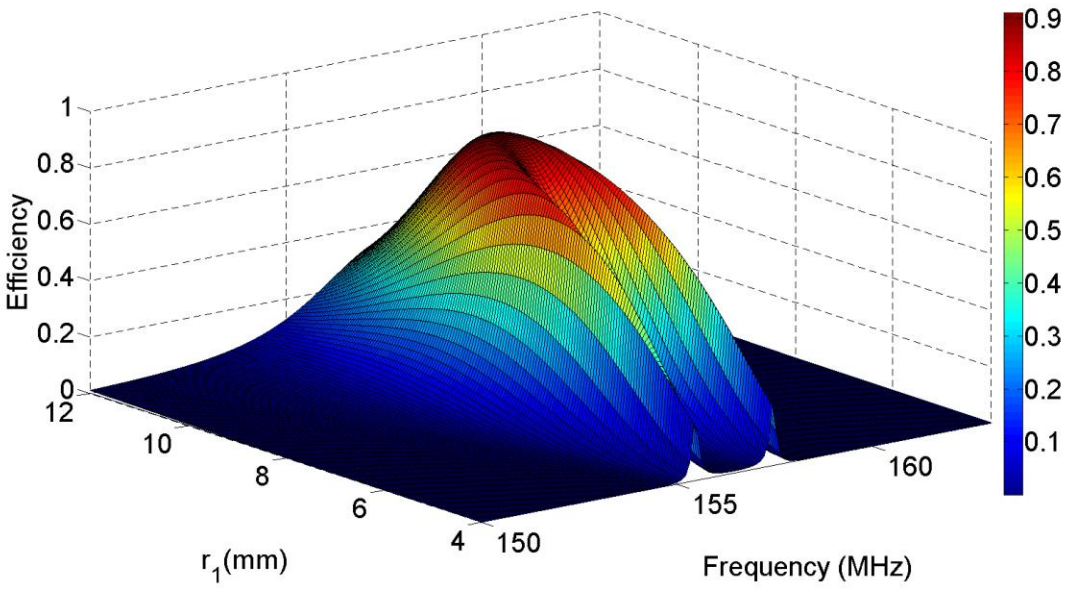

Figure 3.7. CSCMR's efficiency dependence on the radius of the source and load loops, r_1.

The simulation model using ANSYS HFSS swept different radii of the source and load loops, r_1 to validate the optimal value. From the simulated result in Figure 3.8, it is also shown that when r_1 equals 9 mm, the efficiency reaches the maximum value, around 86% at 158 MHz.

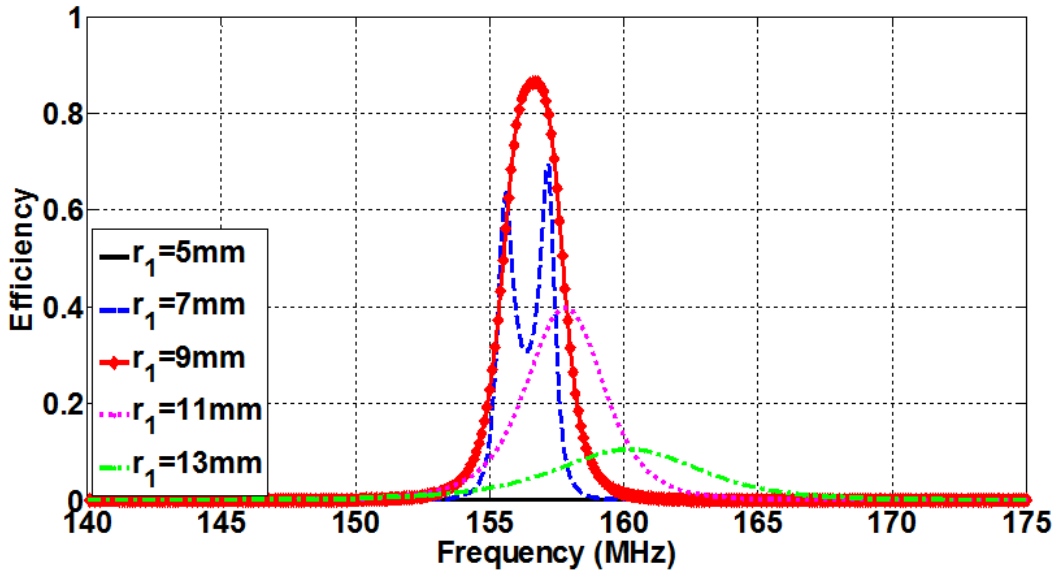

Figure 3.8. Simulated result in software ANSYS HFSS for various radii of r_1.

In order to validate the analytical and simulation results, measurement of the designed CSCMR WPT system is built to compare. The measurement setup is shown in Figure 3.9. The radii of the outer loops are 22.5 mm, which is determined by the operating frequency. The radii of the inner loops are chosen as 9 mm, which is the optimal value obtained from the theoretical and simulation study. The CSCMR WPT system is connected with the Vector Network Analyzer (VNA) E5061B. *S*-parameters can be obtained by VNA and the efficiency which is the square of the magnitude of S_{12} can be calculated.

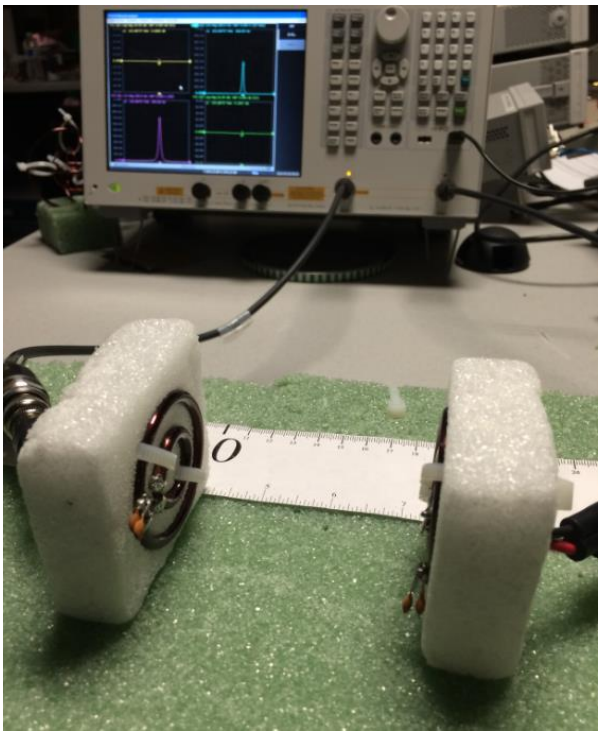

Figure 3.9. Measurement setup of the designed CSCMR WPT system.

Theoretical, simulation and measured efficiencies of the designed CSCMR WPT system are compared in Figure 3.10. It can be seen that the analytical and simulated results agrees well. The measured efficiency is a little lower than the theoretical and simulated ones. The measured operating frequency where the efficiency is maximum also shifts a little lower. This is because the actual capacitors we used in the experiment are not perfect and precise as the ones used in the analytical and simulation models.

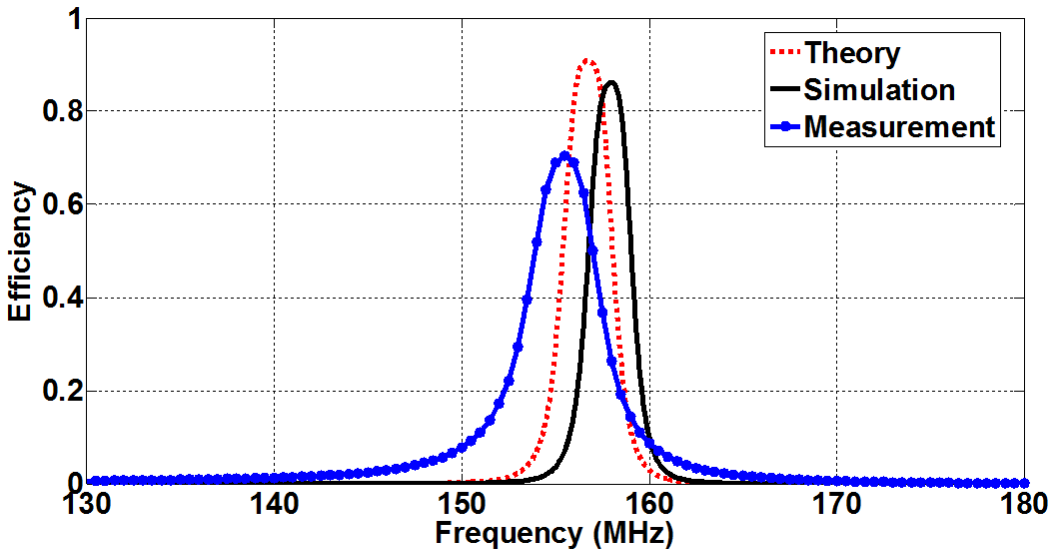

Figure 3.10. Efficiency of the designed CSCMR WPT system.

3.2.2 Effect of Range

The distance between the TX and RX elements also affects the system performance. Figure 3.11 illustrates the dependence of CSCMR's efficiency on the distance, *d*. It shows that when the range is too close, the resonance splits into two peaks. This is because over-coupling between the TX and RX resonators will happen when distance decreases. When TX and RX are placed far away, the efficiency will drop as the range increase. In order to get a single operating frequency band and a maximum efficiency, the distance, *d*, also has an optimal value. From Figure 3.11, the optimal value should be equal to around 80 mm.

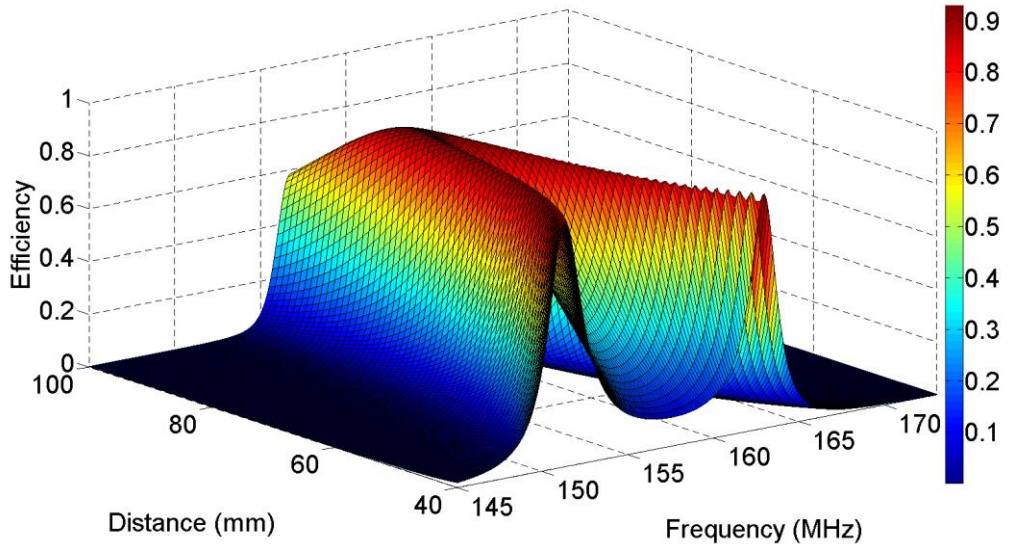

Figure 3.11. CSCMR's efficiency dependence on the distance, d, between the TX and RX subsystems.

Simulated results also show the same performance in Figure 3.12. When distance equals 80 mm, the efficiency is maximum and there is only one peak of the resonance.

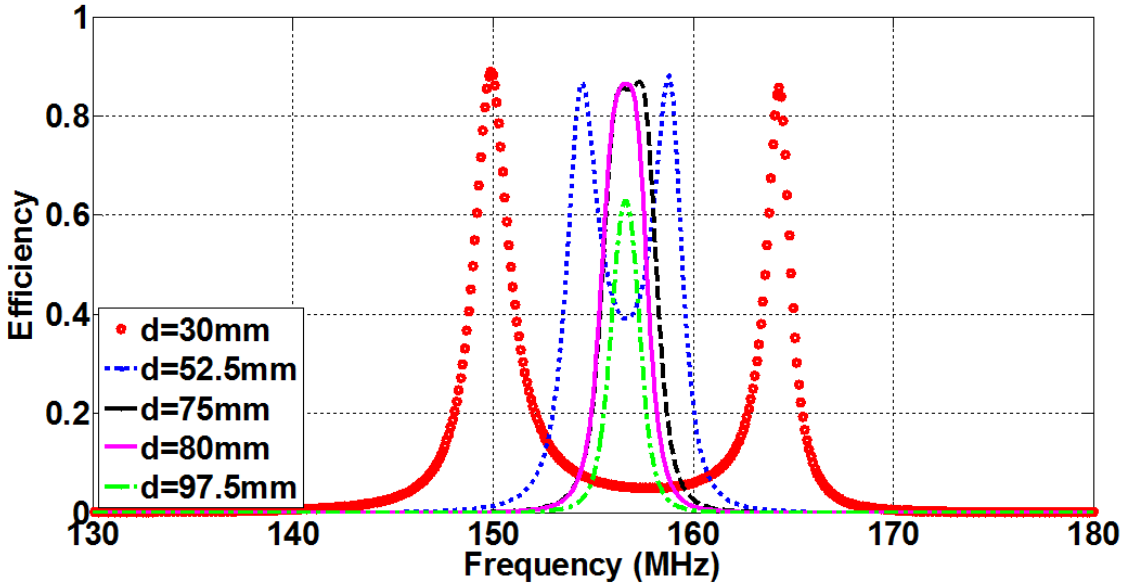

Figure 3.12. Simulated result regarding to various distances.

Experiment is fulfilled in Figure 3.13 in order to validate the theoretical and simulation results. Measured results as shown in Figure 3.14 illustrate similar results as the previous predications. For all the resonances with single peak, efficiency is the best when distance is 80 mm. When the distance is less than 80 mm, over-coupling appears.

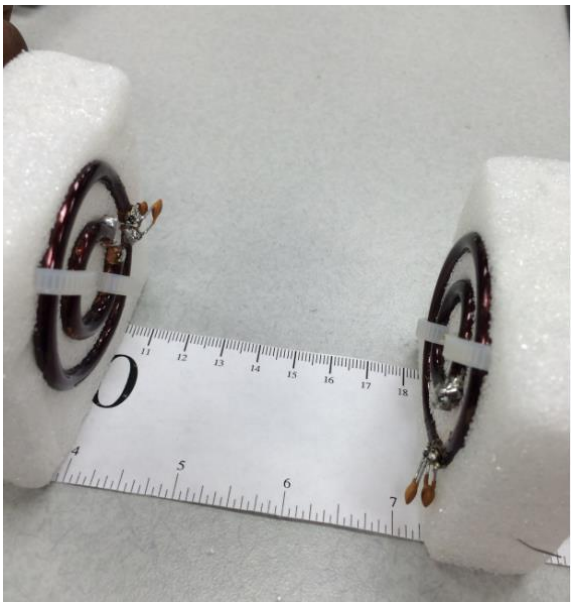

Figure 3.13. Measurement regarding to various distances.

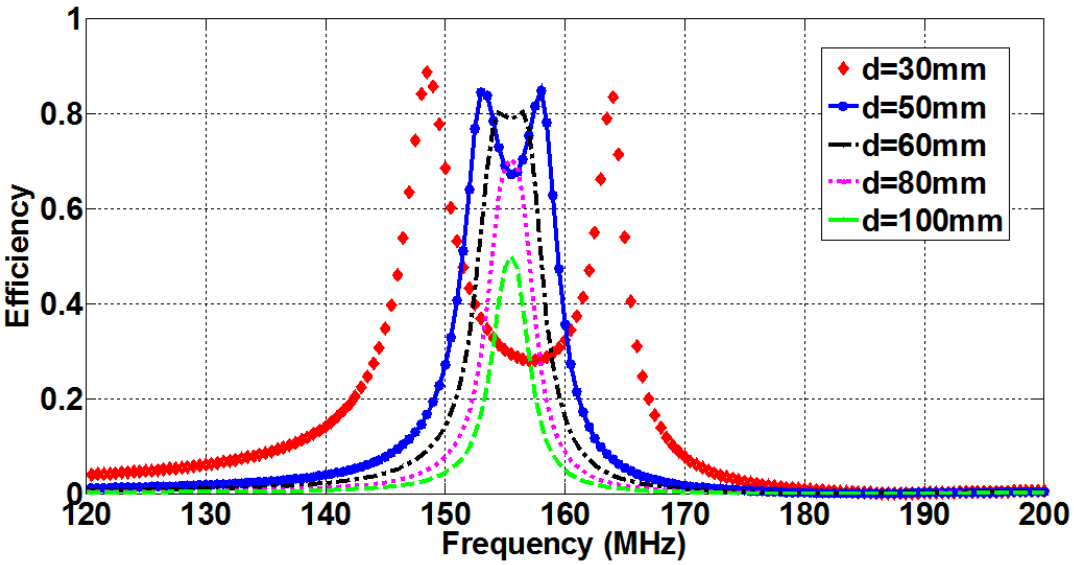

Figure 3.14. Measured efficiency regarding to different distances.

3.3 Optimal Design of SCMR WPT Systems with Two Pair of Resonators

3.3.1 Effect of Configuration

Three loops are used on the TX element and three loops on the RX element, as shown in Figure 3.15. One of the loops on the TX element will be connected to the source and one loop on the RX element will be connected to the load. The other two loops of the TX and RX elements are resonators. The source and load loops can be either the innermost, middle or outermost loops of the TX and RX elements, respectively. Figure 3.15 illustrates two of these ways to layout the CSCMR loops.

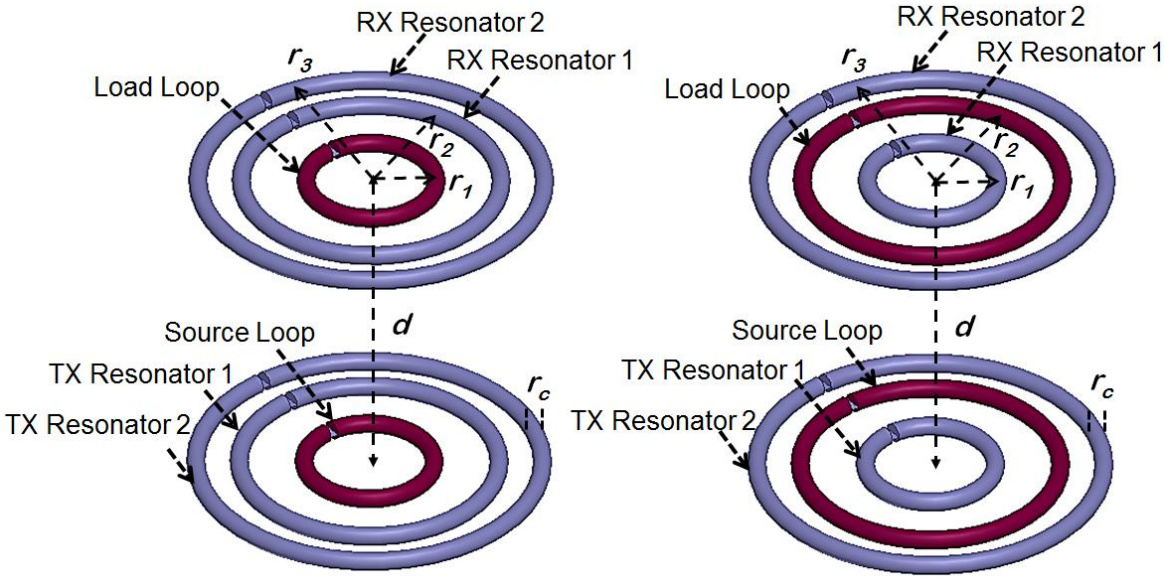

Figure 3.15. Different layout models of dual-band CSCMR systems. (a) The innermost loops are the source and load loops. (b) The middle loops are the source and load loops.

The efficiencies of the CSCMR systems for each layout are calculated using ANSYS HFSS and are compared in Figure 3.16. The geometric specifications of this system are: the cross-sectional radius of all loops, r_c, is 2.1 mm; the radii of the innermost (r_1), middle (r_2) and outermost loops (r_3) are 20 mm, 50 mm and 70 mm, respectively.

The distance between TX and RX is set to *d*=80 mm. Figure 3.16 illustrates that efficient dual-band CSCMR systems can be designed when the source and load elements are the innermost or middle loops since when the outmost loops are used as source and load loops there is only one efficiency peak.

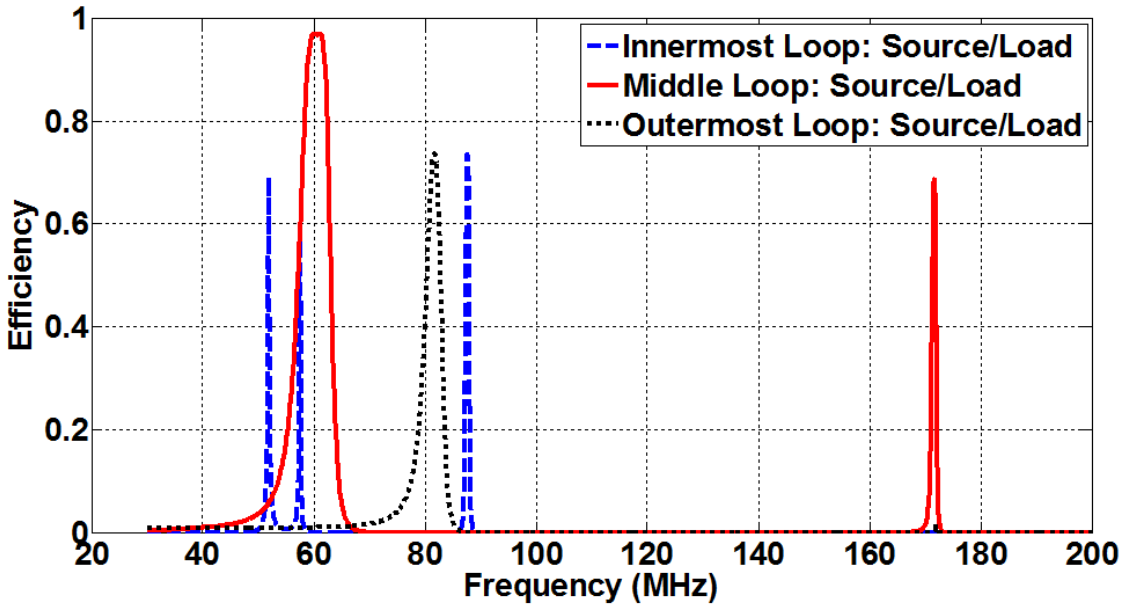

Figure 3.16. Simulated efficiency of different layout methods of CSCMR systems.

Specifically, when the innermost loops of TX and RX are used as source and load (see in Figure 3.16), the first CSCMR resonance occurs approximately at 55 MHz and it splits into two peaks. Each of the peaks has relatively narrow bandwidth (i.e., the 5 dB bandwidths of the first and second peak are 500 kHz and 200 kHz, respectively). The second resonance of this CSCMR system occurs at 88 MHz with a 5 dB bandwidth of 600 kHz. Therefore, there will be actually three narrow WPT channels with this layout method.

When the middle loops of TX and RX are used as source and load (see in Figure 3.16), the two efficiency peaks are located at 60 MHz and 172 MHz. Also, the first

resonance has broader bandwidth (a 5 dB bandwidth of 9 MHz). The two bands of this CSCMR system can be easily tuned independently. Therefore, dual-band CSCMR systems, which use their middle loops as sources and loads, will be used in the rest of this analysis. It should be also pointed out that the efficiency at the second resonance (i.e, 172 MHz) is smaller than the efficiency at the first resonance (i.e., 60 MHz). This can be potentially attributed to different reasons, such as, skin effect, proximity effects and electrical separation between TX and RX, which are examined individually here. The loss resistance of a conductor increases as the frequency increases due to the skin effect. However, the resonator loops corresponding to the second resonance (i.e., higher frequency) have smaller radius than the resonator loops corresponding to the first resonance. In fact, when (3.2), (3.3) and (3.33) are used at the second resonance, the total resistance of the corresponding resonators is found to be smaller than the total resistance of the resonators corresponding to the first resonance. Therefore, the skin effect is not the reason for the reduced efficiency at the second resonance. Also, the spacing between the loops of the TX or RX is significantly larger than the cross-sectional radius of the loops thereby limiting the significance of proximity effects. Finally, at the second resonance (higher frequency) the TX and RX are located further apart electrically compared to the first resonance (lower frequency), since the wavelength decreases with increasing frequency. This results in reduced efficiency at the second resonance. In order to prove this point, the efficiency of the CSCMR system of Figure 3.15(b) is examined for different distances between TX and RX. Figure 3.17 illustrates these results and proves that the efficiency at the second resonance increases to a value similar to the efficiency at the first resonance when the distance between TX and RX is reduced from 80 mm to

50 mm. Therefore, it can be concluded that the efficiency degradation observed at the second resonance (see Figure 3.16) is primarily due to the increased electrical distance between TX and RX.

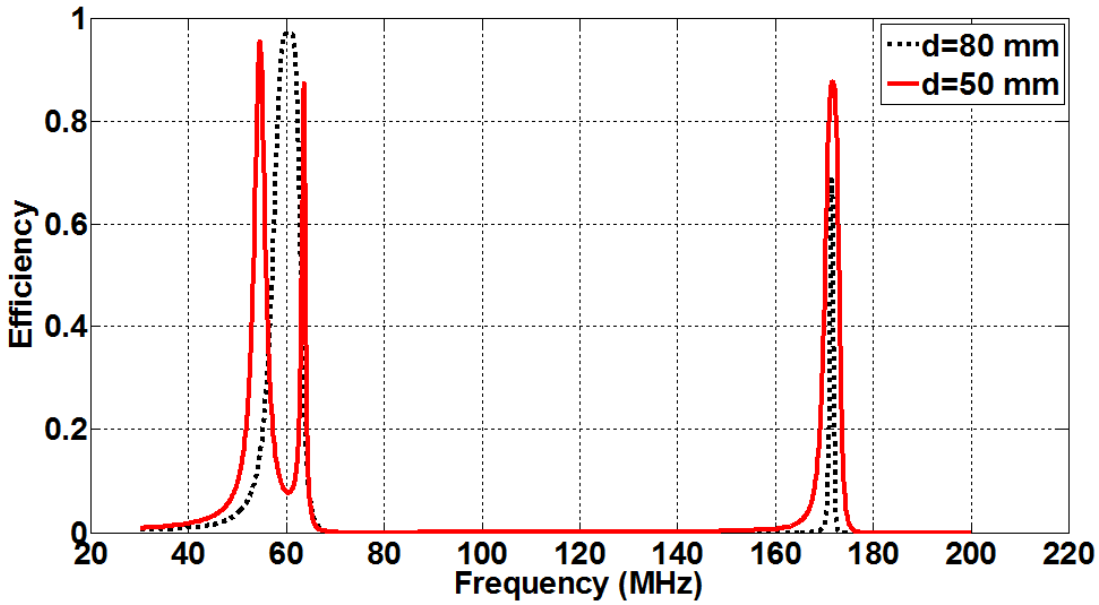

Figure 3.17. Simulated efficiency of CSCMR system of Figure 3.15(b) at different distances.

Also, Figure 3.18 shows the simulated distribution of the magnetic field in ANSYS HFSS at the first resonance of the system of Figure 3.15(b). Figure 3.18 illustrates that as expected the pair of resonators #2, shown in Figure 3.15(b), exhibits the highest magnetic coupling at the first resonance.

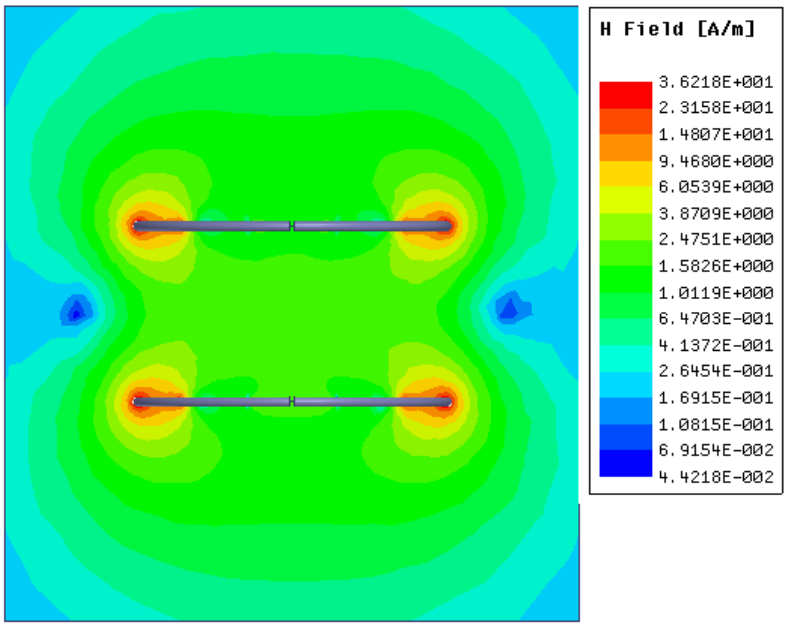

(a)

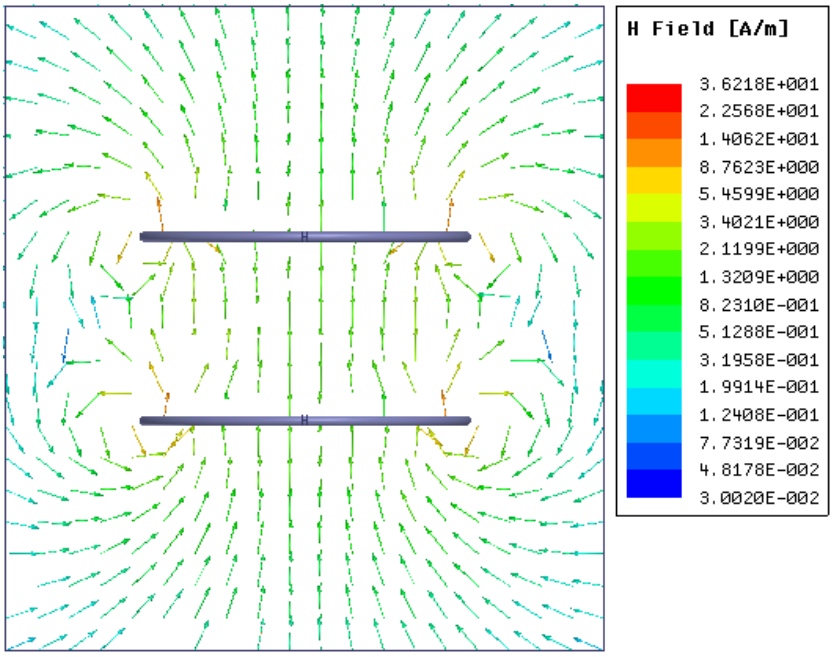

(b)

Figure 3.18. Distribution of the magnetic field, H, at the first resonance of the system of Figure 3.15(b). (a) Magnitude of H. (b) Vector of H.

3.3.2 Effect of Radius

In the proposed dual-band CSCMR system, the lower resonant frequency is mainly determined by the geometric parameters of the larger loop and the higher resonant frequency is mainly determined by the parameters of the smaller loop. The resonators can be designed using (3.33), (3.34). Also, other parameters, such as, the radii and cross-sectional radii of the source and load loops also have an effect on the system's performance.

In order to better understand the effects of these parameters, a dual-band CSCMR system, shown in Figure 3.19, is designed and analyzed. This system is designed to work at 63 MHz and 150 MHz. The middle loops of the TX and RX are chosen to function as the source and load loops, respectively. The cross-sectional radii of innermost and outermost loops, r_{c1} and r_{c3}, are equal to 2.1mm. Based on (3.33) and (3.34), the radii of the innermost and outermost loops (i.e., resonators) are calculated as r_1=23 mm and r_3=65 mm, respectively, and the capacitances for the innermost and outermost loops are C_1=15 pF and C_3=22 pF, respectively. The TX and RX elements are initially placed at a distance, d, equals to 70 mm. The source and load loops have the same radius, r_2, and cross-sectional radius, r_{c2}, due to the symmetry of the TX and RX. The analytical model that was presented in Section II is used to calculate the efficiency of this system for different values of the radius, r_2, and cross-sectional radius, r_{c2}.

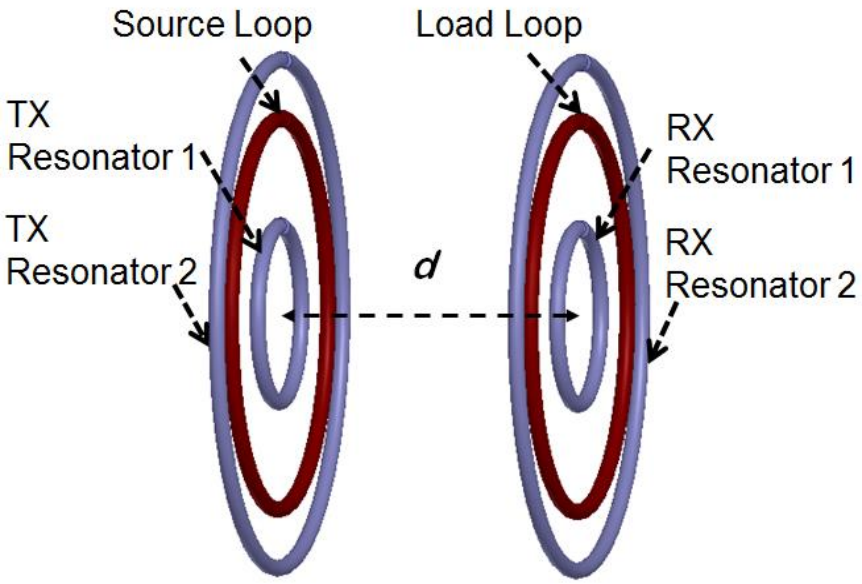

(a)

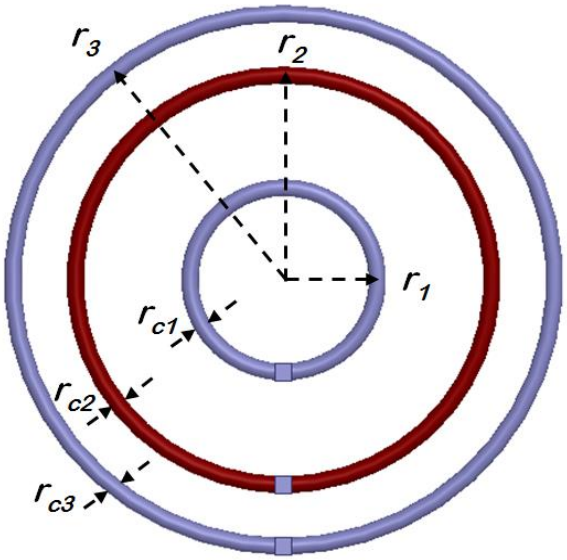

(b)

Figure 3.19. Configuration for a typical dual-band CSCMR. (a) Side view. (b) Top view.

Figure 3.20 illustrates the variation of the efficiency versus frequency and the radius, r_2, when r_{c2}=2.1 mm. Figure 3.20 shows that when the radius of the source and

load loops, r_2, is too small (less than twice the radius, r_1, of the innermost resonating loop): (a) the first resonance splits more distinctly into two peaks since the null between these peaks becomes deeper, and (b) the second resonance of the dual-band system does not appear. Figure 3.20 shows that maximum efficiency is achieved at the second resonance (i.e., 150 MHz) when the radius, r_2 is equal to 52 mm.

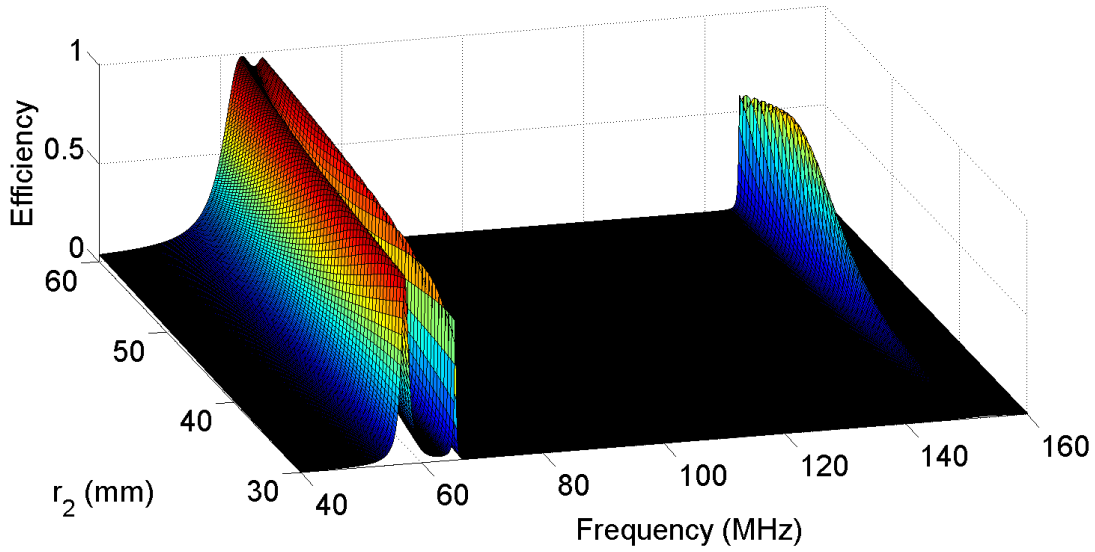

Figure 3.20. Analytical results for different radii of exciting loops (r_c=2.1 mm, d=70 mm).

Figure 3.21 illustrates the variation of the efficiency versus frequency and the cross-sectional radius, r_{c2}, when r_2=52 mm. Figure 3.21 shows that when the cross-sectional radius, r_{c2}, of the source and load loops equals 1 mm, the efficiency reaches its maximum value of 62% at the second resonance. Also, it is observed again that when r_{c2} is smaller than 2 mm the first resonance splits more distinctly into two peaks since the null between these peaks becomes deeper. Therefore, in order to have two resonances with high efficiency and without severe splitting (i.e., no deep nulls), the optimal value of r_{c2} as 2.1 mm was used.

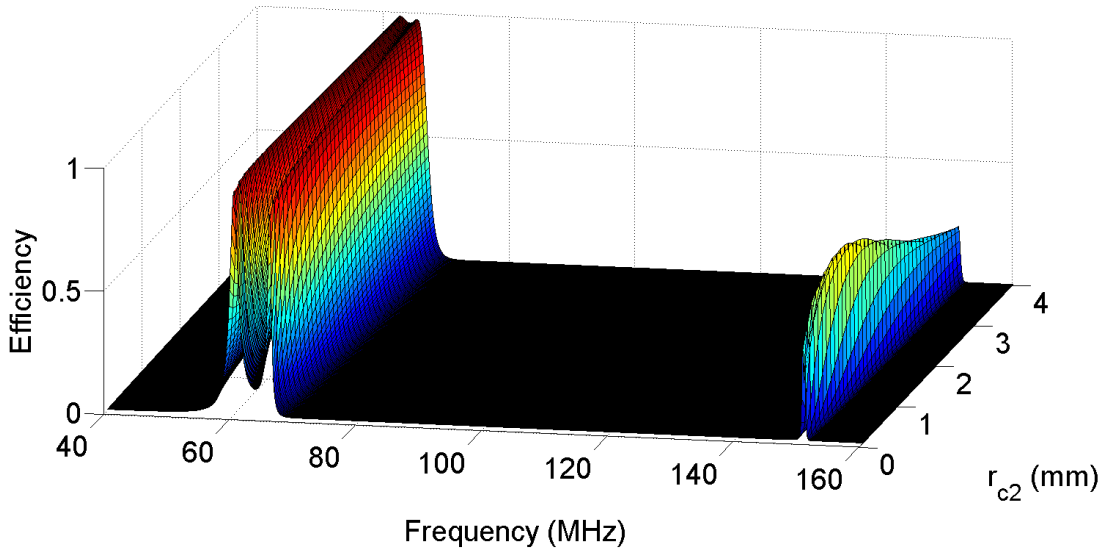

Figure 3.21. Analytical results for different cross-sectional radii of exciting loops (r_2=52 mm, d=70 mm).

3.3.3 Effect of Range

The optimal distance is also found using the analytical results, similarly to the analysis performed for the optimal radii. Figure 3.22 illustrates the variation of the efficiency versus frequency and distance between TX and RX. The optimum values of r_2=52 mm and r_{c2} =2.1 mm were used according to the previous discussion. Figure 3.22 shows that when the distance between TX and RX is larger than 70 mm, the efficiency at the second resonance drops significantly. However, when the distance is smaller than 100 mm, the first resonance splits distinctly into two peaks since the null between these peaks becomes deeper. Therefore, the distance was picked to be 70 mm, as a compromise between achieving good efficiency at the second resonance and avoiding a severe split of the first resonance. It should be pointed out that for a set distance between TX and RX, the electrical distance between the TX and RX at the first (lower frequency) resonance is

shorter than the electrical distance at the second (higher frequency) resonance. Therefore, it is justified that the WPT efficiency at the second resonance is smaller than the efficiency at the first resonance for the same physical distance.

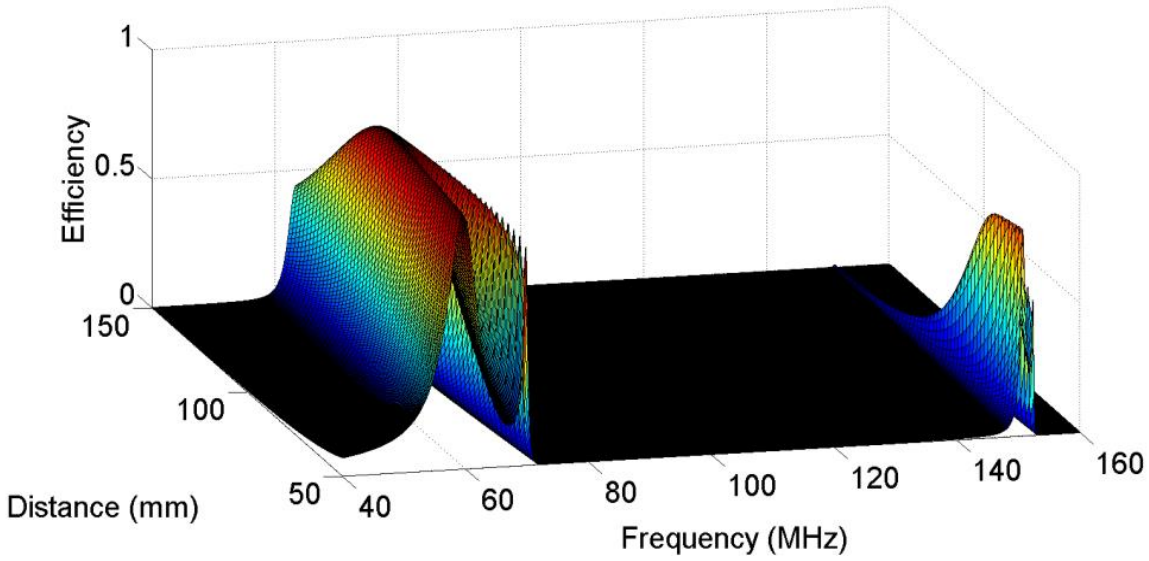

Figure 3.22. Analytical results for different distances between TX and RX (r_2=52 mm, r_c=2.1 mm).

CHAPTER 4

MULTIBAND AND BROADBAND CSCMR SYSTEMS

In this chapter, novel multiband and broadband WPT systems based on Conformal SCMR (CSCMR) are developed and rigorously analyzed. In Section 4.1, optimal multiband CSCMR systems with two, three and four bands are examined in order to validate our analytical results through comparisons with simulations and measurements. In Section 4.2, broadband CSCMR systems are presented and design guidelines for optimal broadband CSCMR systems are developed and discussed. Finally, conclusions are drawn in Section 4.3.

4.1 Multiband CSCMR WPT System

Wireless power transfer systems, which can efficiently transmit power in different bands, may be used for applications where a single WPT TX system needs to power devices or sensors of different sizes at different distances. In such cases, lower operating frequencies will exhibit longer power transfer range and will require larger size WPT receivers for powering sensors and devices. Whereas, higher operating frequencies will exhibit shorter power transfer ranges and will require smaller size WPT receivers for powering sensors and devices. Also, multiband WPT systems can be used to provide compatibility with different WPT standards. Therefore, multiband WPT systems can be very useful for accommodating multiple standards as well as different receiver sizes and ranges.

The multiband SCMR WPT system is designed using the proposed theoretical model derived above. The CSCMR configuration is utilized in order to achieve planar

compact WPT systems. The operational frequencies of the multiband and broadband CSCMR systems are picked as examples so that designs can be developed, analyzed, built and validated. The proposed designs can be scaled and/or altered to cover other frequencies depending on the application. Multiband CSCMR systems can be potentially developed to be compatible with different WPT standards.

The proposed multiband WPT system will be based on CSCMR systems that use multiple pairs of different size loop resonators resonating at different frequencies thereby transferring power efficiently at multiple bands. The self-inductance of each loop resonator is solely determined by its geometric parameters. Therefore, each loop can resonate at the frequency where its *Q*-factor is maximum when it is connected to the appropriate capacitor. The radius of each CSCMR loop that resonates at a certain resonant frequency, f_i, can be derived from (3.33). The lumped capacitance used to resonate this loop can be calculated from (3.34).

4.1.1 Dual-band CSCMR System Design

The optimal dual-band CSCMR system, which was derived above, is now examined using the proposed theoretical model as well as simulation and measurements. The distance between the TX and RX is set as d=70 mm in order to achieve good efficiency in both frequencies as well as prevent resonance splitting. Figure 4.1 shows the prototype of this CSCMR system along with its geometric parameters according to the layout shown of Figure 3.19. Figure 4.2 compares the analytically calculated (using the formulation presented in Section 3.3), simulated and measured efficiency of this CSCMR

system. It can be seen that the analytical, simulated and measured results agree well thereby validating the proposed analytical formulation.

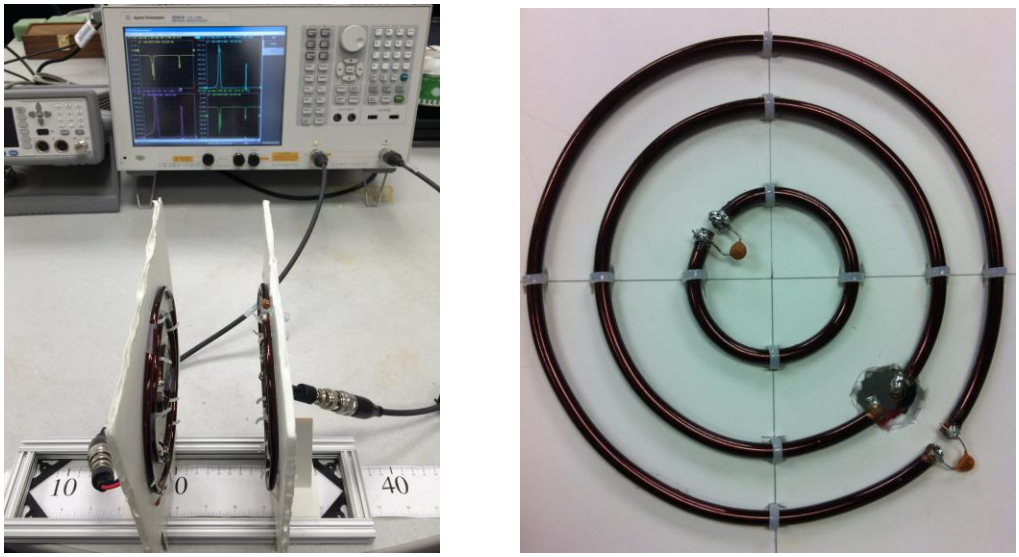

(a) (b)

Figure 4.1. A dual-band CSCMR system (d=70 mm, r_1=23 mm, r_2=52 mm, r_3=65 mm, r_c=2.1 mm, C_1=15 pF, C_3=22 pF). (a) Measurement setup. (b) TX or RX element.

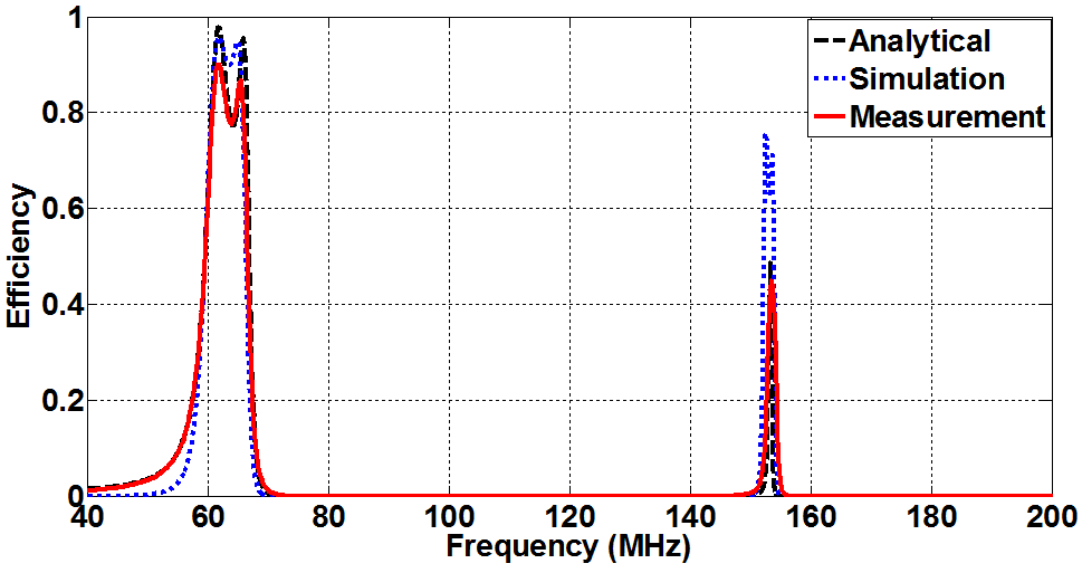

Figure 4.2. Efficiency of dual-band CSCMR system

Figure 4.3 illustrates the measured efficiency of this system for distances of 40 mm, 80 mm and 120 mm. These results are consistent with the theoretical results presented in the previous section and show that as the distance between TX and RX decreases the efficiency increases and also resonance splitting occurs for the distance of 40 mm.

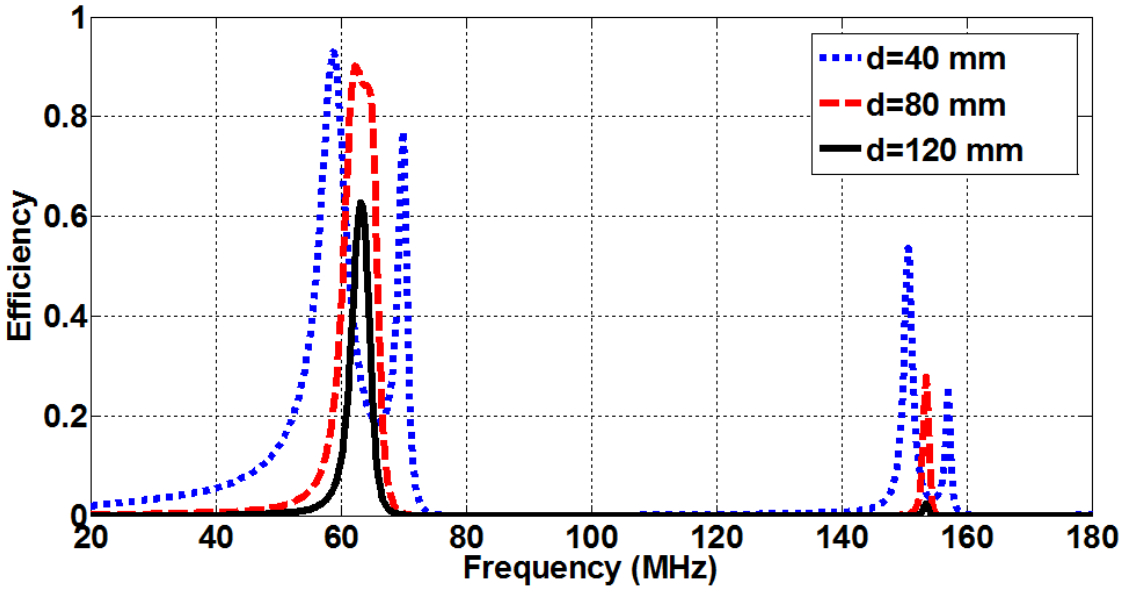

Figure 4.3. Measured efficiency of the dual-band CSCMR system versus distance between TX and RX.

4.1.2 Three-band CSCMR System Design

Three-band CSCMR system can be also designed by following the design procedure of the dual-band SCMR systems presented above. However, in the three-band CSCMR systems the innermost loops have to be used as source and load loops. Otherwise, only dual-band operation can be achieved. As discussed in the dual-band systems, when the source and load loops are the innermost loops, the first resonance splits into two peaks. A three-band CSCMR system (i.e., with three resonators) is initially

studied based on the analytical model. The topology of such a system is shown in Figure 4.4. The performance of the first resonance of this system for different values of the source/load loop radius, r_1, is shown in Figure 4.5. It is seen that in order to achieve a high efficiency at the first operating frequency of this system, the radius of the source/load loops should be larger than half the radius of the outermost resonator, r_4.

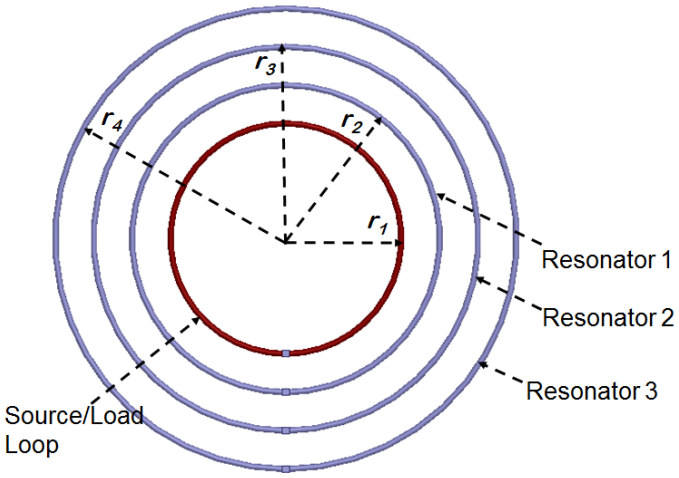

Figure 4.4. Geometry of a three-band CSCMR TX or RX.

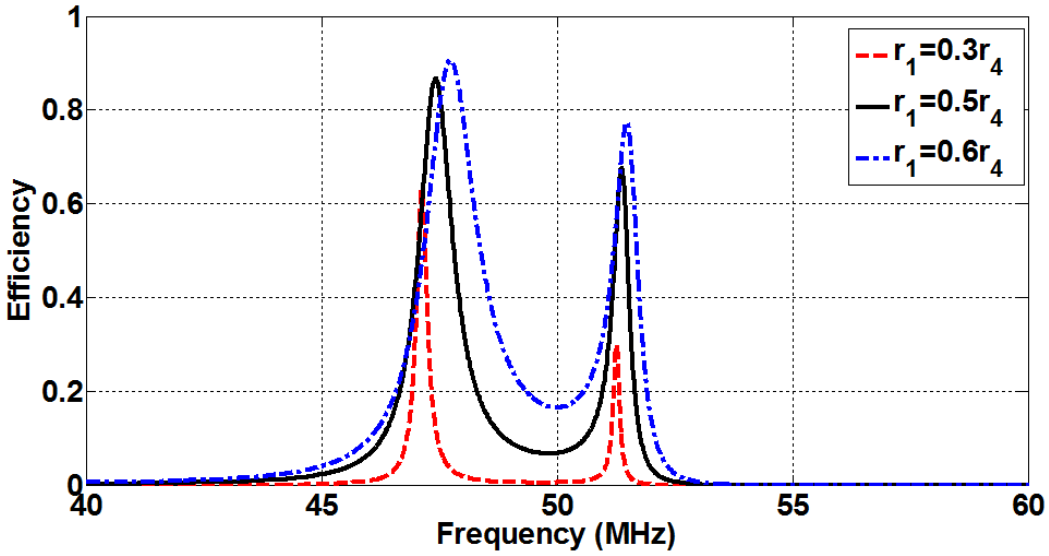

Figure 4.5. Analytical efficiency of the first resonance of a three-band CSCMR system for different values of the source/load loop radius, r_1.

A three-band CSCMR wireless power transfer system with three pairs of resonators is designed based on this conclusion. This system is designed to work at 50 MHz, 110 MHz and 200 MHz. The cross-sectional radius, r_c, of all loops is chosen as 0.8 mm. The radius of the source/load loop, r_1, is chosen as half the radius of the outermost radius, r_4, in order to achieve better performance. Also, in order to avoid overlapping of adjacent loops $r_3 > r_2 > r_1$ and since $r_1 = r_4/2$ and $r_4 > r_3$ the radii of the three resonator loops should satisfy the following relation:

$$r_3 > r_2 > \frac{r_4}{2} > \frac{r_3}{2}. \tag{4.1}$$

The radii of the resonator loops and the corresponding lumped capacitances can be calculated using (3.33) and (3.34). However, the radius of the resonator loop that operates at 50 MHz is too large (theoretical radius, r_4, is 117 mm) and the radius of the resonator loop that operates at 200 MHz is smaller (theoretical radius, r_2, is 23 mm) than the radius of the source/load loop. Therefore, these two radii of the resonator loops are selected based on (4.1) in order to make the design practically realizable. The corresponding lumped capacitors also need to be changed from their theoretical optimal values in order to resonate the loops at the required operating frequencies (thereby sacrificing the efficiency of the WPT system).

The radius of the middle loop (r_3) is calculated as 48 mm with a lumped capacitor (C_3) of 8.6 pF in order to resonate this loop at 110 MHz. Based on (4.1), the radii of the lower and higher band resonators can be chosen within the ranges: 24 mm < r_2 < 48 mm and 48 mm < r_4 < 96 mm. In order to design a compact three-band CSCMR system, the

radii of the lower and higher band resonators are chosen to be r_2=40 mm and r_4=60 mm. In order to make the system operate at 200 MHz and 50 MHz, the corresponding lumped capacitors are calculated to be C_2=3.2 pF and C_4=31 pF, respectively. Also, the radius of the source/load loop (r_1) is 30 mm, which is half the radius of the outermost radius. The distance, d, between TX and RX is 80 mm. The simulation model of this three-band CSCMR system is shown in Figure 4.6. Figure 4.7 illustrates the measured efficiency of this system for four different distances. It is seen that when the distance decreases, the efficiency at the third resonance increases. This occurs because at higher frequencies the loops are located electrically further apart compared to the lower frequencies, since the wavelength decreases with increasing frequency. This is similar observation, as the one discussed for the dual-band system.

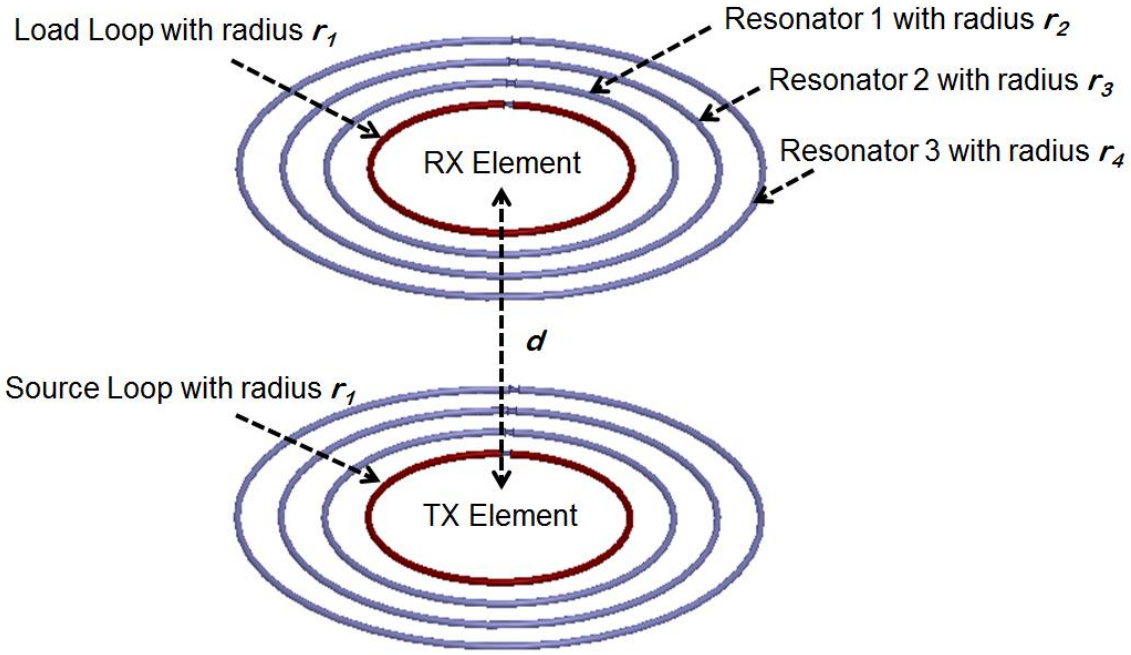

Figure 4.6. Simulation model of three-band CSCMR system (r_1=30 mm, r_2=40 mm, r_3=48 mm, r_4=60 mm, r_c=0.8 mm, d=80 mm, C_2=3.2 pF, C_3=8.6 pF, C_4=31 pF).

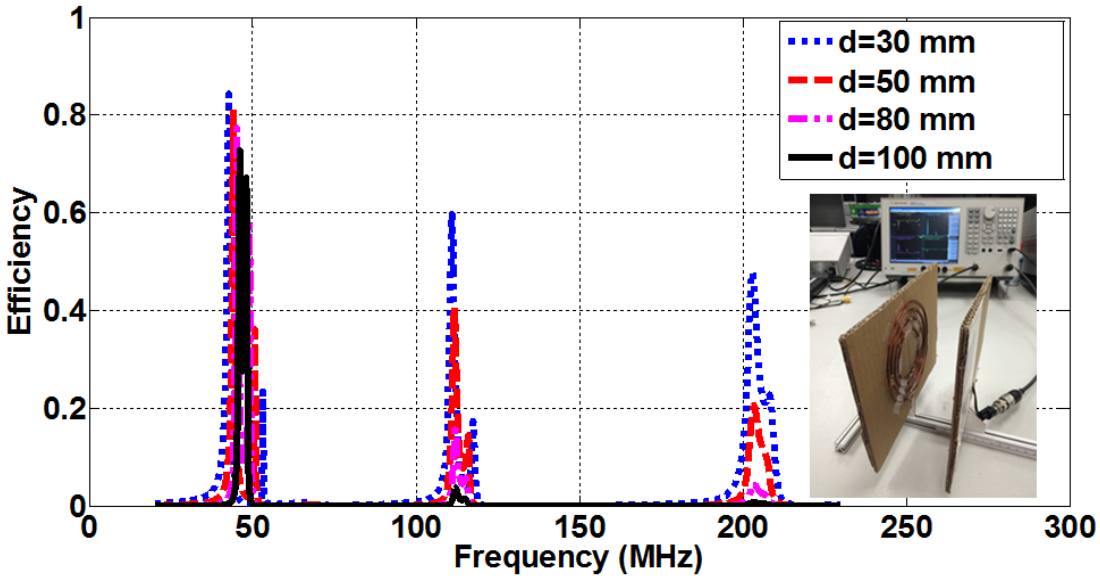

Figure 4.7. Measured efficiency of three-band CSCMR system for different distances.

4.1.3 Four-band CSCMR System Design

Four-band or other multi-band systems can also be designed following the same design procedure with four or more pairs of resonators. A smaller loop with 20 mm radius is added into the previous three-band SCMR system to perform as source/load loop for a four-band SCMR system. The four-band system is designed to work at 50 MHz, 110 MHz, 200 MHz and 300 MHz. The simulation model and specifications of this design are shown in Figure 4.8. The simulated and analytical results for the efficiency of this four-band CSCMR system are shown in Figure 4.9. Figure 4.10 illustrates the analytically calculated efficiency of this system for two different distances. It can be observed that when the distance is decreased to 50 mm, the efficiency increases significantly at the higher resonances and frequency splitting occurs at the first three resonances. This splitting results in more than four narrow-band WPT channels with 5 dB bandwidth between 200-1000 KHz for each channel.

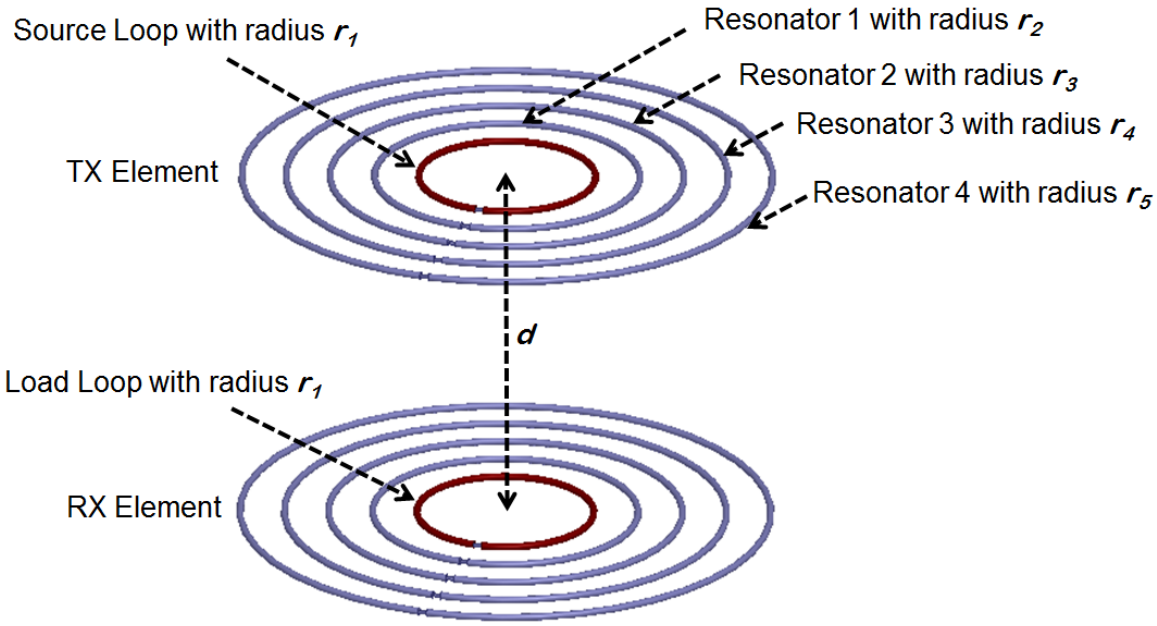

Figure 4.8. Simulation model of three-band CSCMR system (r_1=20 mm, r_2=30 mm, r_3=40 mm, r_4=48 mm, r_5=60 mm, r_c=0.8 mm, d=80 mm, C_2=2.4 pF, C_3=3.2 pF, C_4=8.6 pF, C_5=31 pF).

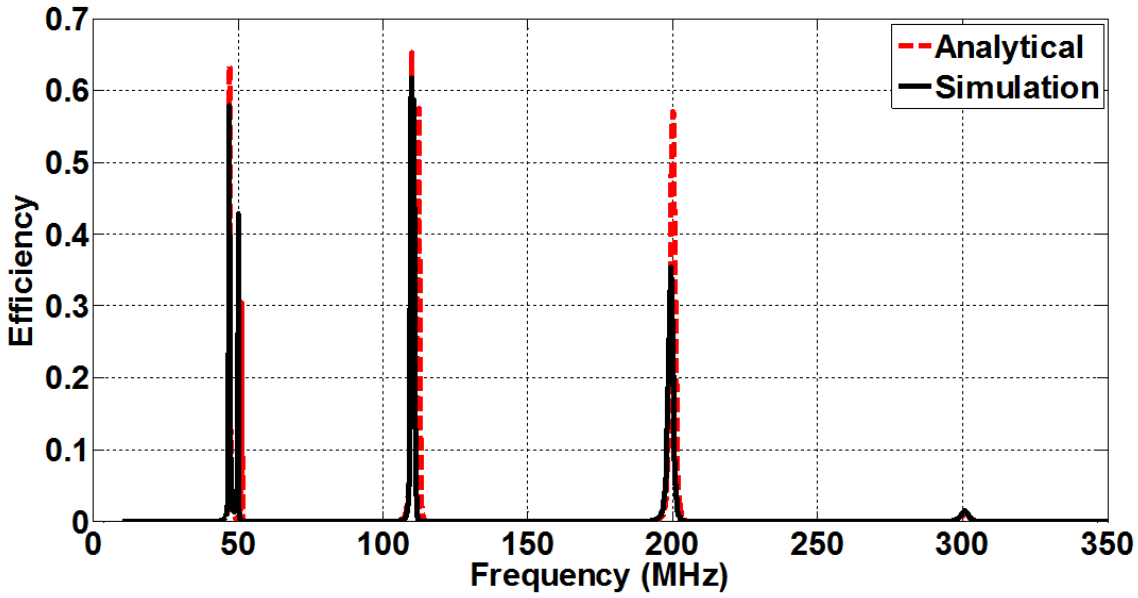

Figure 4.9. Efficiency of four-band CSCMR system.

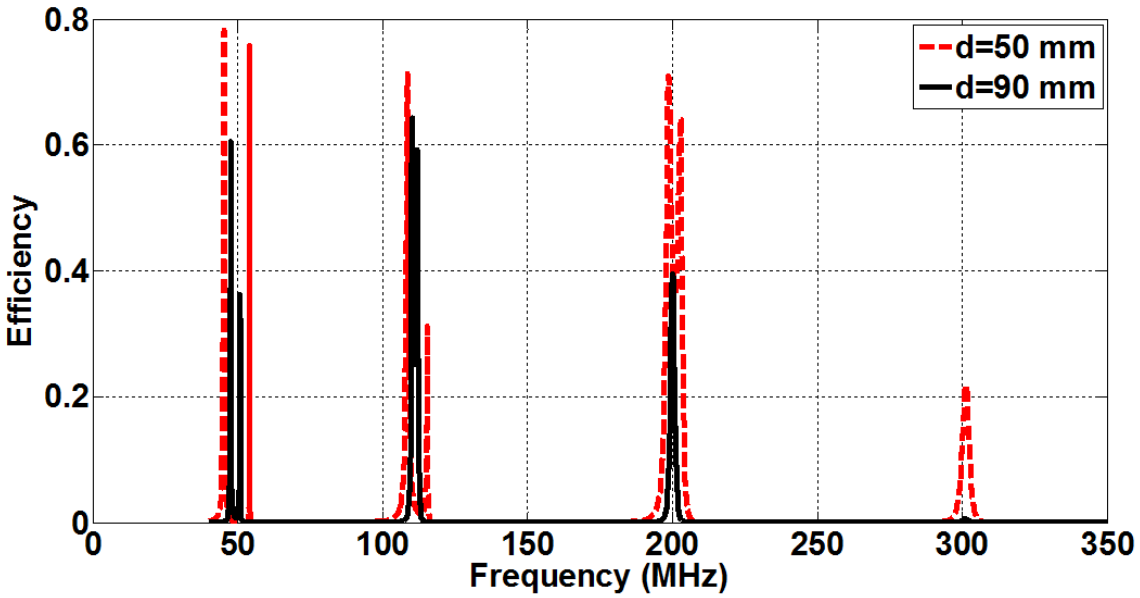

Figure 4.10. Analytically calculated efficiency of four-band CSCMR system for different distances.

4.2 Broadband CSCMR WPT System

In this section, a broadband CSCMR design is presented. WPT systems that are multiband are of great interest as they can power multiple sensors for different applications. Furthermore, broadband WPT systems can support simultaneous powering and communication through the same wireless link thereby enabling autonomous (i.e., battery-less) sensors.

4.2.1 Broadband CSCMR Design

The proposed broadband CSCMR system consists of three loops in each TX/RX. It is observed from Figure 4.11 that two resonances occur near each other when the innermost loops are chosen as the source and load loops. Therefore, in order to merge several resonant frequency bands of the multiband CSCMR method into one, the

innermost loops were used as the load and source loops for this broadband CSCMR design. There are two ways to realize this.

The first method is to use two resonators with different radii (r_i) and different cross-sectional radii (r_{ci}) so that they will resonate at the same frequency at which they exhibit maximum *Q*-factor. In this way, maximum *Q*-factor will be achieved by both resonators at the same frequency. In order to make the two frequencies equal, the relationship between the loop radius (r_i) and the cross-sectional radius (r_{ci}) is derived based on (3.5) as

$$\frac{r_{ci}}{r_{cj}} = \left(\frac{r_j}{r_i} \right)^3 . \tag{4.2}$$

Equation (4.2) shows that the inner resonator loop with smaller radius should have a much larger cross-sectional radius than the outer resonator loop in order to satisfy this condition. An example of such topology for a CSCMR TX or RX is shown in Figure 4.11.

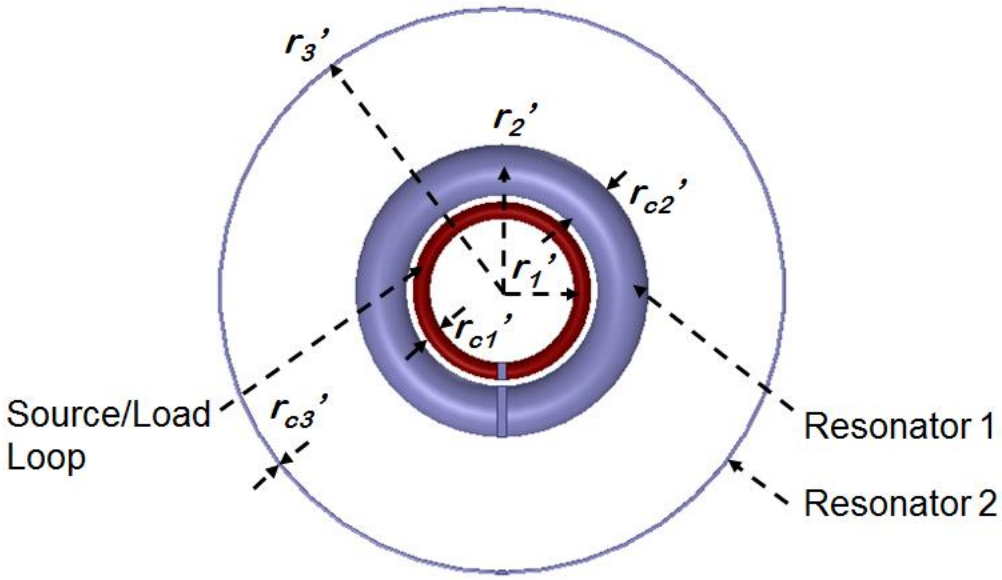

Figure 4.11. Geometry of a broadband CSCMR TX or RX for method 1.

The second method changes the capacitors that are connected to the two resonators so that their resonant frequencies will be equal. The geometry of this method is shown in Figure 4.12. In this way, the model is easier to build, but one of the loops will not resonate at exactly the frequency where its *Q*-factor is maximum. This will reduce the transmission efficiency of the CSCMR system, but it will significantly broaden its bandwidth.

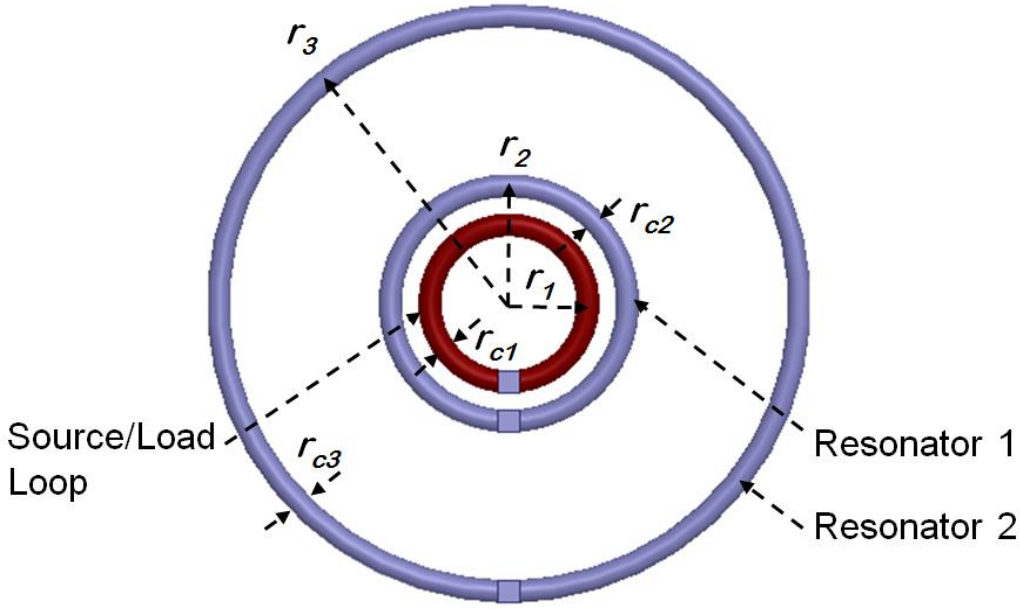

Figure 4.12. Geometry of a broadband CSMR TX or RX for method 2.

First, the impact of various parameters on the system performance is studied. The second method (Figure 4.12) is chosen due to its practicality to design a broadband CSCMR system operating at 155 MHz. The cross-sectional radius of all the loops (r_{c1}=r_{c2}=r_{c3}) is chosen as 2.1 mm. The middle loop is picked as the resonant loop that will resonant at 155 MHz, where its Q-factor is maximum. Therefore, the radius of the middle loop, r_2, is calculated as 22.5 mm using (3.33). The corresponding lumped capacitance

can be calculated using (3.34). The distance between TX and RX is chosen to be 70 mm. Figures 4.13 and 4.14 show the efficiencies of this CSCMR system for different ratios r_2/r_1 and r_3/r_2. These results illustrate that when r_2 is fixed, the ratio r_2/r_1 is 1.4, and the ratio of r_3/r_2 is 2.5 (i.e., r_1 is 0.71 times r_2, and r_3 is 2.5 times r_2), the performance of the CSCMR system is the best in terms of both the flatness and bandwidth of the efficiency.

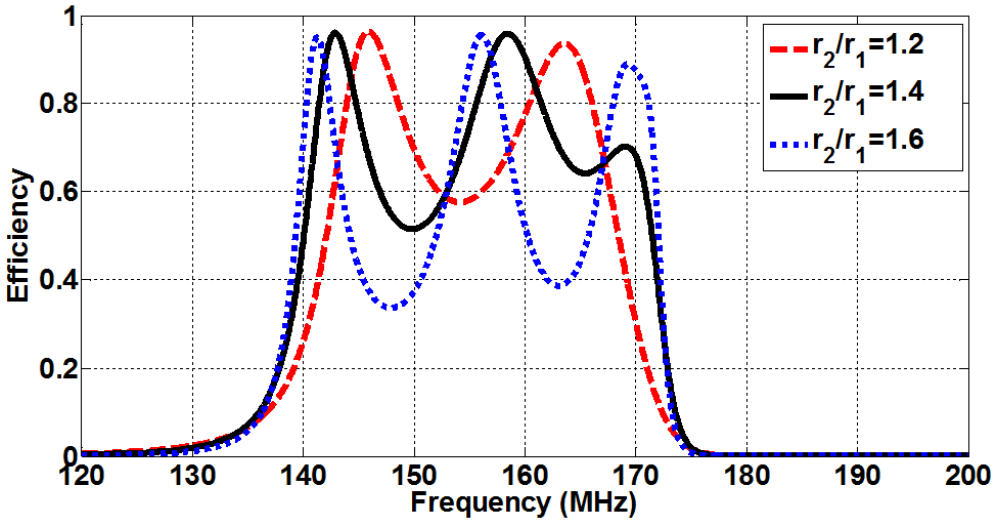

Figure 4.13. Efficiency of broadband CSCMR systems for different r_2/r_1.

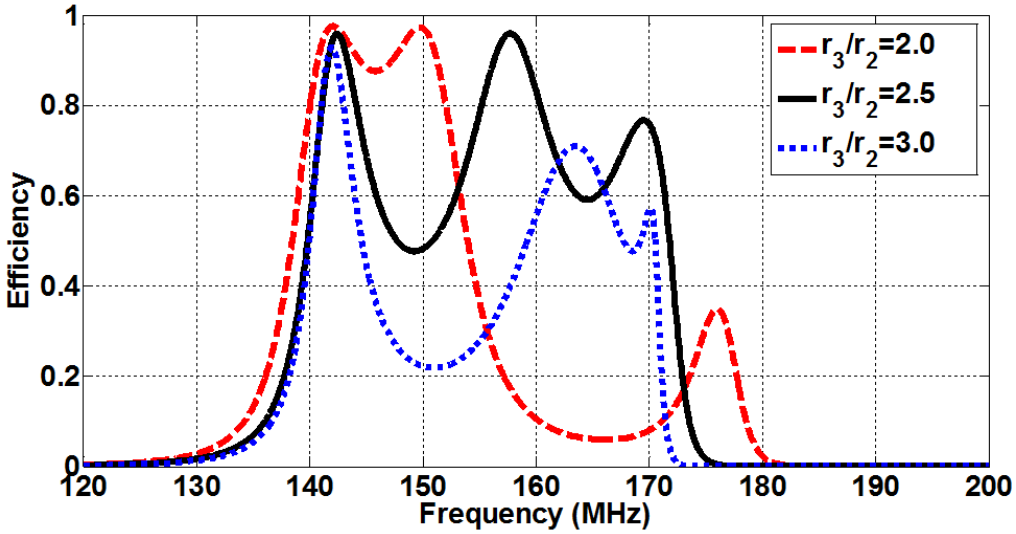

Figure 4.14. Efficiency of broadband CSCMR systems for different r_3/r_2.

Also, the cross-sectional radii, r_{c1} and r_{c3}, of the innermost and outermost loops, affect the performance of the CSCMR system. Figure 4.15 shows the efficiency of a broadband CSCMR design with the following parameters for different values of r_{c1}: r_1=16 mm, r_2=22.5 mm, r_3=56.25 mm, r_{c2}=r_{c3}=2.1 mm, d=70 mm. Figure 4.15 shows that when r_{c1} increases, the flatness of the efficiency improves, but bandwidth stays the same. Figure 4.16 shows when r_{c3} increases, the bandwidth increases, but the flatness of the efficiency stays approximately the same. Therefore, in order to improve the flatness of the efficiency and bandwidth, the cross-sectional radii of the innermost and outermost loops should be as large as possible.

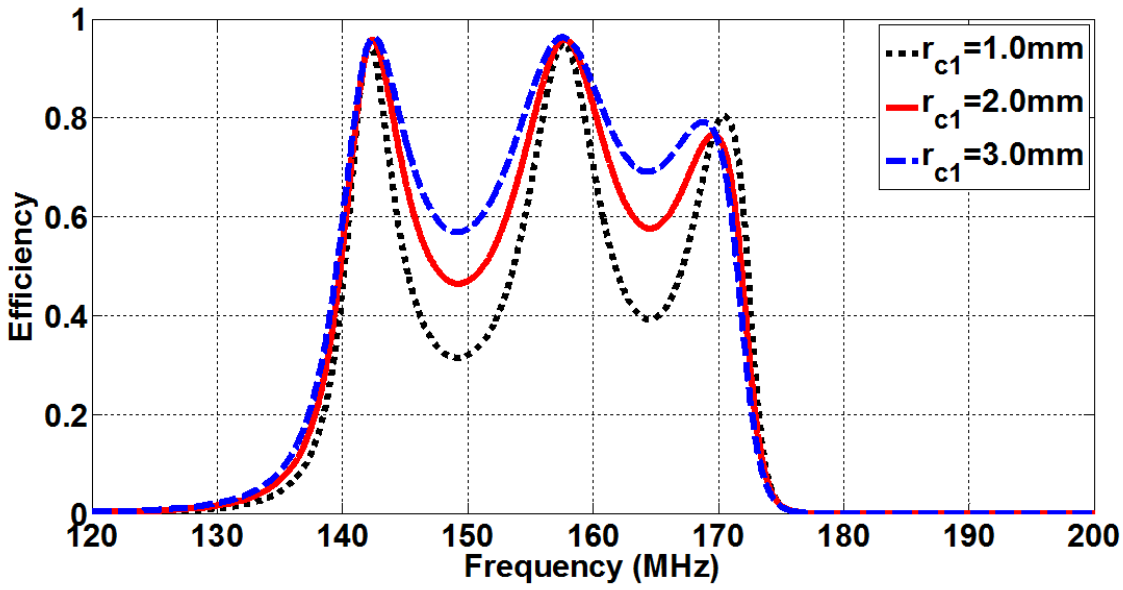

Figure 4.15. Efficiency of broadband CSCMR for different r_{c1} (r_1=16 mm, r_2=22.5 mm, r_3=56.25 mm and r_{c2}=r_{c3}=2.1 mm, d=70 mm).

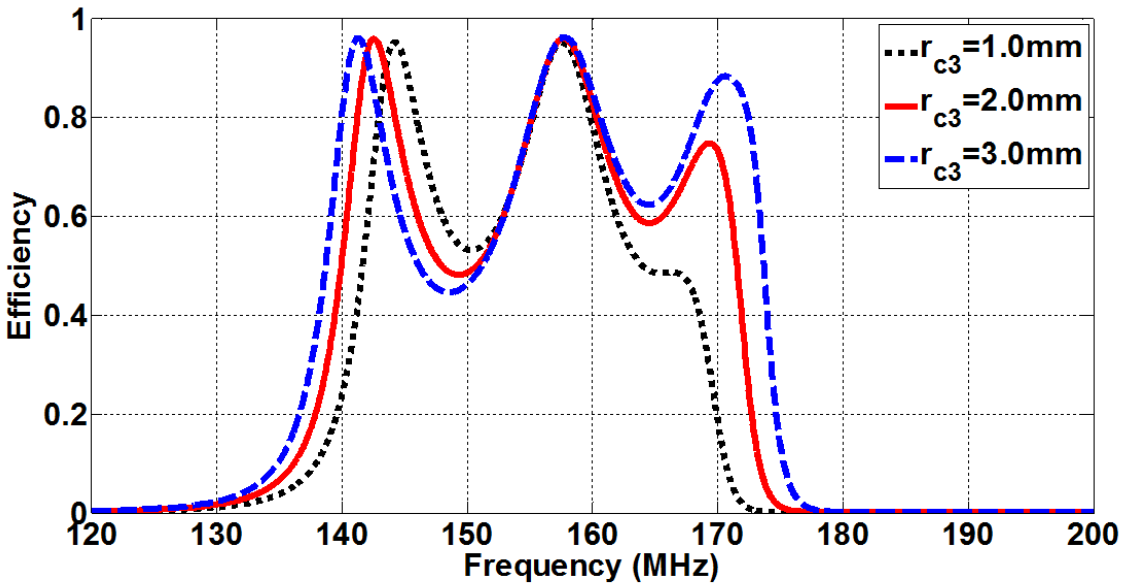

Figure 4.16. Efficiency of broadband CSCMR for different r_{c3} (r_1=16 mm, r_2=22.5 mm, r_3=56.25 mm and r_{c1}=r_{c2}=2.1 mm, d=70 mm).

The distance between TX and RX of CSCMR systems also affects their bandwidth. Figure 4.17 illustrates the variation of the efficiency of a broadband CSCMR system for different ratios of the distance to r_3. Figure 4.17 shows that the distance, d, between TX and RX should be chosen as 1.0–1.3 times the radius of the outermost loop, r_3, in order to achieve broader bandwidth and good efficiency. Similar results were derived for the geometrical parameters of first method (see Figure 4.11) that two resonators have different radii and cross-sectional radii.

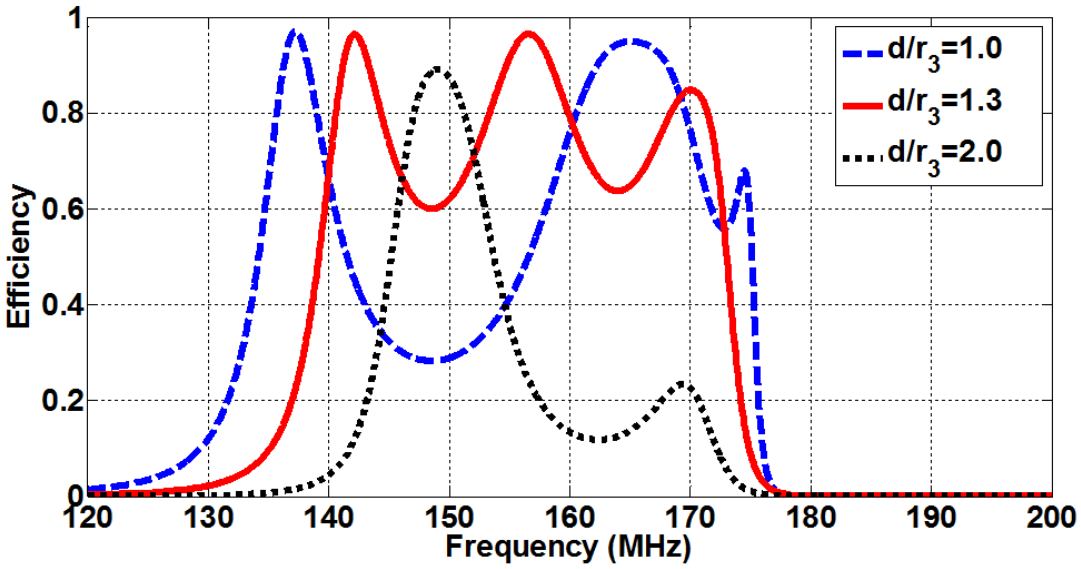

Figure 4.17. Efficiency of broadband CSCMR for different d/r_3 (r_1=16 mm, r_2=22.5 mm, r_3=56.25 mm and r_{c1}= r_{c2}=r_{c3}=2.1 mm).

Based on the above results and extensive analytical and simulation studies as well as measurements of various designs, it was concluded that in order to achieve broadband performance, the following criteria should be met: (a) the radius of source/load, r_1, should be 0.71 times the radius of the middle loop, r_2, (b) the radius of the outermost loop, r_3, should be 2.5 times the radius of the middle loop, r_2, (c) the distance between TX and RX, d, should be chosen 1.0–1.3 times the radius of the outermost loop, r_3, and 2.5–3.25 times of the radius of middle loop, r_2.

Therefore, based on these design criteria and condition (4.2), the cross-sectional radii of resonators 1 and 2 in the first method of Figure 4.11 should satisfy the relationship

$$r_{c2}^{'} = 15.625\, r_{c3}^{'}. \tag{4.3}$$

Also, the radius of resonator 1, r_2', should be 1.4 times the radius of source/load loop, r_1'. Therefore, in order to avoid overlapping of adjacent loops, the following condition should be satisfied:

$$0.4\, r_1^{'} > r_{c1}^{'} + r_{c2}^{'}\,. \tag{4.4}$$

In order to satisfy both conditions of (4.3) and (4.4), the cross-sectional radius of resonator 2 (r_{c3}') should be very small, otherwise, it will lead to overlapping of the source/load loop and resonator 1. Therefore, this type of broadband CSCMR cannot be easily designed in practice.

Based on the design criteria, broadband systems of the two methods operating at 300 MHz are designed and compared here. The geometric specifications of the CSCMR design of method 1 (see Figure 4.11) are: r_{c1}'=1.0 mm, r_{c2}'=1.6 mm, r_{c3}'=0.1 mm, r_1'=8.0 mm, r_2'=11.2 mm, r_3'=28 mm, d'=28.2 mm, C_2'=9.17 pF, and C_3'=1.32 pF. The geometric specifications of the CSCMR design of method 2 (see Figure 4.12) are: r_{c1}=r_{c2}=r_{c3}=1.1 mm, r_1=9.3 mm, r_2=13 mm, r_3=32.5 mm, d=42 mm, C_2=6.71 pF, and C_3=1.97 pF. Figure 4.18 shows that the second method delivers broader bandwidth. Therefore, the second method will be used in what follows to design broadband CSCMR systems; especially, after considering the fabrication difficulties of the first method.

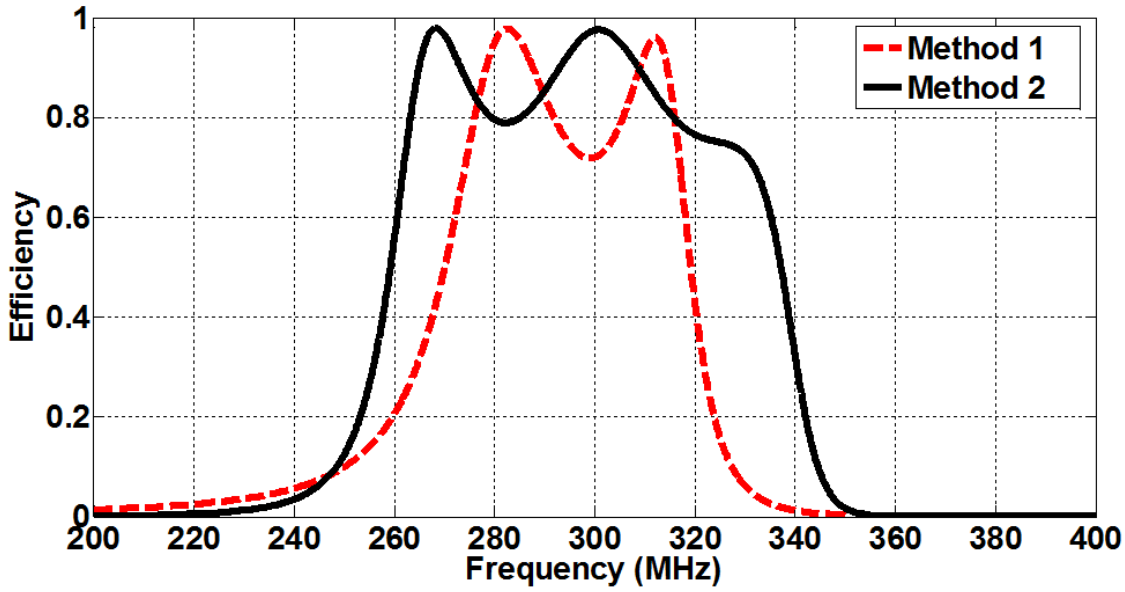

Figure 4.18. Comparison of broadband CSCMR systems based on methods 1 and 2.

For the second design method of broadband CSMCR, there are two choices for equating the two resonant frequencies of the resonators. The first choice is to make the large loop (resonator 2) resonate at the frequency where the small loop (resonator 1) resonates with maximum Q-factor. Therefore, in this case the resonant frequency is determined by the parameters of the smaller resonator and the system works at a relatively high frequency. The second choice is to make the smaller loop (resonator 1) resonate at the frequency where the large loop (resonator 2) resonates with maximum Q-factor. Therefore, in this case the broadband system works at a lower frequency, which is determined by parameters of larger loop. Using different capacitors, this system can be tuned to work in two bands. Figure 4.19 shows the comparison of the choices to realize broadband systems utilizing the same size loops (r_{c1}=r_{c2}=r_{c3}=1.1 mm, r_1=9.3 mm, r_2=13 mm, r_3=32.5 mm, d=42 mm) but with different capacitors in order to operate at two different frequency bands efficiently (capacitors in higher frequency band: C_2=6.71 pF,

C_3=1.97 pF; capacitors in lower frequency band: C_2'=32.27 pF, C_3'=9.5 pF). It is shown that broader bandwidth and better performance can be achieved when the system is working at the higher frequency band, which is mainly determined by the parameters of the smaller loop (resonator 1). Therefore, the smaller loop (resonator 1) is used to design broadband systems.

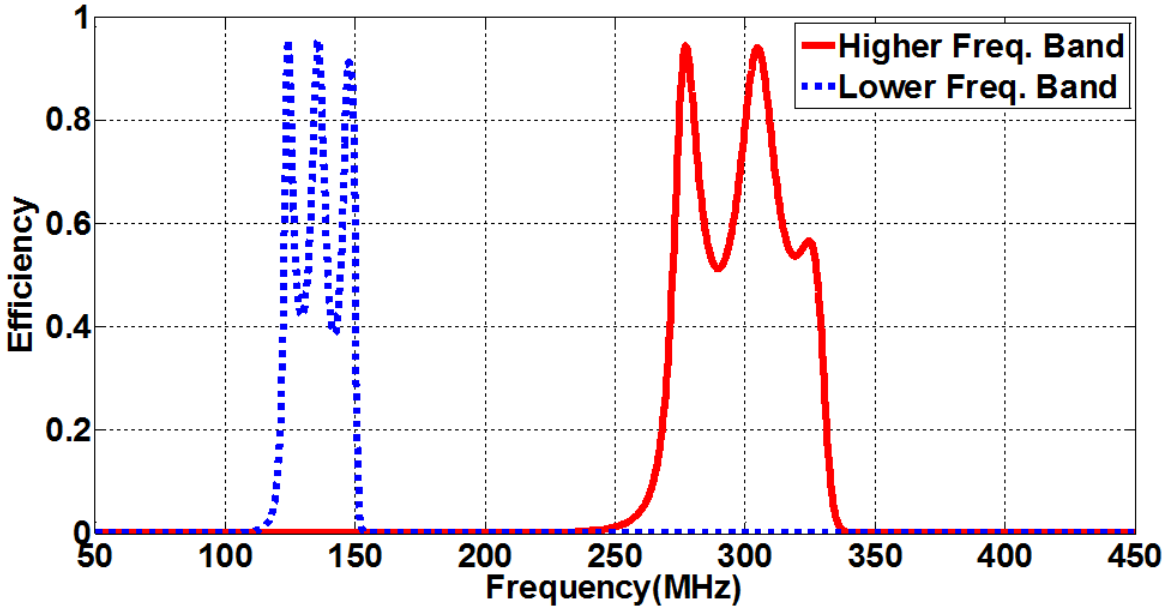

Figure 4.19. CSCMR broadband system operating in two different bands by changing the capacitors of the resonators.

4.2.2 Comparisons with Traditional SCMR Methods

Based on the previous results, a broadband CSCMR is designed and it is compared with traditional SCMR and CSCMR systems. The comparison is made in two ways: 1) the three systems are operating at the same frequency, and 2) the three systems have same outer diameters. Figure 4.20 shows the three different systems that will be compared at the same frequency. The first system is a standard SCMR system, which is narrowband. The second system is the standard CSCMR system, which is also

narrowband. The third system is the proposed novel broadband CSCMR system. The operating frequency for all the three systems is 165 MHz. All the loops of the three systems have same cross-sectional radius of loop, $r_c''= r_c'=r_c$=2.1 mm. The radius of the loop (r_2'', r_2' *or* r_2) which will resonate at 165 MHz with maximum Q-factor is calculated as 21 mm by (23). The corresponding capacitor is 14.6 pF. Based on the findings of the previous section, the broadband CSCMR's parameters are related to the radius of the middle loop (r_2). The radius of innermost loop (r_1) is chosen as r_2 /1.4=15 mm and the radius of outermost loop (r_3) is chosen as r_2×2.5=52 mm. The lumped capacitor of the outermost loop is chosen as 4.2 pF in order to make its resonant frequency equal to the one of the middle loop. Considering the optimal ratio of d/r_3 as 1.0 ~ 1.3 (which was found above), the TX and RX resonators for all three systems are placed at a distance, $d''= d'=d$=60 mm. All the designs are shown in Figure 4.20.

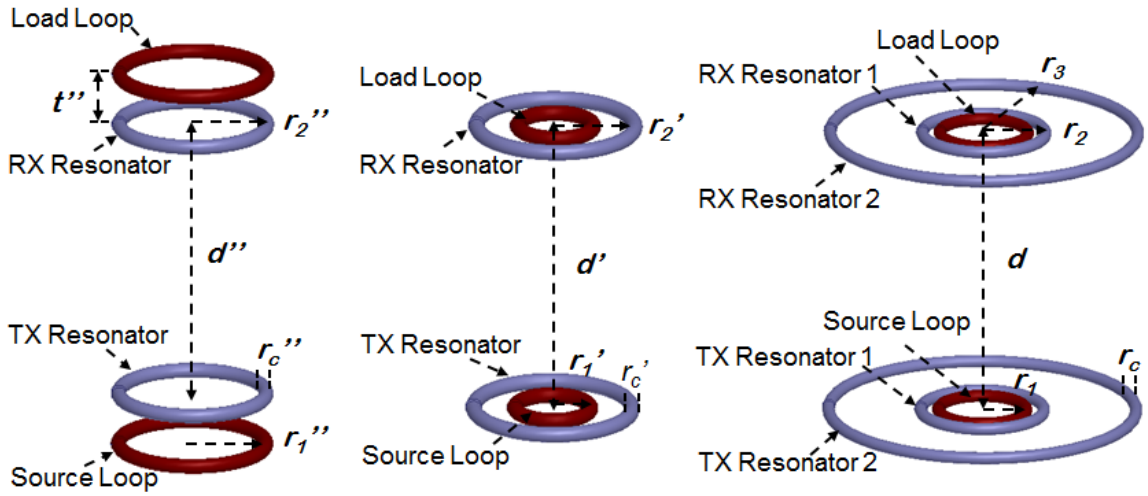

(a) (b) (c)

Figure 4.20. Models of three different SCMR systems operating at the same frequency. (a) Traditional SCMR (r_c''=2.1 mm, $r_1''= r_2''$=21 mm, t''=20 mm, d''=60 mm, C_2''=14.6 pF). (b) Standard CSCMR (r_c'=2.1 mm, r_1'=10 mm, r_2'=21 mm, d'=60 mm, C_2'=14.6 pF). (c) Broadband CSCMR (r_c=2.1 mm, r_1=15 mm, r_2=21 mm, r_3=52 mm, d=60 mm, C_2=14.6 pF, C_3=4.2 pF).

Figure 4.21 compares the simulated efficiencies of the three systems. Figure 4.21 shows that the proposed broadband CSCMR exhibits significantly larger bandwidth than the other two methods. Table 4.1 also compares the three methods and shows that the broadband CSCMR system has 7-8 times larger bandwidth than the other two traditional systems.

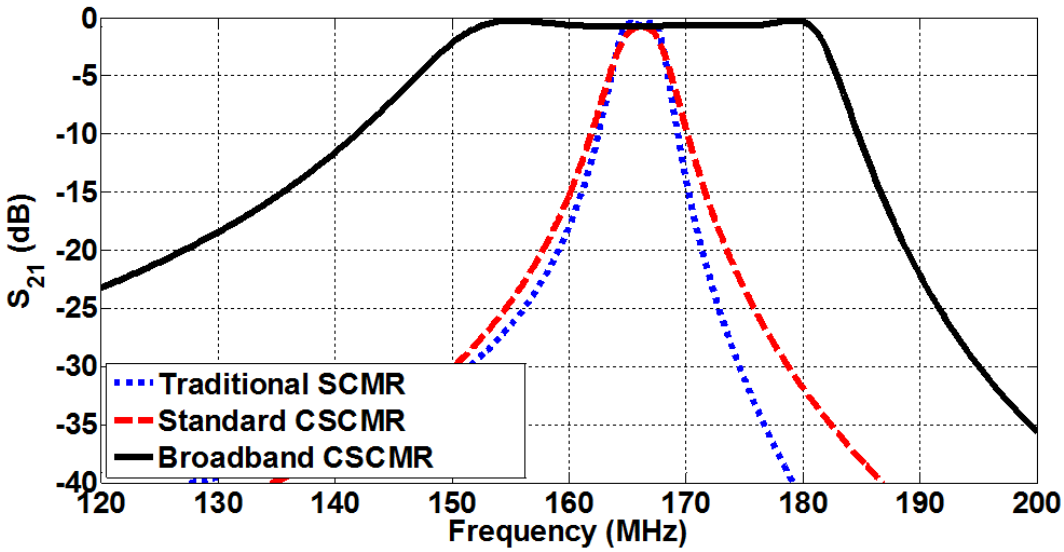

Figure 4.21. S_{21}-parameter of the three WPT systems of Figure 4.20.

Table 4.1. Comparison of the Three WPT Systems of Figure 4.20.

	Traditional SCMR	Standard CSCMR	Broadband CSCMR
3 dB BW (MHz)	4.1	4.0	33
5 dB BW (MHz)	4.9	5.3	36
10 dB BW (MHz)	6.8	8.2	43
Overall Dimension of TX or RX element (mm)	42	42	104
Thickness of TX or RX element (mm)	28.4	4.2	4.2
Distance between TX and RX (mm)	60	60	60
Efficiency at 165 MHz	86.0%	84.2%	84.2%

In order to validate the simulation results, the broadband CSCMR of Figure 4.20(c) is fabricated and measured. Actual capacitors cannot be as precise as the ones used in the analytical and simulation models (C_2=14.6 pF, C_3=4.2 pF). Therefore, capacitors with values of 14 pF and 4 pF were used in the prototypes. Therefore, the operating frequency will slightly shift to higher frequency. Figure 4.22 shows the prototype and the measurement setup.

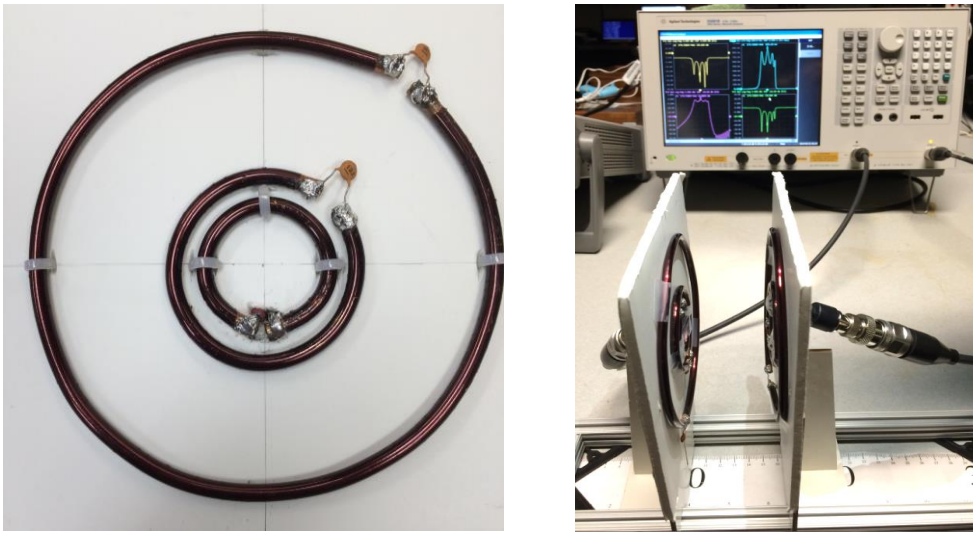

(a) (b)

Figure 4.22. Prototype of broadband CSCMR system (d=60 mm, r_1=15 mm, r_2=21 mm, r_3=52 mm, C_1=14 pF, C_2=4 pF). (a) TX or RX element. (b) Measurement system.

Figure 4.23 plots the efficiency of this system and compares analytical and simulated calculations with measurements. It can be seen that this design operates at a center frequency of 170 MHz. Also, this design exhibits a bandwidth of 38 MHz for efficiency that is at least 50%. In addition, the measurements agree well with the analytical and simulation results. The measured efficiency is lower than the simulated one. This discrepancy is mainly due to the fact that the capacitors used in this experiment have losses and are not perfect as the capacitors used in the simulation.

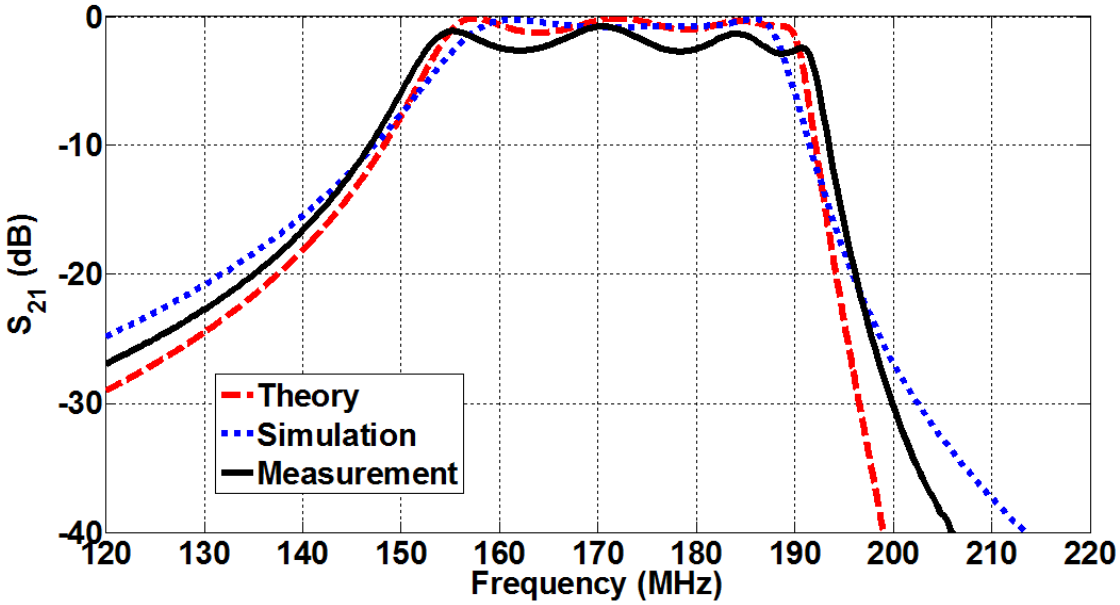

(a)

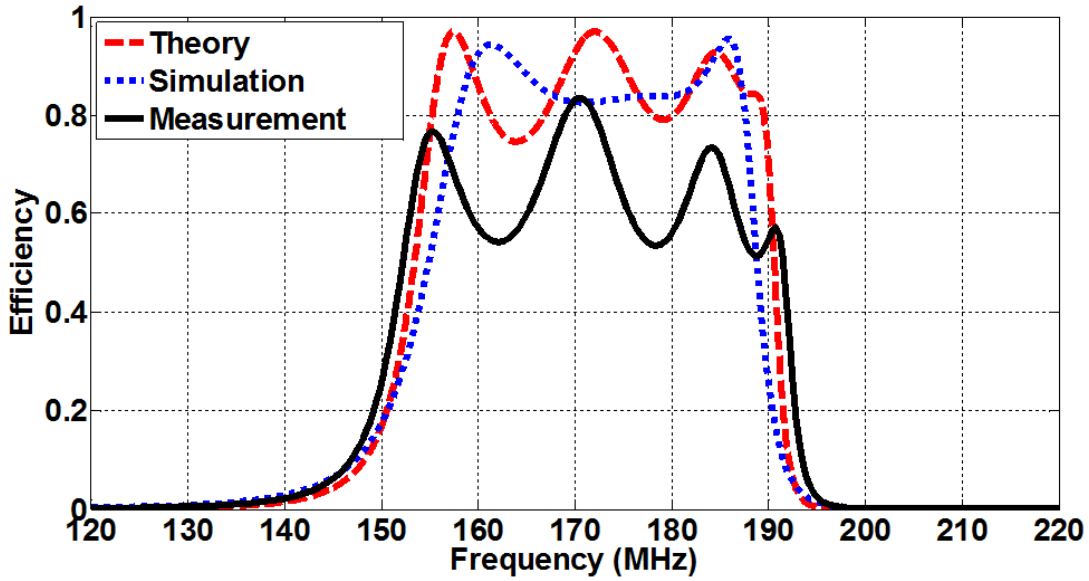

(b)

Figure 4.23. Performance of the prototyped broadband CSCMR system. (a) S_{21}-parameter. (b) Efficiency.

Next, the performance of this broadband CSCMR system is compared with the performance of the traditional SCMR and standard CSCMR systems that resonate at the same frequency. The corresponding systems are shown in Figure 4.24 and they are based

on the parameters of Figure 4.20. Figure 4.25 compares the measurements of the three systems in Figures 4.22 and 4.24. It is seen that the maximum efficiencies of traditional SCMR, standard CSCMR and broadband CSCMR are 64.85%, 53.14% and 83.45%, respectively. The 3 dB bandwidths of these three systems are 3.4 MHz, 4.5MHz and 39.2 MHz. These results clearly illustrate that the proposed broadband CSCMR exhibits significantly larger bandwidth than the other two SCMR methods.

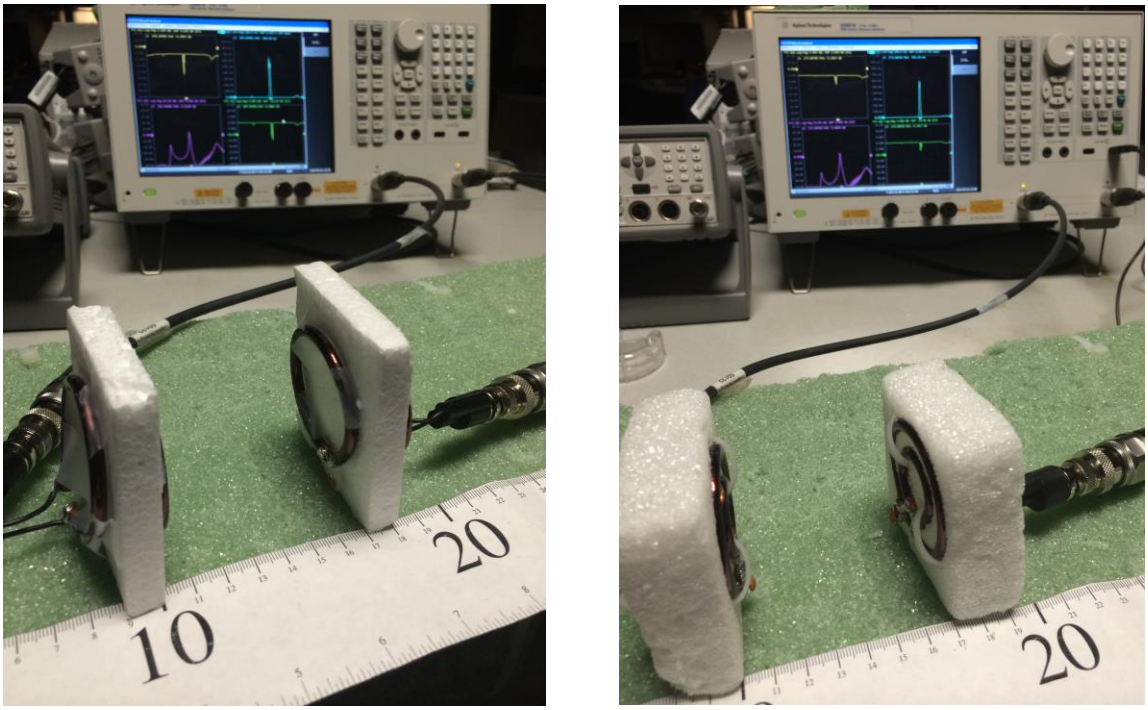

(a) (b)

Figure 4.24. Prototypes of two WPT systems: (a) Traditional SCMR. (b) Standard CSCMR.

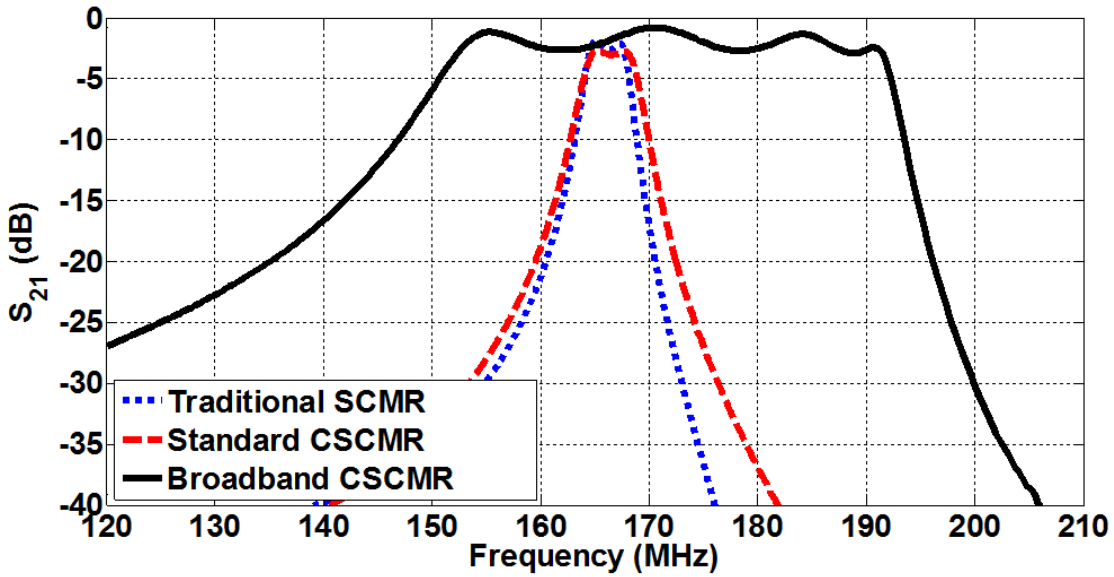

(a)

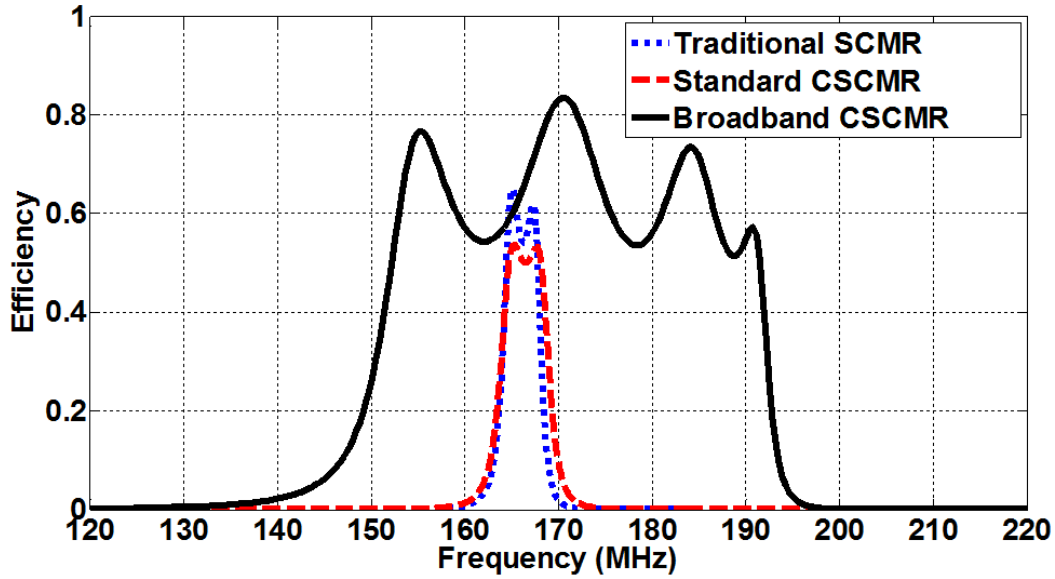

(b)

Figure 4.25. Measured performance of three WPT systems working at same frequency. (a) S_{21}-parameter. (b) Efficiency.

Also, the three methods (broadband CSCMR, SCMR and CSCMR) are compared for systems with the same outer diameters that operate at different frequencies. In order to achieve maximum efficiency for each system, the design of traditional SCMR and

standard CSCMR systems should satisfy formulas (3.5) and (3.6). Based on these formulas, the frequency where the loop with radius of 52 mm exhibits maximum *Q*-factor is 78 MHz thereby requiring a lumped capacitor of 20 pF. The other parameters are chosen based on the theoretical analysis and optimal designs discussed in section III. These three systems with same outer loops are placed at the same distance of 60 mm. All three designs are shown in Figure 4.26. Figure 4.27 shows the corresponding prototypes and measurement setups of the traditional SCMR and standard CSCMR systems based on the parameters shown in Figure 4.26.

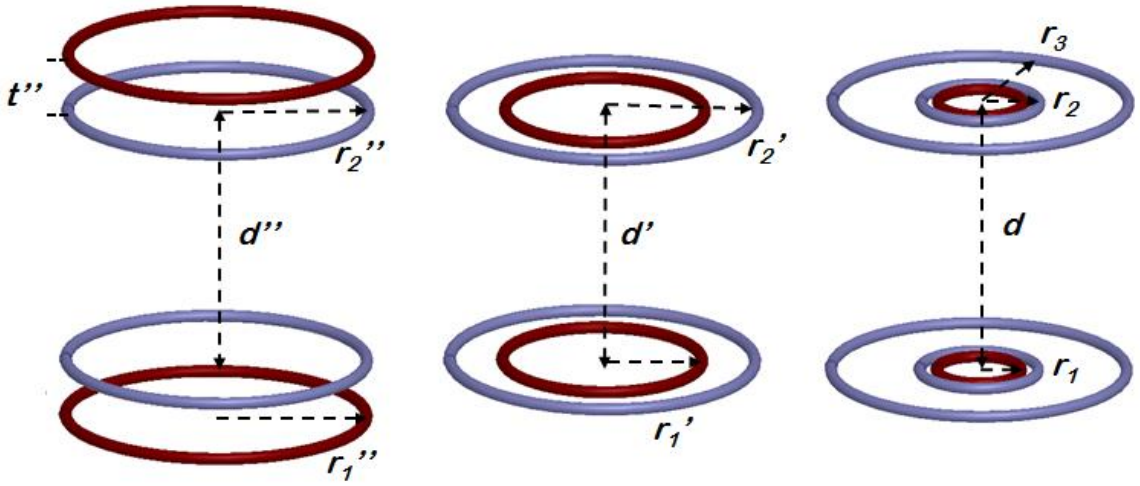

(a) (b) (c)

Figure 4.26. Models of three different SCMR systems with same outer diameters. (a) Traditional SCMR (r_1''= r_2''=52 mm, t''=20 mm, d''=60 mm, C_2''=20 pF). (b) Standard CSCMR (r_1'=34 mm, r_2'=52 mm, d'=60 mm, C_2'=20 pF). (c) Broadband CSCMR (r_1=15 mm, r_2=21 mm, r_3=52 mm, d=60 mm, C_2=14.6 pF, C_3=4.2 pF).

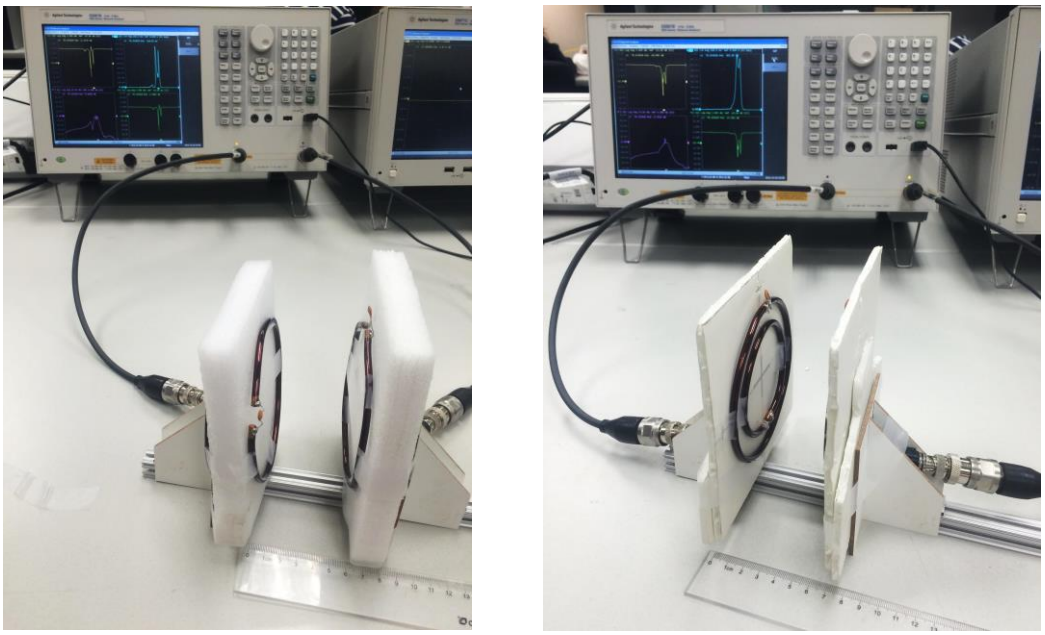

(a) (b)

Figure 4.27. Prototypes of two WPT systems with same outer diameters as the broadband CSCMR: (a) Traditional SCMR. (b) Standard CSCMR.

Since the three systems are working at different frequencies, the fractional bandwidth is used to evaluate the system bandwidth performance. The fractional bandwidth is defined as

$$FBW = \frac{2(f_H - f_L)}{f_H + f_L}. \tag{4.5}$$

The measurements of the three systems of Figures 4.22 and 4.27 are compared in Figure 4.28. Figure 4.28 shows that the 3 dB fractional bandwidths of standard SCMR, CSCMR system and proposed broadband CSCMR system are 2.56%, 12.22% and 23.06%, respectively. Therefore, the proposed broadband CSCMR system exhibits larger bandwidth than the other two SCMR methods with the same outer diameters.

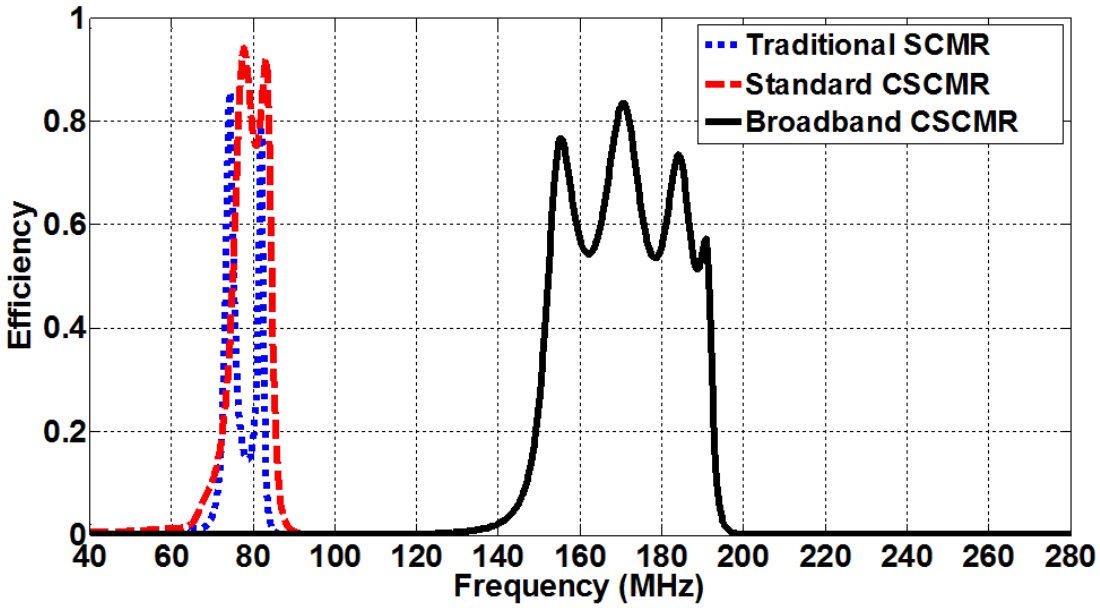

Figure 4.28. Measured efficiency of three WPT systems with same outer diameters.

4.2.3 Broadband System using Printable CSCMR

The broadband CSCMR WPT system design can also been used in the printable CSCMR system. The copper loops are printed by LPKF machine on a PCB. In this way, it is more simple and accurate to fabricate a broadband CSCMR WPT system.

As discussed in the previous sections, some design rules should be followed in order to achieve better in band performance. First, the radius of the outmost loop should be around 2.5 times of the radius of the middle loop. Also, the source/load loop which is the innermost loop needs to be as close as possible to the first resonator loop. Therefore, the parameters of the broadband are chosen as: d=40 mm, $r1$=11 mm, $r2$=14.6 mm, $r3$=38 mm, C_1=24 pF, C_2=82 pF, w=2 mm. The geometry and 3D model of a broadband CSCMR system are shown in Figure 4.29.

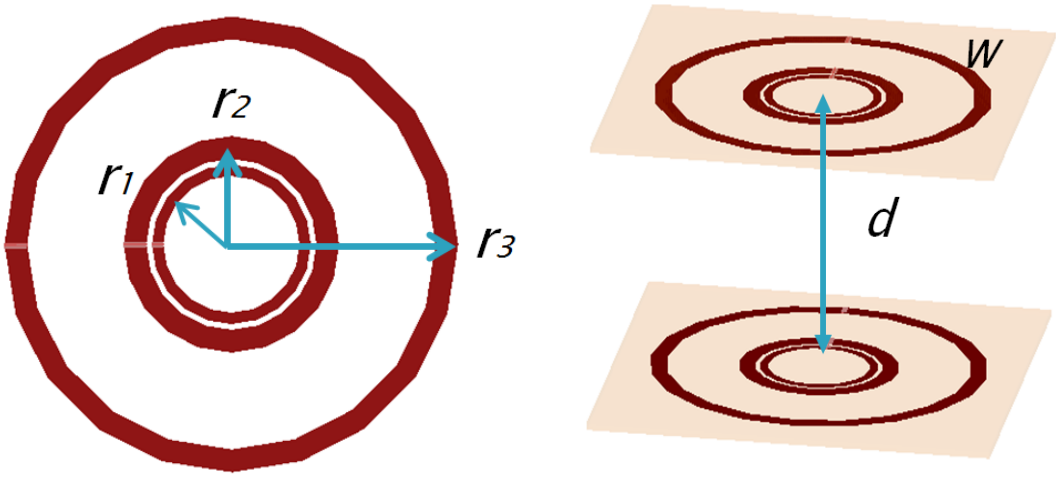

(a) (b)

Figure 4.29. A dual bands CSCMR WPT system (d=40 mm, w=2 mm, r_1=11 mm, r_2=14.6 mm, r_3=38 mm, C_1=24 pF, C_2=82 pF). (a) Geometry. (b) 3D model.

The design is validated by simulation and measurement. The measurement prototype is shown in Figure 4.30. Simulated and measurement results are compared in Figure 4.31. Both results matched and showed that more than 10 MHz 3dB bandwidth is achieved at 73 MHz.

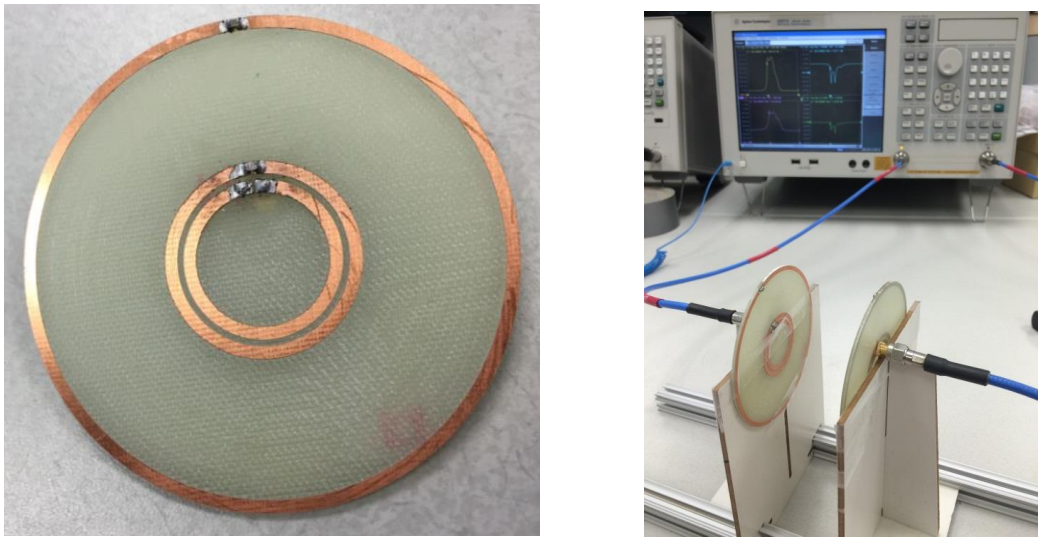

(a) (b)

Figure 4.30. Prototype of a broadband CSCMR WPT system in Figure 4.29. (a) Prototype of a TX or RX element. (b) Measurement setup.

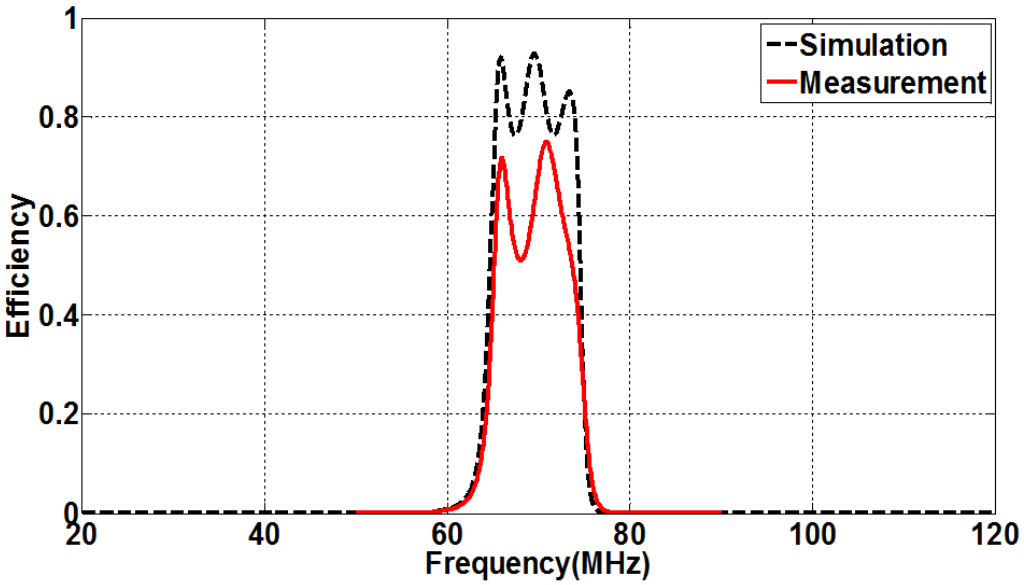

Figure 4.31. Simulated and measurement results of a broadband CSCMR WPT system in Figure 4.29.

4.3 Summary

In this section, design methods for multiband and broadband CSCMR wireless power transfer systems are proposed. Two-band, three-band and four-band CSCMR systems are designed and validated. Also, novel broadband CSCMR systems are analyzed, designed, simulated and measured. The proposed broadband CSCMR system significantly broadens the bandwidth of traditional SCMR systems. In fact, the prototyped broadband CSCMR system achieved more than 7 times larger bandwidth compared to the traditional SCMR system at the same frequency. Also, broadband system using planar CSCMR is designed and validated. Multiband and broadband wireless power transfer systems have great potential in various wireless applications. For example, the proposed WPT systems can be scaled to operate at the appropriate frequencies in the ISM band for charging mobile devices or sensors depending on the application.

CHAPTER 5

MINIATURIZATION OF SCMR SYSTEMS

In this chapter, the properties of planar Conformal SCMR (CSCMR) are initially studied. Volume reduction of CSCMR WPT systems is realized based on these properties. Additionally, novel topologies are proposed in order to miniaturize CSCMR systems. Finally, the effects of high permittivity or permeability substrates are studied. All these methods successfully tuned the operating frequency to lower frequencies with excellent efficiencies, thereby reducing the size of CSCMR systems.

5.1 Miniaturization Methods

Wireless power transfer technologies for communication and recharging devices have recently attracted increased interest based on current society needs in various areas such as, sensors, Integrated Circuit chips (ICs), biomedical implants, and wireless communications [76-78]. The miniaturization of SCMR systems will significantly enhance various technologies by providing small, highly efficient wireless power systems that can support safe and flexible operation of different applications. In the following sections, we will discuss several methods for miniaturized SCMR WPT system.

5.2 Printable CSCMR

Conventional SCMR requires certain distance between the source and the TX resonator as well as between the load and the RX resonator. Depending on the dimension of each element, the distance can be relatively large (around half of the largest dimension of the resonators). Therefore, the traditional three-dimensional structures of SCMR

systems occupy significant volume and cannot be easily printed on substrates and incorporated in modern communications systems and implantable medical devices.

The Conformal SCMR (CSCMR) was proposed recently to address this problem [69] and used copper loops to realize CSCMR systems. However, the cross-sectional thickness of these loops still limits the use of CSCMR structures in many practical applications. A printable compact SCMR structure is presented and realized on a PCB, as shown in Figure 5.1. Results of simulations and measurements show this approach can result in a realizable unit cell size down to $\lambda_0/66$. Also, the printable CSCMR element has some unique properties which can help to further shrink the volume of CSCMR systems.

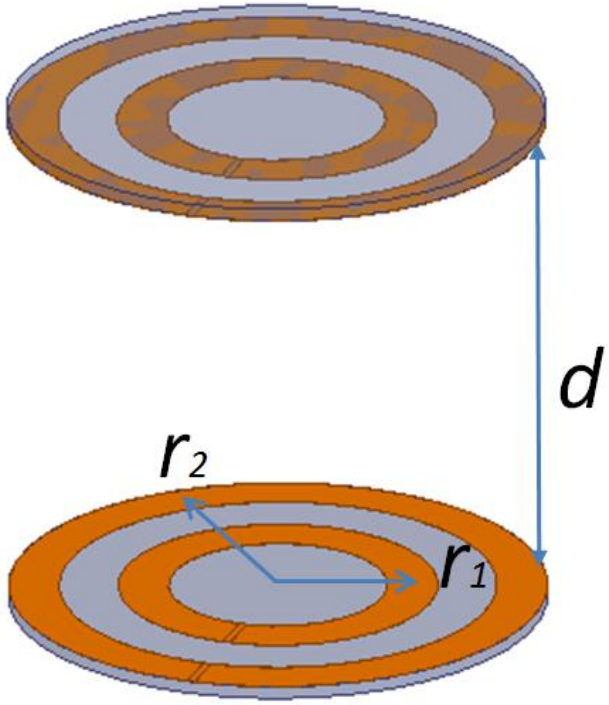

Figure 5.1. A typical printable CSCMR WPT system (r_1=13 mm, r_2=29 mm, d=60 mm).

5.2.1 Printable CSCMR Properties

In a traditional SCMR system, the Q-factor of one resonator loop exhibits one maximum value in a certain frequency, f_{max}. If the operating frequency is away from that frequency, f_{max}, Q-factor will drop quickly. Therefore, efficiency is low except when the operating frequency is exactly equal to the frequency, f_{max}, where Q-factor is maximum. However, the Q-factor in a planar CSCMR system maintains high value in a wide frequency range. Therefore, the system can work in a relatively wide frequency range while maintaining high efficiency using different capacitors. Figure 5.2 shows the Q-factor of the resonator illustrated in Figure 5.1. It shows that the Q-factors are above 1000 from 33 MHz to 144MHz. The Q-factor is maximum around 80 MHz.

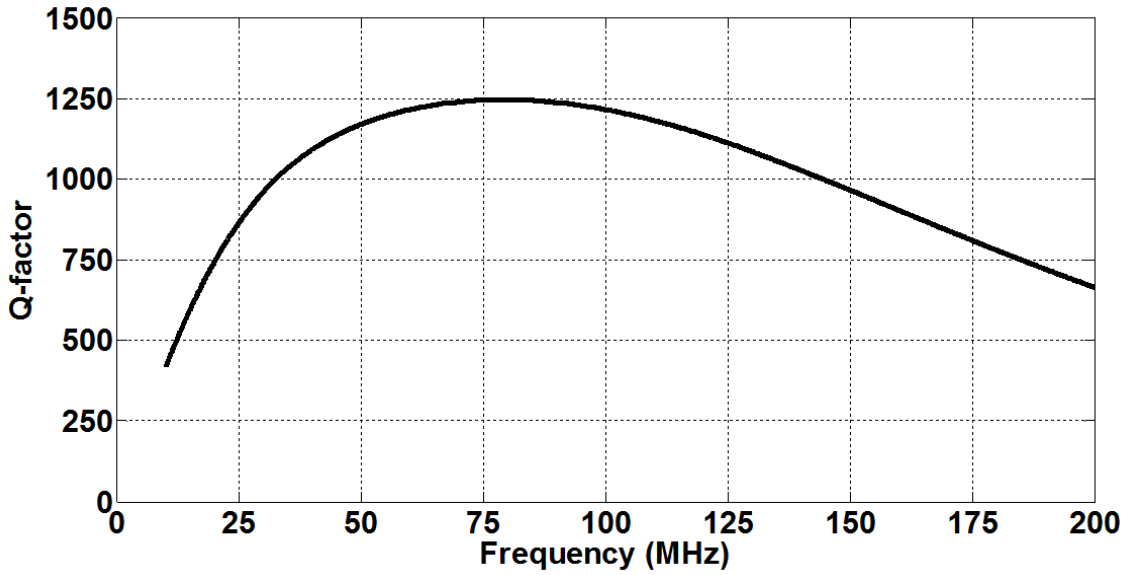

Figure 5.2. The Q-factor of the resonator illustrated in Figure 5.1.

5.2.2 Printable CSCMR using Large Capacitors

The Q-factor of one resonator loop in a planar CSCMR system maintains high value in a wide frequency range. Therefore, a CSCMR system can be tuned to operate at

lower frequency (e.g., 48 MHz) using larger capacitor (e.g., 100 pF) while maintaining high efficiency. The simulation result of a typical CSCMR system in Figure 5.1 using ANSYS HFSS is shown in Figure 5.3. Efficiencies of various systems with different capacitors working from 48 MHz to 110 MHz are all above 80%. Therefore, a CSCMR system can be tuned to operate at lower frequency (e.g., 48 MHz) using larger capacitor (e.g., 100 pF) while maintaining high efficiency.

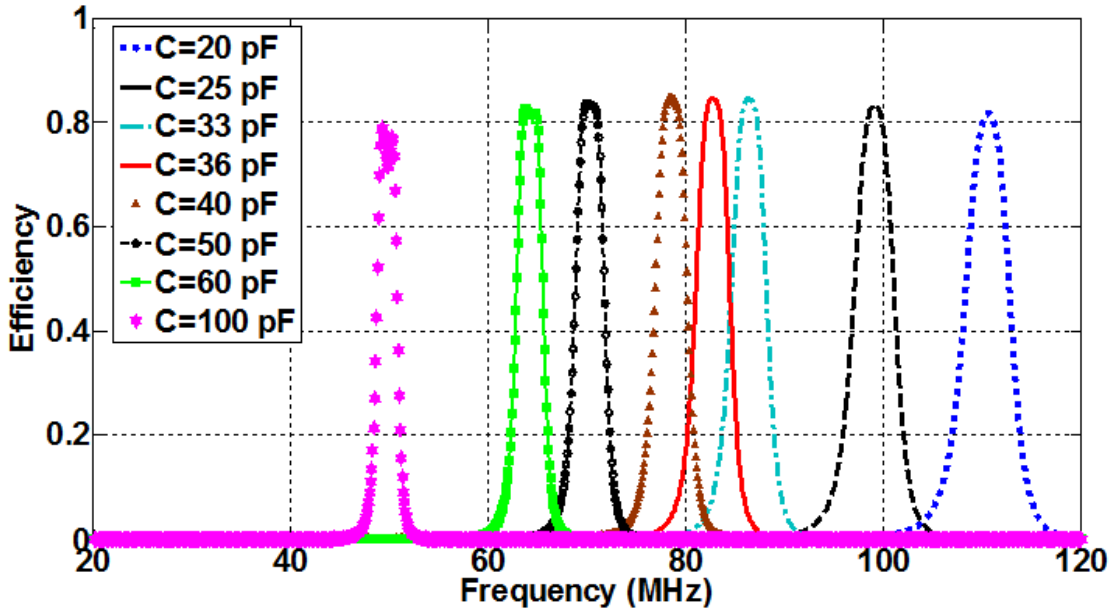

Figure 5.3. Simulated efficiency of printable CSCMR system in Figure 5.1 regarding to different capacitors.

To validate the simulated results, the printable CSCMR system in Figure 5.1 is prototyped and measured, as shown in Figure 5.4. Three different capacitors (33 pF, 47 pF, 100 pF) are used and the efficiencies of the printable CSCMR systems are tested respectively. Table 5.1 lists the tested efficiencies of the three different systems. It shows that when a larger capacitor is used (e.g., 100 pF), the operating frequency will shift to lower frequency (e.g., 48 MHz) while 66% efficiency still will be achieved. Therefore,

the miniaturization of SCMR system can be fulfilled by using larger capacitors in printable CSCMR systems.

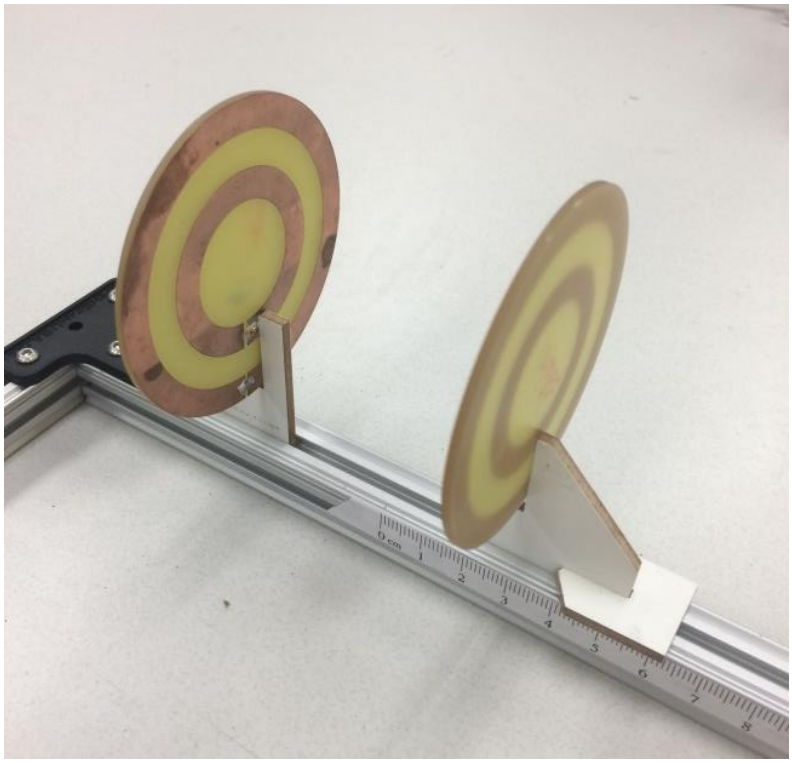

Figure 5.4. Measurement prototype of the printable CSCMR system in Figure 5.1.

Table 5.1. Measurement of the Three WPT Systems with Different Capacitors.

Capacitors	Operating frequency	Maximum Efficiency
33 pF	84 MHz	73 %
47 pF	71 MHz	62%
100 pF	48 MHz	66%

5.3 Topology Optimization

Other methods for miniaturizing SCMR system are also studied here. Multilayered CSCMR methods that stack multiple resonators on multilayer PCB boards were reported in [79]. In such systems, the operating frequency can significantly successfully shift to lower operating frequencies. Also, using different novel topologies of the copper trace can realize miniaturization, because self-inductance or capacitance will increase [78].

The formula of resonant frequency is related to the inductance and capacitance. Therefore, increase the self-inductance of the resonator will decrease the operating frequency. The formula of the inductance of a flat or ribbon wire or a track on a PCB can be calculated using [79]

$$L = 2.0\times10^{-3}\times\ell\left[\ln\left(\frac{2.01}{w+t}\right)+0.5+0.2235\left(\frac{w+t}{l}\right)\right]\mu H \qquad (5.1)$$

where ℓ, w, and t are the length, width, and the thickness of the flat or ribbon wire in cm, respectively. Therefore, increasing the length or decreasing the width of the copper trace will make the self-inductance larger.

5.3.1 Meandered Topology

A meandered topology is used to increase the copper trace, thereby increasing the self-inductance, see Figure 5.5. Simulation results of a planar CSCMR system for system of Figure 5.5 with different lumped capacitances are shown in Figure 5.6. It is shown that the operating frequency shifts from 83 MHz to 33 MHz with 67.8% of efficiency when using 240 pF capacitor. Even though the operating frequency can be lowered for the

standard CSCMR system of Figure 5.1 using larger capacitance, its efficiency at the same frequency of 33 MHz is only 46% compared to 67.8% of the meandered system.

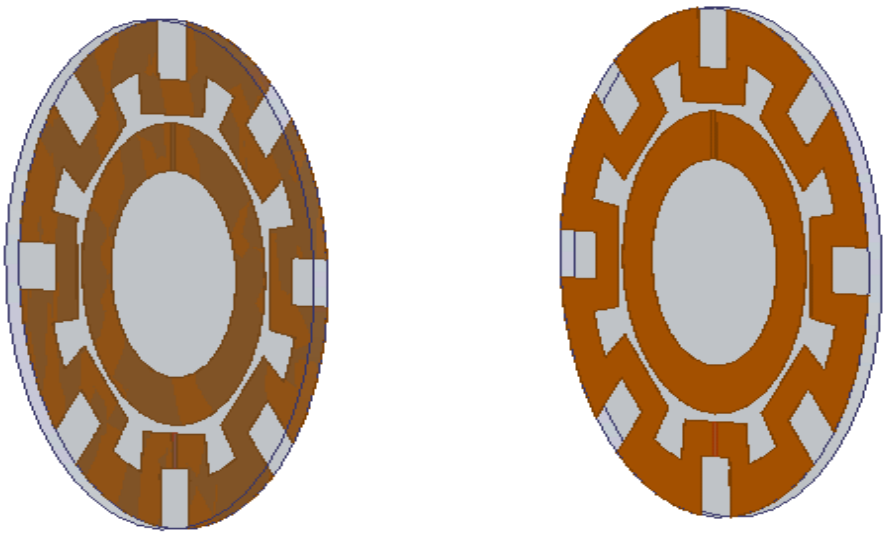

Figure 5.5. A CSCMR WPT system with meandered topology.

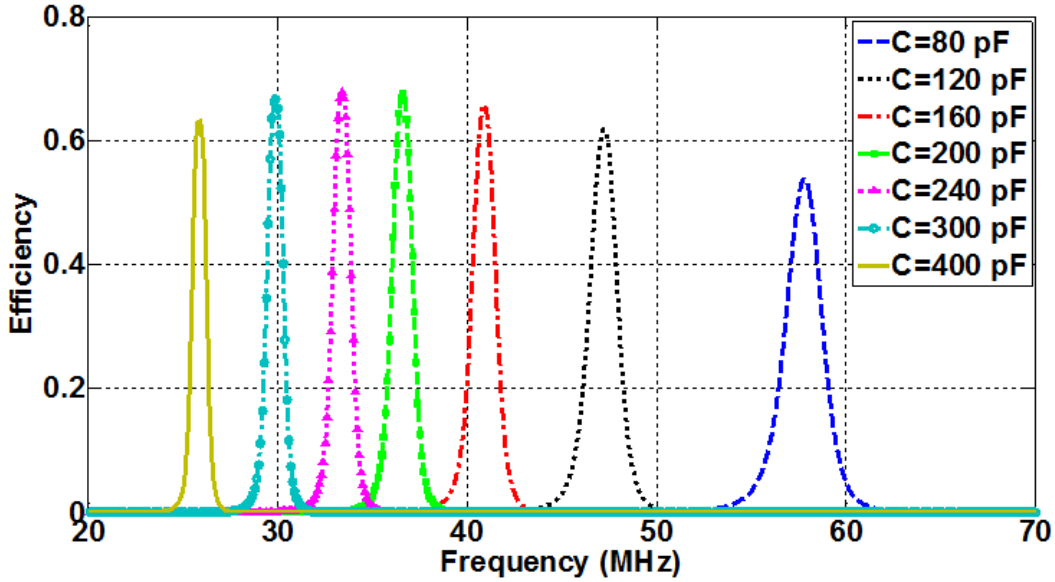

Figure 5.6. Simulated efficiency of CSCMR system of Figure 5.5 for different capacitors.

5.3.2 SRRs Topology

Increase the capacitance of the resonator will also decrease the operating frequency. The capacitance of the resonators in the SCMR systems can be realized with self-capacitor or lumped capacitor. Previous work on SCMR has used loops, coils or lumped circuits to realize the resonators. The required lumped capacitance should be calculated based on the resonant frequency. However, limited research has been done on other types of resonator structures, such as Split Ring Resonators (SRRs). The geometry of SRR is shown in Figure 5.7. This SRR structure has both inductance and capacitance thereby forming a tank resonator. The resonant frequency of the SRR element can change by varying its capacitance, which depends on the spacing, length and area of capacitive gap.

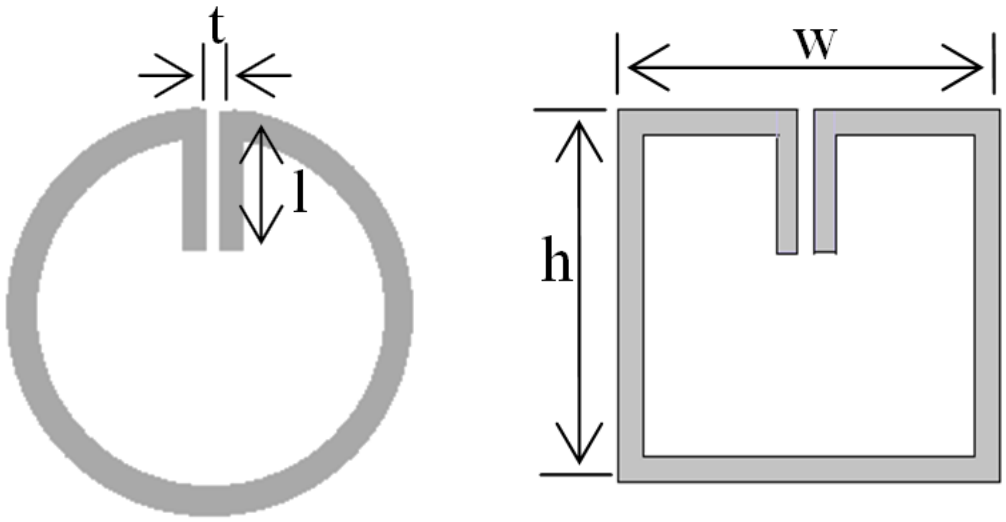

(a) (b)

Figure 5.7. The geometry of SRR structure (a) traditional circular SRR (b) square SRR.

An SCMR design with SRRs operating at 85MHz is developed (Figure 5.8). The gap is tuned using t=0.8mm and l=110mm. Higher efficiency was achieved by reducing the size of the source loop or optimizing the distance between the source loop and the SRR (l_1). Finally, an excellent power transfer efficiency (90%) is achieved at a distance of l_2=200mm. Compared with the previous research work in [80], which uses lumped capacitors (efficiency is about 64%), or system of only inductively coupled source and load loops, this design works at the same operating frequency and same distance l_2, but achieves a much higher efficiency, as shown in Figure 5.9.

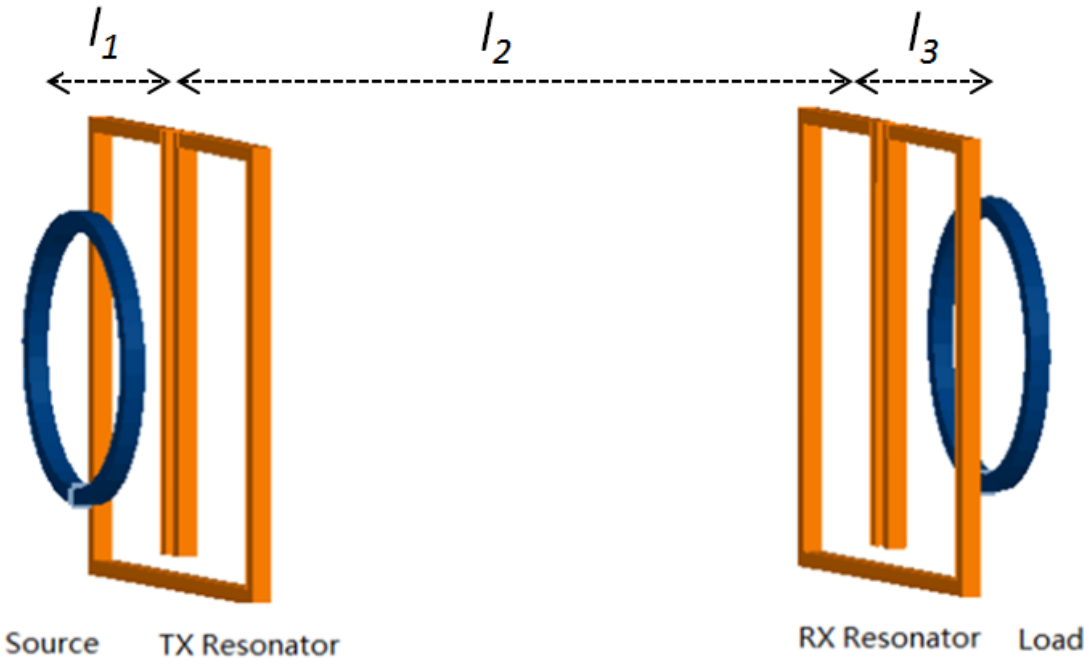

Figure 5.8. SCMR wireless power transfer system based on SRRs (l_1=l_3=20 mm, l_2=200 mm, t=0.8 mm, l=110 mm, w=125 mm, h=118 mm).

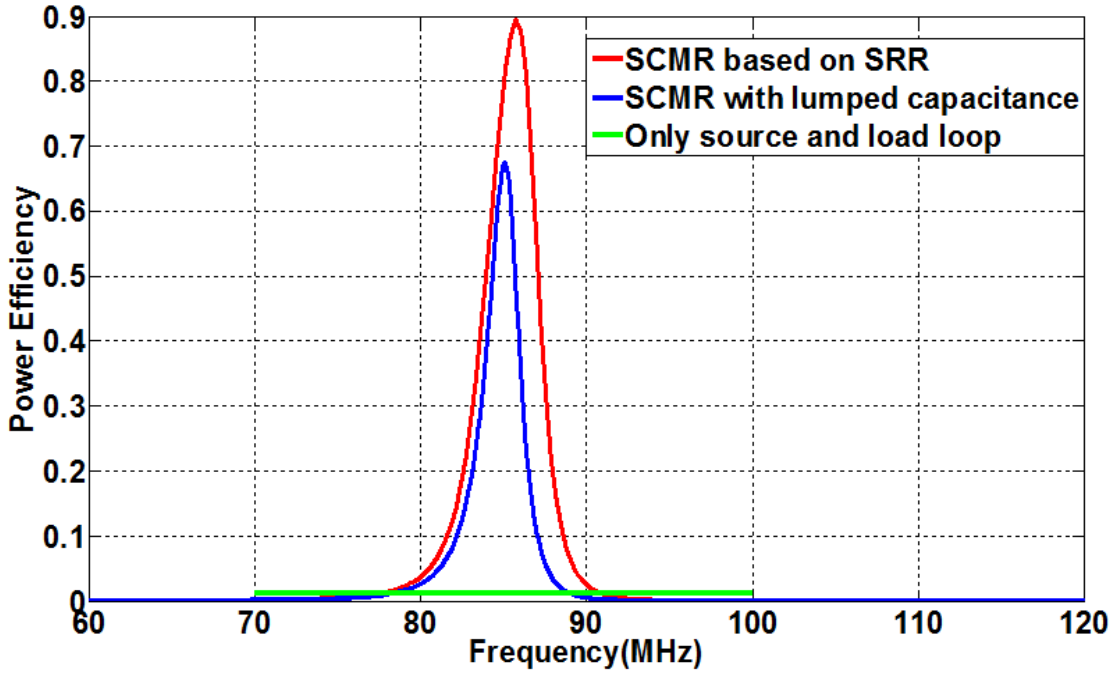

Figure 5.9. Comparison of the efficiency of inductive coupling with SCMR system based

Also in SRRs, their inductance and capacitance is relatively separated, therefore it is easier to tune their operating frequency. The inductance of SRR elements depends on their length, which can be decreased to lower their resonant frequency. However, this will reduce the inductive coupling between the source loop and the TX loop which in turn will reduce the efficiency of the SCMR system. Therefore, reduction of the resonant frequency should be done by adjusting the capacitor gap, which has less effect on the wireless powering efficiency. By increasing the length of capacitor gap (l), decreasing the distance between the gap (t), or increasing the thickness of an SRR, the operating frequency of the SCMR system decreases substantially. Figure 5.10 shows our results regarding these dimension changes. It illustrated that the operating frequency can be tuned by changing the SRRs parameters, thereby miniaturization can be realized.

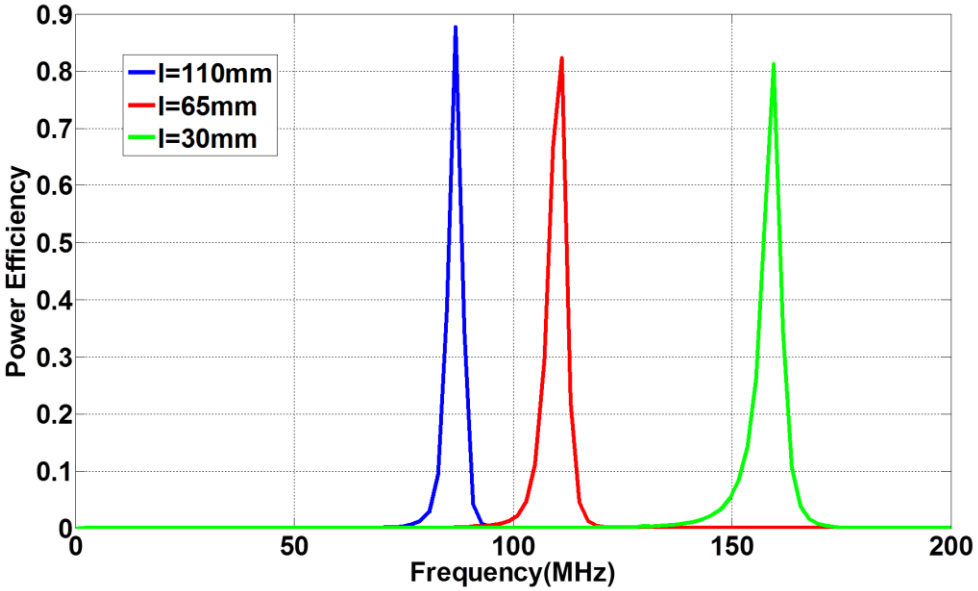
l=110mm
l=65mm
l=30mm
Power Efficiency
Frequency(MHz)
0
0.1
0.2
0.3
0.4
0.5
0.6
0.7
0.8
0.9
0
50
100
150
200

(a)

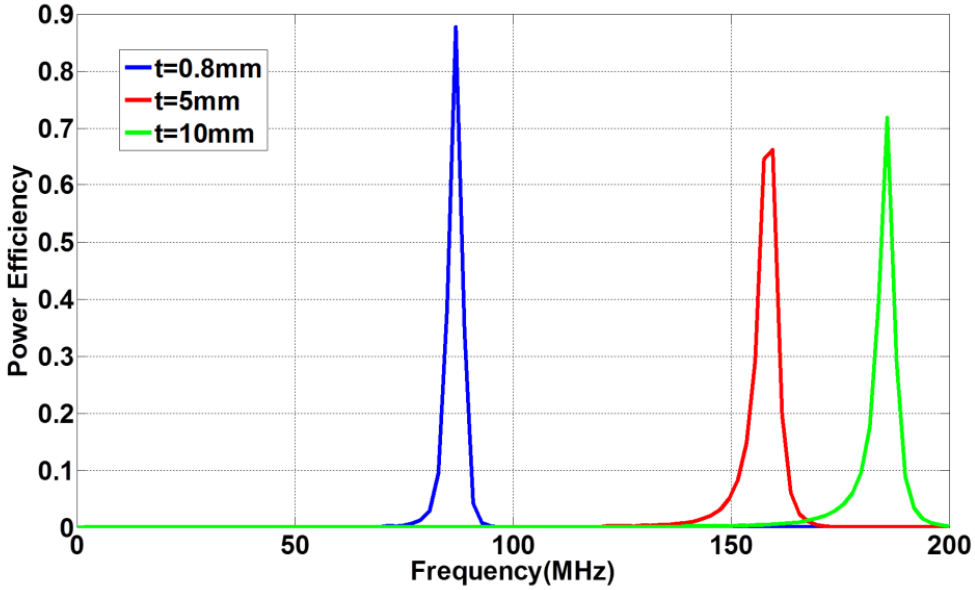
t=0.8mm
t=5mm
t=10mm
Power Efficiency
Frequency(MHz)
0
0.1
0.2
0.3
0.4
0.5
0.6
0.7
0.8
0.9
0
50
100
150
200

(b)

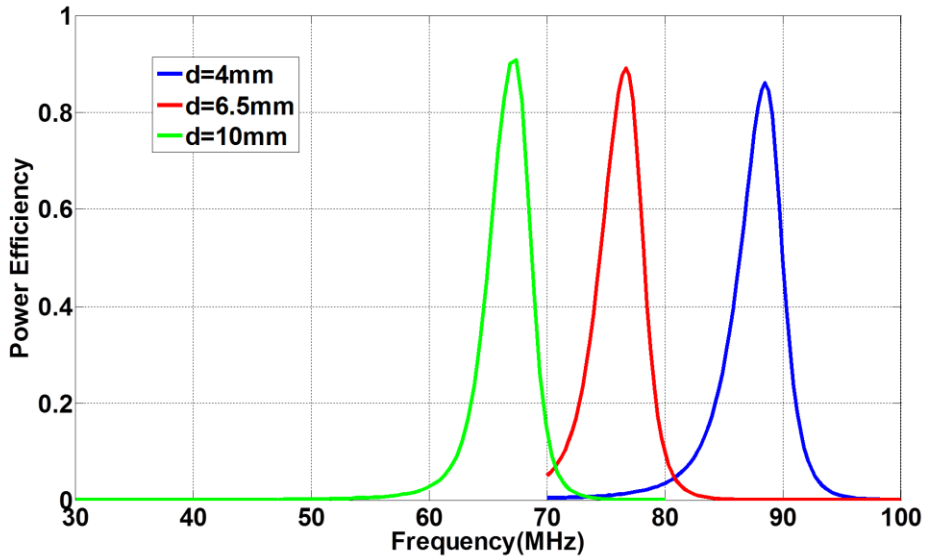

(c)

Figure 5.10. Simulated results regarding dimension changes (a) Length of gap changes. (b) Distance of gap changes. (c) Thickness of gap changes.

5.3.3 Spirals Topology

Instead of using lumped capacitors, a new CSCMR system is examined that uses a pair of identical self-resonant spirals. Resonators based on spiral structures include increased inductance but decreased capacitance. Such a printable CSCMR system will simplify the fabrication process of such systems but will not lower the operating frequency.

The resonator topology is shown in Figure 5.11(a). The spacing between each turn of the spiral structure provides the required capacitance and the copper strip provides the distributed inductance [81]. Therefore, by adjusting the width and thickness of the strip (w, t), the distance between the turns (s), and the radius of the first turn (r_1), the spiral resonator can operate at the desired frequency, where its Q factor is maximum. Also, tuning the radius of the source or the load (r_0) can also affect the system performance.

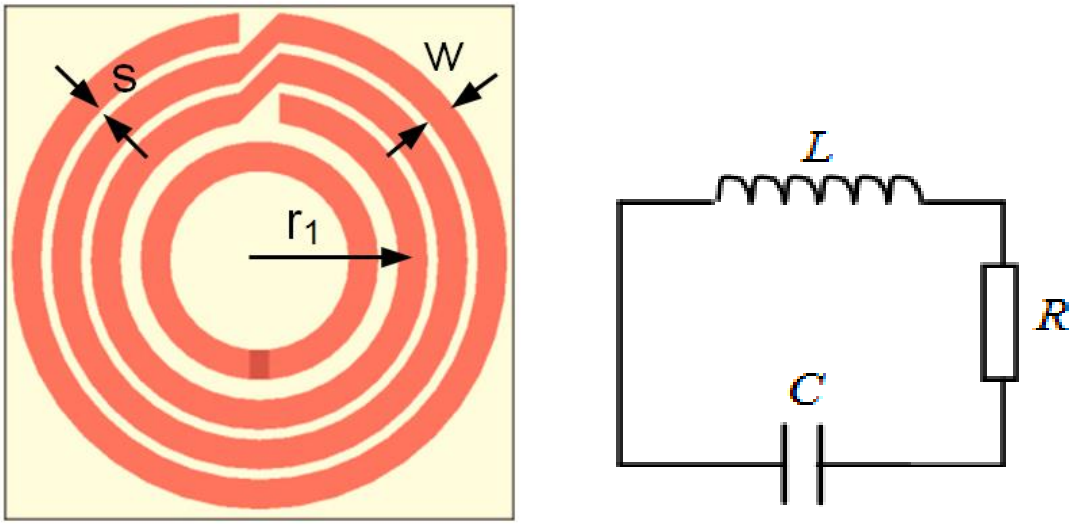

(a) (b)

Figure 5.11. Self-resonators. (a) Sketch of a three-turn spiral resonator. (b) Equivalent circuit of the spiral resonator.

The simulation model of our design is shown in Figure 5.12. The spiral TX and RX resonators are surrounding the source and load circular rings, respectively. The radius of the source and load ring is r_0=10.5 mm and the radius of the first turn of the spiral is r_1=15.5 mm. The width of the strip is w=3mm and the distance between the turns is s=1 mm. The TX element and RX element are placed at a distance of 40 mm. The design was also built and measured, as shown in Figure 5.13. The simulated and measured results of the printable CSCMR systems are compared in Figure 5.14. Apart from a slight shift in the frequency, the measured power transfer efficiency matches very well the simulation results. The WPT efficiency is approximately 48%.

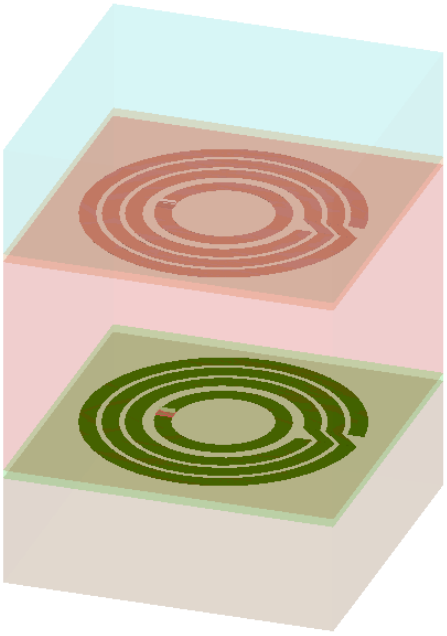

Figure 5.12. Simulation model of printable CSCMR system with self-resonant spirals.

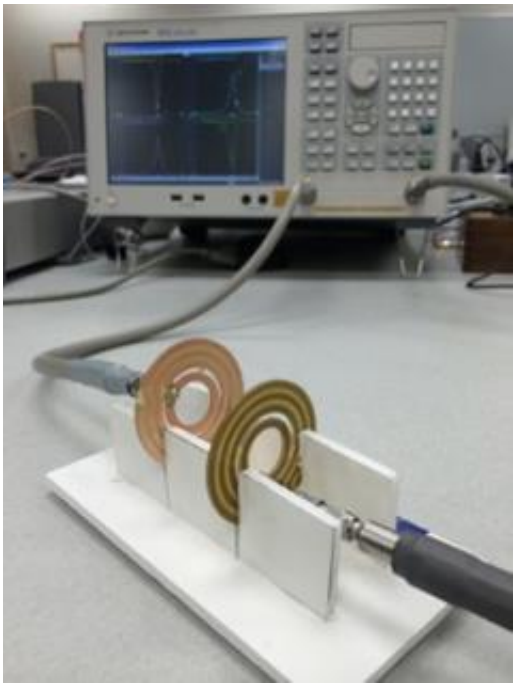

Figure 5.13. Measurement setup of a printable CSCMR system with self-resonant spirals.

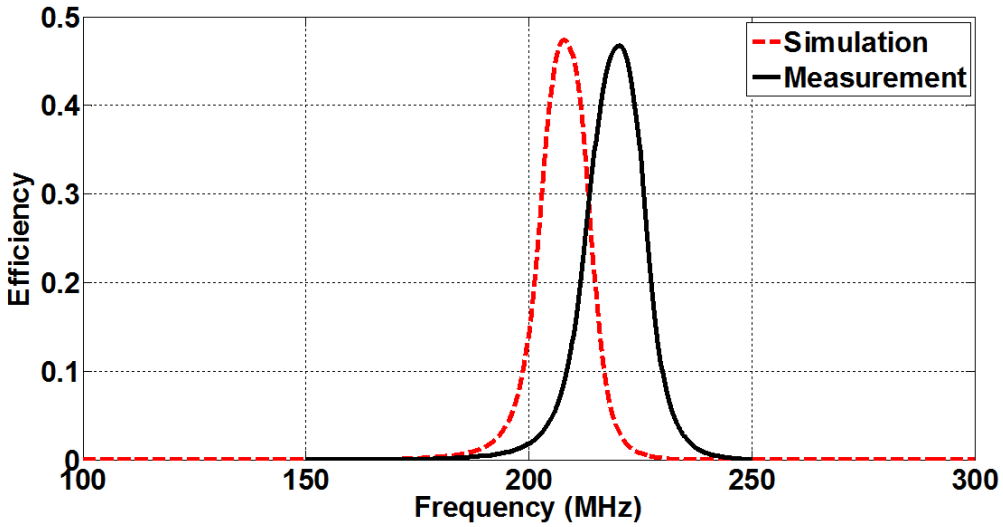

Figure 5.14. Comparison of measured and simulated results of printable CSCMR with self-resonant spirals.

Since the self-capacitance in the spiral is not large enough, a lumped capacitor is connected with the spiral trace in the same system of Figure 5.13 in order to shift the operating frequency to a lower frequency. A 68 pF capacitor is loaded between the spiral trace, see the prototype in Figure 5.15 (a). The measurement setup is shown in Figure 5.15 (b). The measured result is compared with the result of previous system, as shown in Figure 5.16. The operating frequency is shifted from 220 MHz to 28 MHz. Because the capacitors used in Figure 5.15 have loss and the long pin plays effect on the performance, the efficiency of this system is not desirable, only 48%.

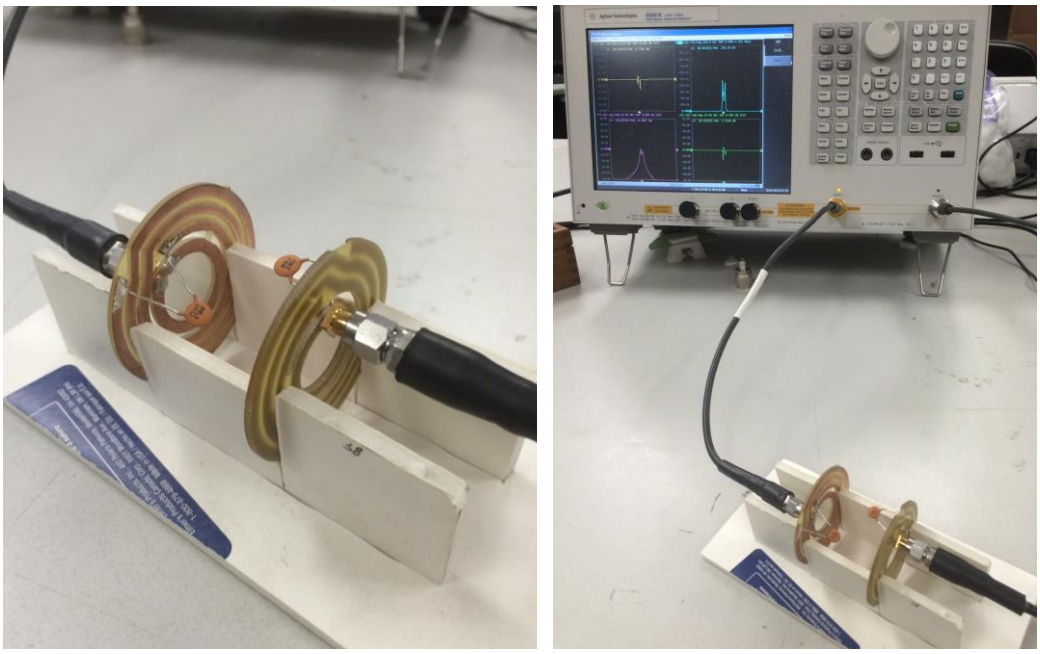

(a) (b)

Figure 5.15. A printable CSCMR system in Figure 5.13 with lumped capacitor. (a) Prototype. (b) Measurement setup.

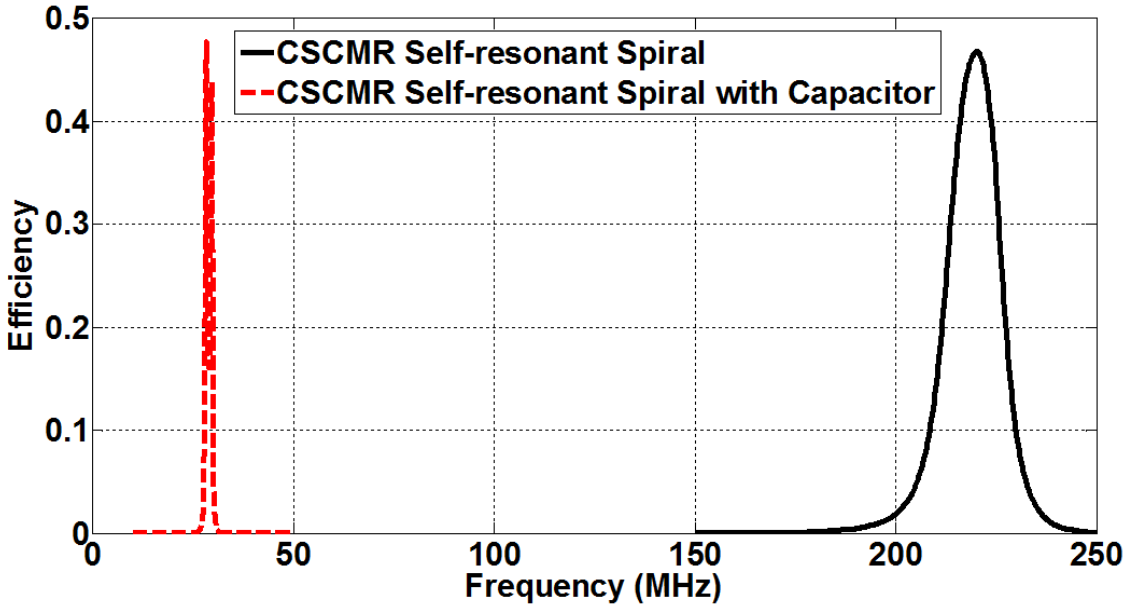

Figure 5.16. Comparison of measured results of printable CSCMR System in Figure 5.13 and Figure 5.15.

5.3.4 3-D Structure

Previous novel topologies for miniaturized CSCMR system are all based on two dimensional (2-D) planar. In this section, we proposed the 3-D structure which includes the distributed capacitance and inductance in 3-D configuration. In this way, large inductance or capacitance can be achieved and no lumped components are needed. The equivalent circuit of a typical 3-D resonator can be described as in Figure 5.17. The whole inductance will increase to the sum of inductance in the two layers, L_s+L_p. Large parallel-plate capacitance, L_p, will also be added.

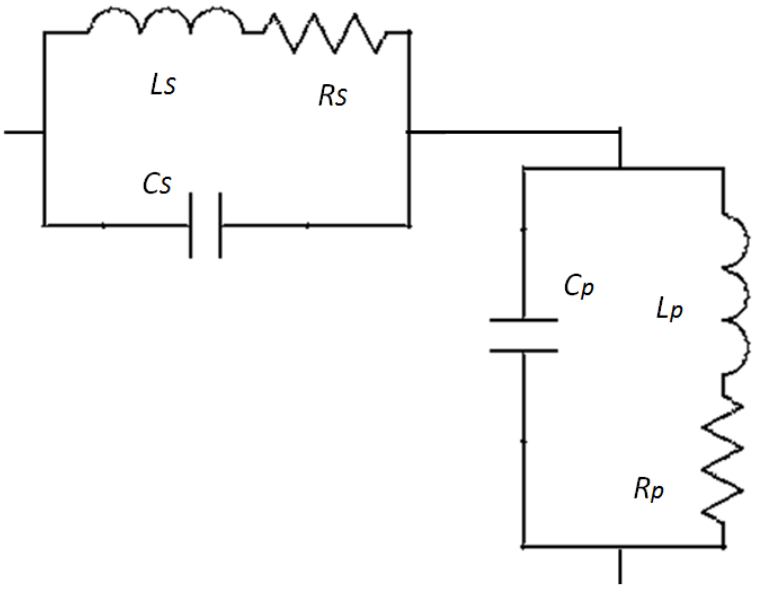

Figure 5.17. Equivalent circuit of LC resonator in 3-D CSCMR system.

Based on the equivalent circuit, a simulated model of a 3-D CSCMR system is built in Figure 5.18. Compared to the conventional CSCMR system, this 3-D CSCMR system does not need lumped capacitance and the operating frequency shifts to lower frequency. In order to compare the performance to the conventional printable CSCMR

system in Figure 5.1, the parameters of the 3-D CSCMR are chosen the same values as: : r_1=16 mm, r_2=29 mm, w=6 mm. We use the substrate with same properties for the two systems: permittivity, ε=10.2, and thickness, h=1.5 mm.

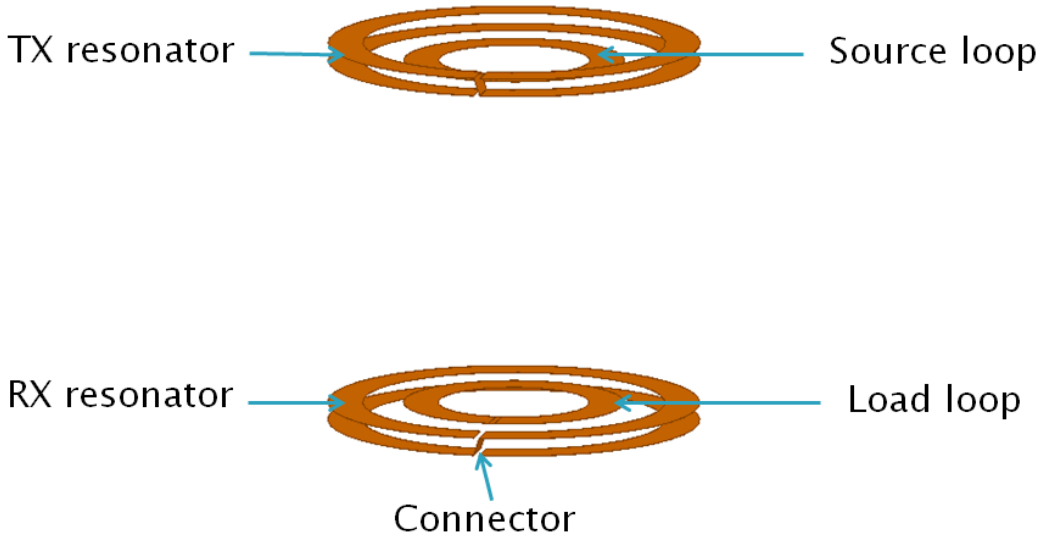

Figure 5.18. Simulated model of a 3-D CSCMR system.

The simulated compared results of one conventional printable CSCMR and two 3-D CSCMR systems with two different thicknesses are listed in Table 5.2. It shows that operating frequency shifts from 86 MHz to 60.1 MHz. If the thickness of the substrate decreases from 1.5 mm to 1.0 mm, the operating frequency will further shift from 60.1 MHz to 48.9 MHz. Therefore, 3-D CSCMR is another method to lower the operating frequency without lumped capacitor. Compared to other methods, 3-D CSCMR could lower the operating frequency further with the same size, although efficiency is sacrificed a little because of the increased copper resistance.

Table 5.2. Comparison of Different Systems.

Different systems	Lumped capacitors (pF)	Working frequency (MHz)	Efficiency (%)
Printable CSCMR	33	85.9	83.25
3-D CSCMR with 1.5 mm thickness	NA	60.1	69.88
3-D CSCMR with 1.0 mm thickness	NA	48.9	64.76

Another example to realize the 3-D CSCMR is based on the spiral topology. The CSCMR system with spiral topology has discussed in Section 5.3.3. Although the simulated model in Figure 5.12 simplifies the fabrication process, the operating frequency is too high in the mid-range application. Therefore, we proposed the 3-D CSCMR system based on multilayered spiral resonators.

A 3-D CSCMR system based on two-layered spiral resonators is shown in Figure 5.19 (a). The spiral resonators on the first layer and the second layer are placed in two opposite directions: one is in 0 degrees, and the other is rotated by 180 degrees. In this way, the operating frequency will shift to lower frequencies efficiently. Also, if we build three spirals layers in opposite directions: one is in 0 degrees, one is rotated by 180 degrees, and the other one is in 0 degrees again, as shown in Figure 5.19 (b). The operating frequency will shift to lower frequencies further.

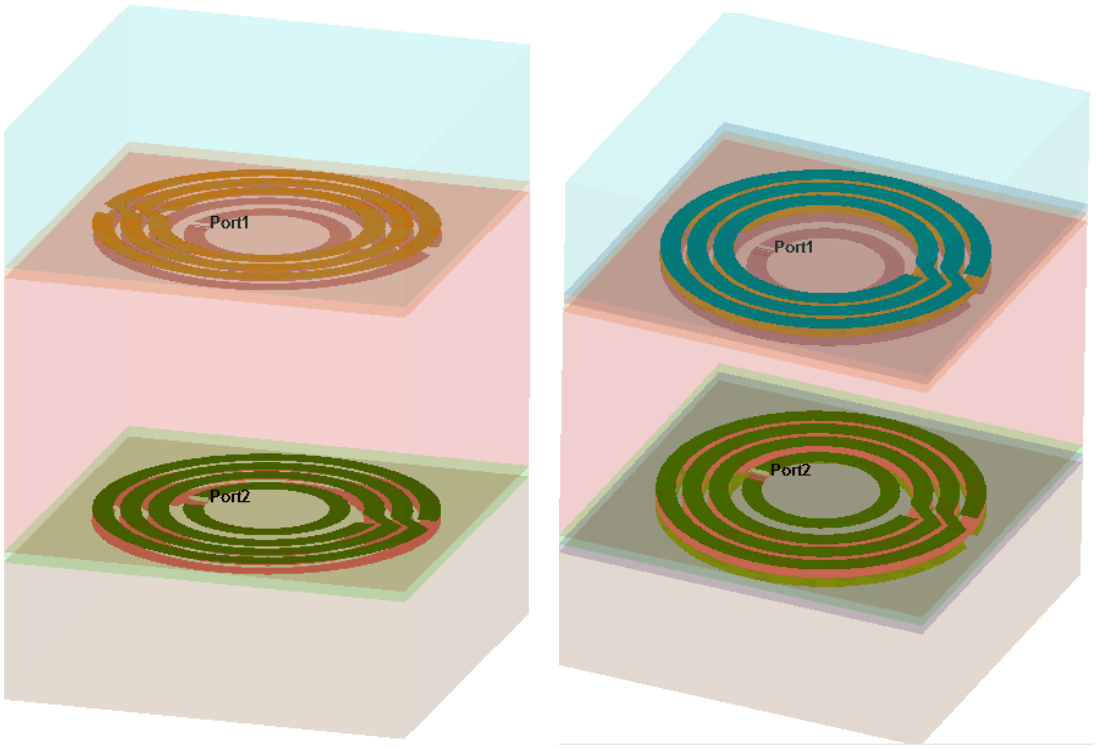

(a) (b)

Figure 5.19. A 3-D CSCMR system based on multilayered self-resonant spirals. (a) Two layers. (b) Three layers.

Figure 5.20 shows the compared results of the proposed system and the system discussed in Figure 5.12. It clearly shows that the working frequency of the 3-D CSCMR system based on two-layered and three-layered self-resonant spirals shifts from 210 MHz to 162 MHz and 127 MHz, respectively.

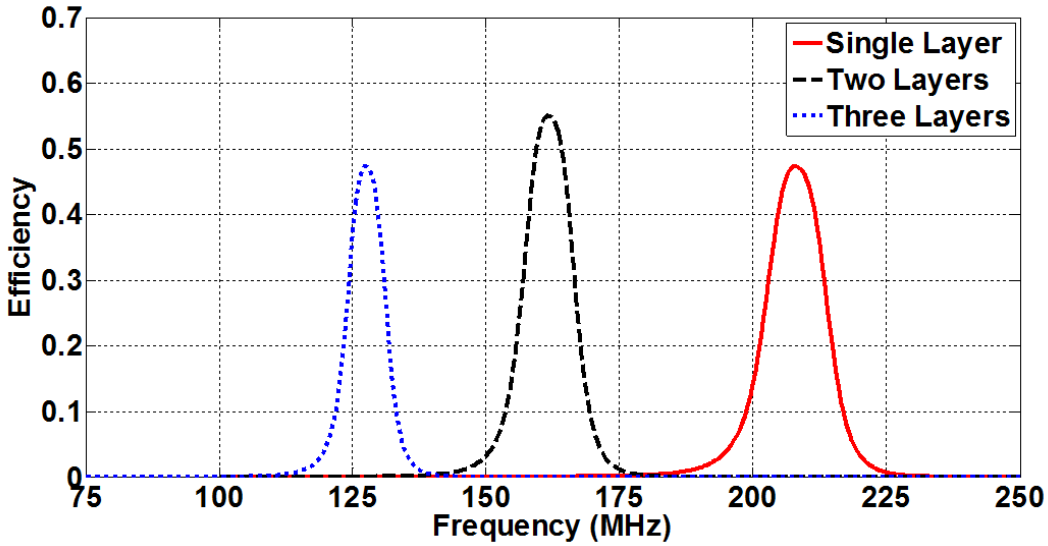

Figure 5.20. Simulated results of three systems.

5.4 Substrate Effect

The printable CSCMR systems are all built on the substrate. Therefore, the properties of the substrate will have some effects on the performance of the CSCMR system. In the following sections, we mainly discussed the effects of the thickness and dielectric properties of the substrate.

5.4.1 Effect of Thickness

The effects of the substrate thickness in the planar CSCMR systems are examined. For the sake of consistency, we still use the same system in Figure 5.1. Efficiencies of CSCMR systems for various thicknesses of FR4 substrates are shown in Figure 5.21, which shows the thickness of the substrate does not significantly affect the operating frequency of CSCMR systems. Therefore, planar CSCMR systems can be very thin without sacrificing performance. A prototype of an ultra-thin printable CSCMR is shown in Figure 5.22. This enables the TX and RX elements in the planar CSCMR systems to be

flexible for use in different applications, such as wearable devices or implantable devices. In fact, ultra-thin CSMR designs can provide volume savings and can be printed on flexible boards.

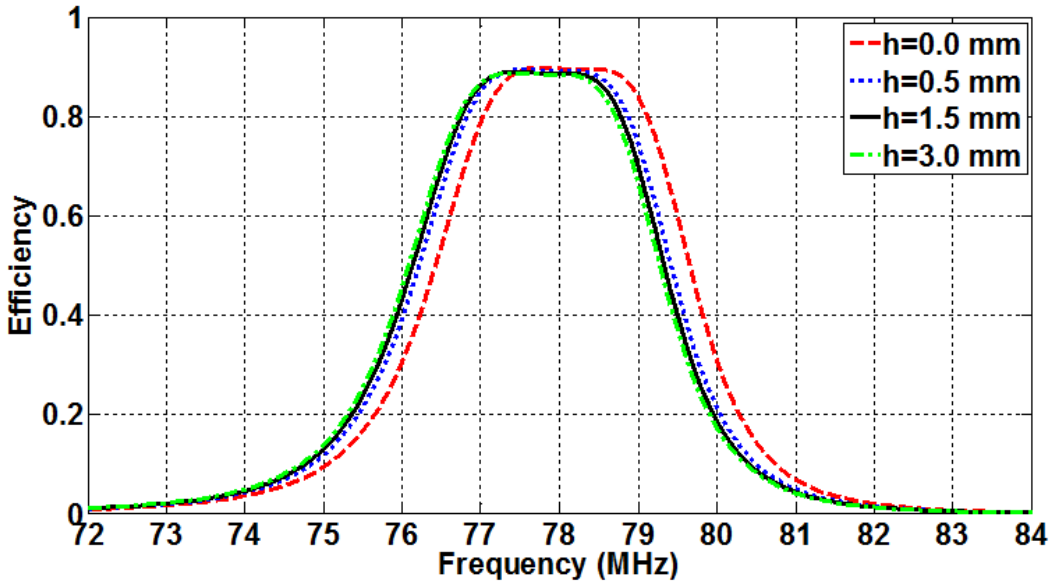

Figure 5.21. Simulated efficiency of CSCMR system in Figure 5.1 for different substrate thicknesses.

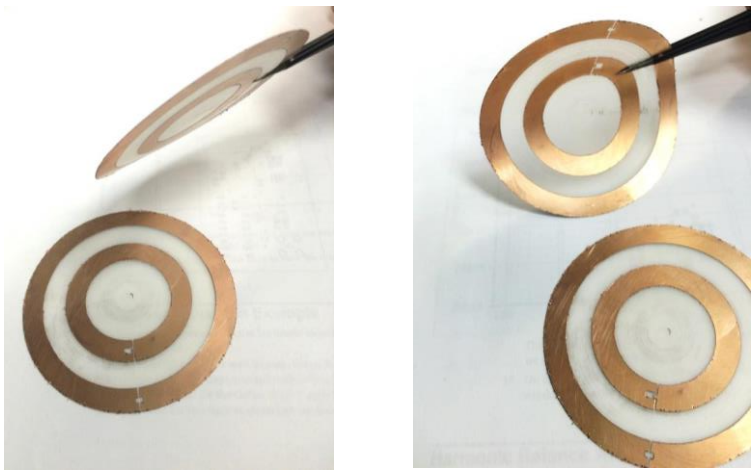

(a) (b)

Figure 5.22. Prototype of an ultra-thin planar CSCMR. (a) TX and RX element. (b) One bent TX/RX element.

5.4.2 Effect of Dielectric Properties

Properties of the substrate also affect the system performance. Using high dielectric constant or permittivity substrate, the operating frequency shifts to lower frequencies. Two ferrite sheets with the properties of ε=12, μ=1000 are adhered to the back of FR4 boards, as shown in Figure 5.23. Figure 5.24 shows these ferrite sheets shift the operating frequency from 83 MHz to 54 MHz while maintaining the same high efficiency.

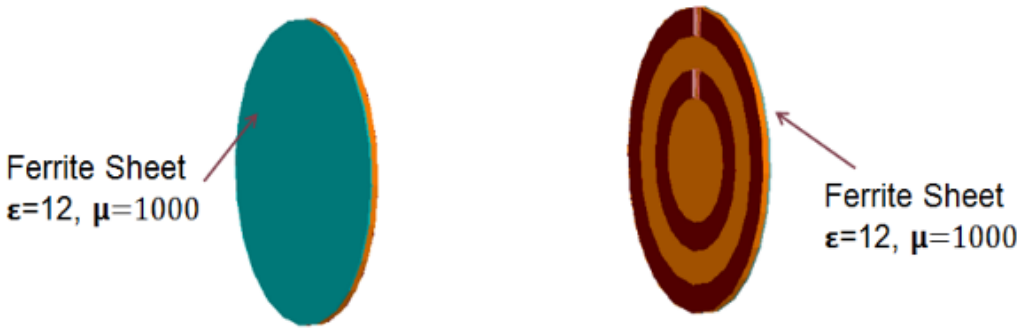

Figure 5.23. A CSCMR WPT system with ferrite sheets at the back of FR4 substrates.

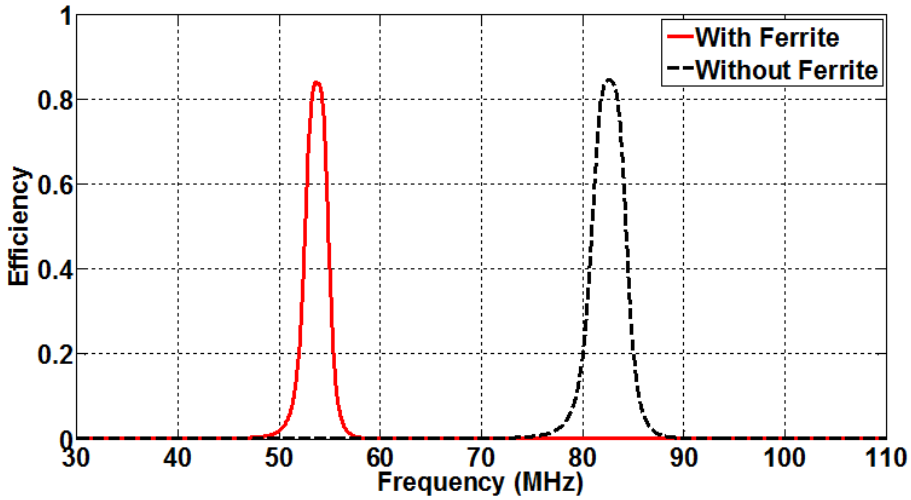

Figure 5.24. Simulated efficiency of CSCMR WPT systems with and without ferrite sheets.

CHAPTER 6

CSCMR SYSTEM IN VARIOUS APPLICATIONS

In this chapter, the CSCMR WPT systems applied in various applications are discussed. The performance of the CSCMR WPT systems under different applications is firstly discussed in Section 6.1. A CSCMR system design for biomedical devices is proposed in the following section. The misalignment property of the CSCMR system is finally studied and applied to power multiple devices simultaneously.

6.1 CSCMR under Different Applications

The CSCMR system can be used to power different sensors and devices under a variety of applications. Therefore, the performance of CSCMR system in various media is studied.

A typical printable CSCMR system is used as an example, as shown in Figure 6.1. The TX and RX elements are identical with same parameters. The radius of the outer loop is 29 mm. The radius of the inner loop is 16 mm. The widths of the copper loops are all picked as 6 mm. The lumped capacitor is chosen as 33 pF. All experiments are measured with a distance of 60 mm between TX and RX elements. The typical printable CSCMR system is tested when copper sheet, plastic sheet, ferrite sheet, and a package of water are placed between TX and RX elements. The experiments are shown in Figure 6.2. Measured results are listed in Table 6.1, which show that power can go through dielectric materials, such as plastic, water and paper, but will be reflected by materials, such as metal or ferrite.

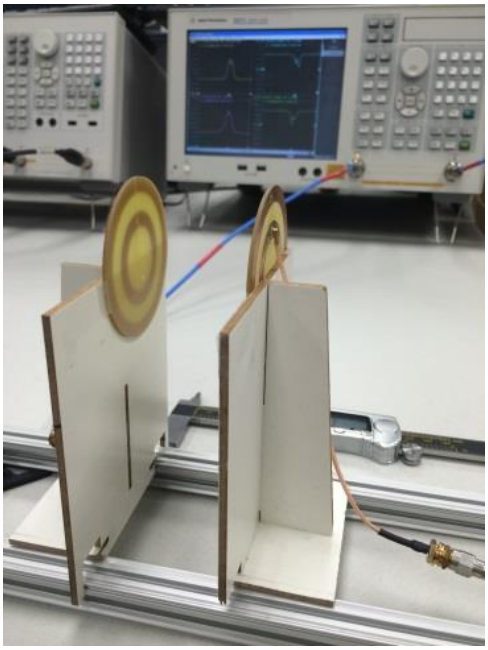

Figure 6.1. A typical printable CSCMR system in air.

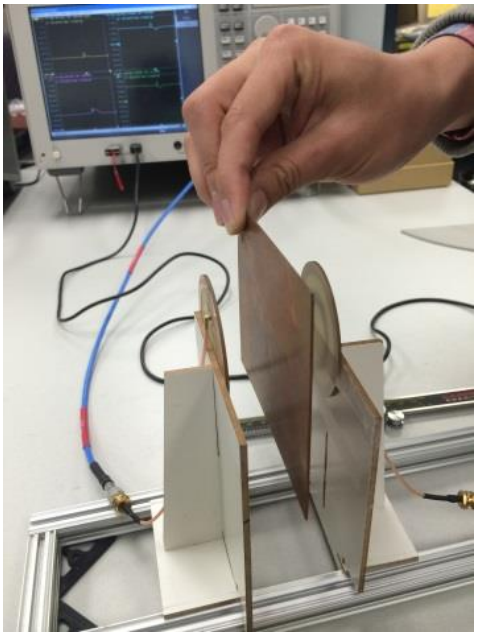

(a)

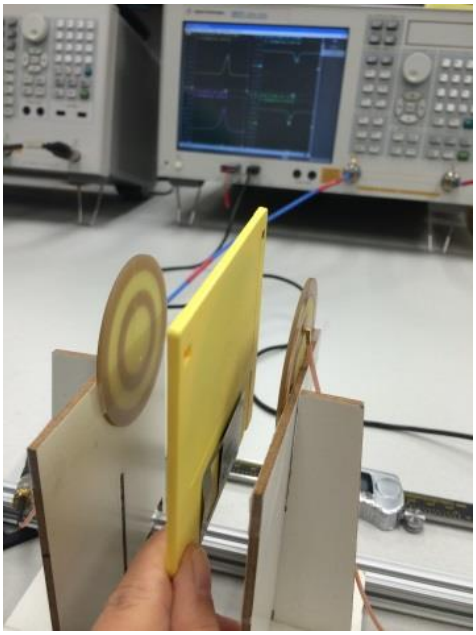

(b)

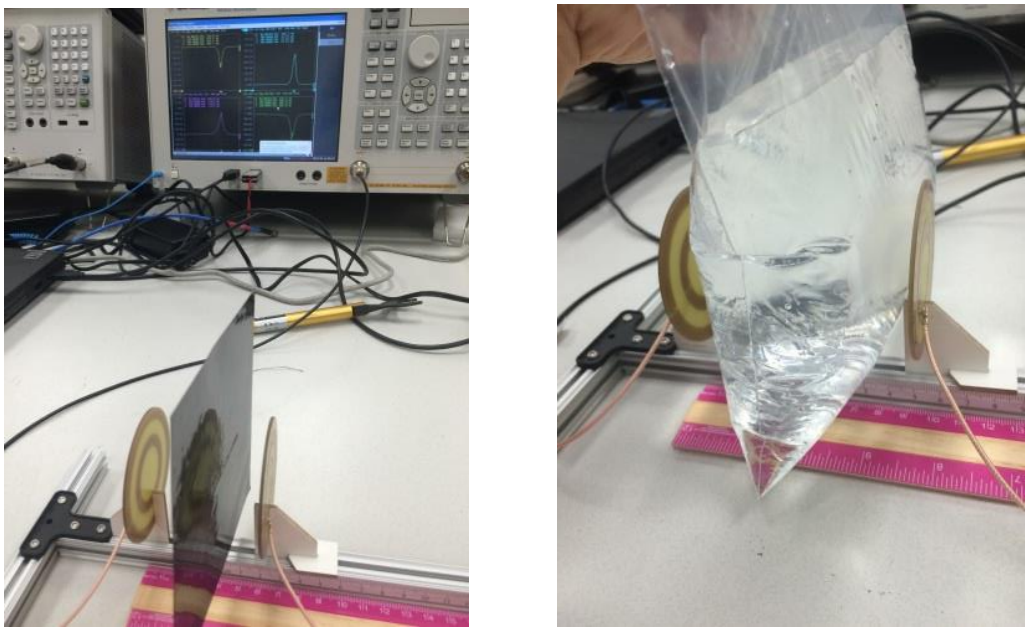

(c) (d)

Figure 6.2. A typical CSCMR System is in various environments. (a) Copper sheet between TX and RX. (b) Plastic sheet between TX and RX. (c) Ferrite sheet between TX and RX. (d) A package of water between TX and RX.

Table 6.1. Comparison of CSCMR WPT Systems in Various Environments.

Environments	Working Frequency (MHZ)	Maximum Efficiency (%)
In air	83.51	73.30
Whole copper sheet between	85.6	5.26
Half copper sheet between	85.6	60.70
Plastic sheet between	83.51	73.30
Ferrite sheet between	83.3	54.13
Water Between	83.1	72.90

6.2 CSCMR for Biomedical Devices

Wireless power transfer (WPT) techniques have gained significant interest in recent years in many applications, especially for wearable and implantable medical devices. WPT methods can assist technologies for continuous health monitoring and early diagnosis of disease. Previously, near-field inductive coupling has been mainly used for WPT through human tissue [82-84]. However, inductive coupling has limited range and poor efficiency. Recently, the SCMR WPT method was used with improved efficiency and longer range.

6.2.1 CSCMR Design in Tissue

In this section, the effects different human tissues on the efficiency of SCMR are firstly analyzed in detail. The design process for printable Conformal SCMR (CSCMR) systems, which are suitable for wearable and implantable applications, is presented. Finally, two optimal CSCMR systems with RX element on surface of human chest and embedded in human heart or muscle are presented.

A planar tissue model was developed with various human tissue materials from the ANSYS male human body model. The electrical properties of human tissue are changing with frequency, which are reported in Cole-Cole dispersion model [85]. Table 6.2 summaries information of main tissues at three frequencies.

Table 6.2. Electrical Properties of Human Tissue at Different Frequencies.

Freq. (MHz)	Properties	Fat	Muscle	Bone	Heart
10	ε_r	13.67	160.0	78	293.5
	σ (S/m)	0.029	0.645	0.071	0.501
100	ε_r	6.07	66.19	29	90.82
	σ (S/m)	0.036	0.731	0.15	0.733
1000	ε_r	5.45	55.74	18.4	59.29
	σ (S/m)	0.054	1.006	0.32	1.284

A CSCMR system (D_o=12.8 mm, D_i=7.6 mm, w=1.2 mm) is designed to analyze its performance in human tissue. The source loop and TX loop as well as the load loop and RX loop are printed in one plane, see Figure 6.3. More details about CSCMR systems in air can be found in Chapter 3. Copper strips (0.035 mm thick) are printed on FR4 substrate with thickness of 1.5 mm. This system works at 455 MHz in air with capacitor of C=6 pF, system efficiency is 80% when TX and RX elements are 10 mm apart. The design considerations of CSMR systems for wearable and implantable applications will be discussed below.

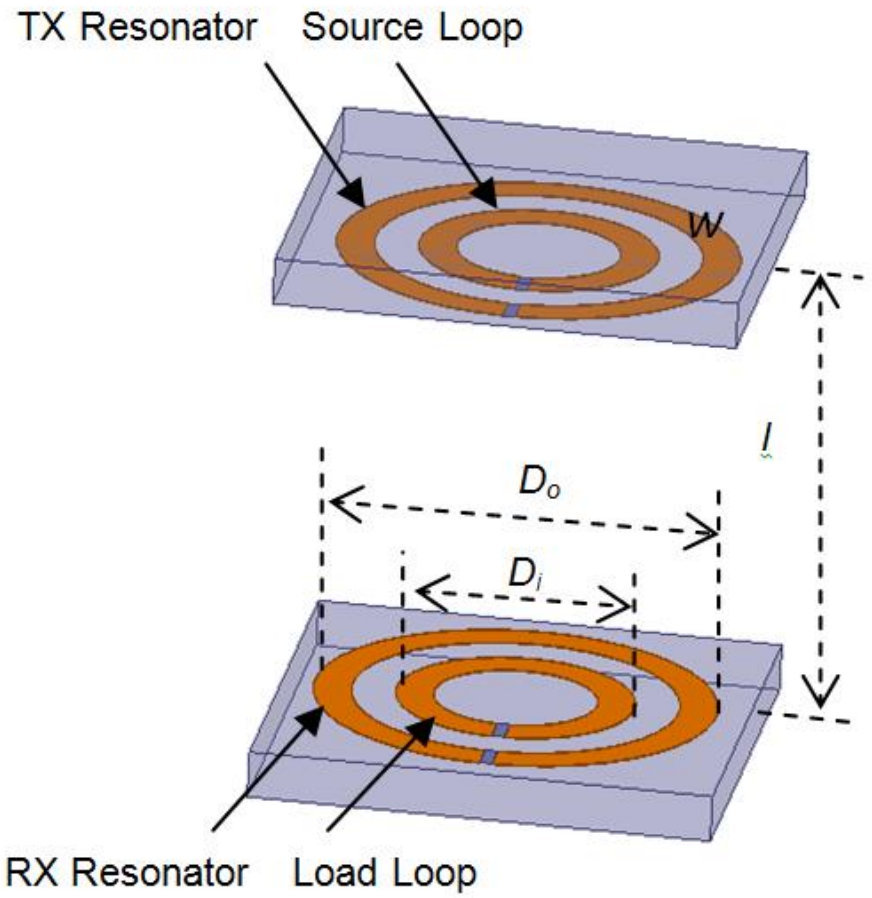

Figure 6.3. Geometry of printable conformal WPT SCMR system.

A. CSCMR with RX Element on Surface of Human Tissue

In order to simplify the simulation model, planar layered models with various tissue properties and thickness are built to represent the human tissue with EM simulation tool ANSYS HFSS, as shown in Figure 6.4. When RX element is placed on the surface of human tissue, WPT system performance will be affected by various tissues properties, like permittivity (ε_r) and electric conductivity (σ). The quality-factor, Q, of the receiver's resonating loop as well the frequency, where its maximum Q-factor (f_{Qmax}) occurs, will decrease as the permittivity and electric conductivity of the layer underneath it increase.

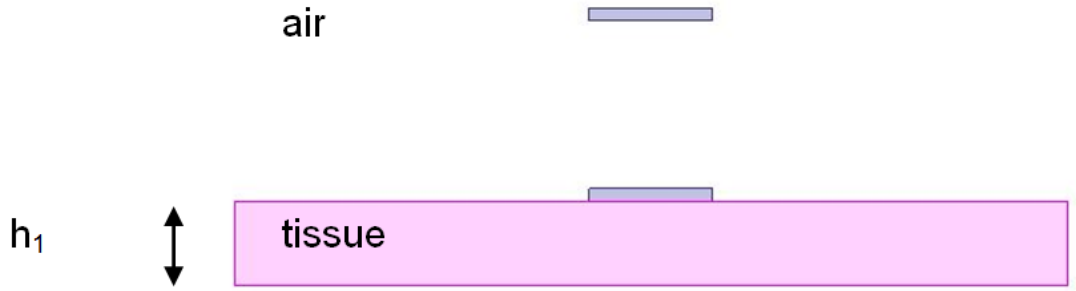

Figure 6.4. WPT system model with TX element is in air and RX element is on the surface of one tissue layer.

Effects of various thickness of one and multi-layered tissues are also studied. Figure 6.5 shows the Q-factor versus different thicknesses of muscle tissue. Other tissue simulation results show that thickness of one layer do not significantly affect the Q-factor. Also, f_{Qmax} shifts to lower frequencies as thickness increases. This shift is more significant when the tissue has with large high permittivity or conductivity.

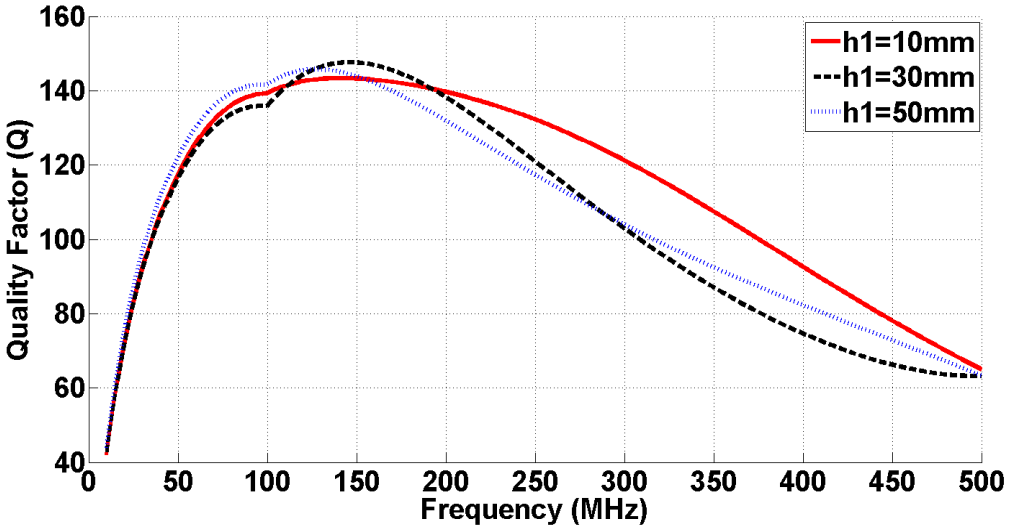

Figure 6.5. Quality-factor variations regarding to different thicknesses of muscle tissue.

When multilayers are included in human tissue model, such as Figure 6.6, the effects of the thicknesses of various tissues are also studied. Figure 6.7 illustrates *Q*-factor variations for different thickness of three tissues: skin, fat, and muscle. It shows that the *Q*-factor will decrease significantly as the thickness of muscle tissue increases. Other tissues with low permittivity (ε_r) and electric conductivity (σ) like the skin and fat tissues do not significantly affect the *Q*-factor.

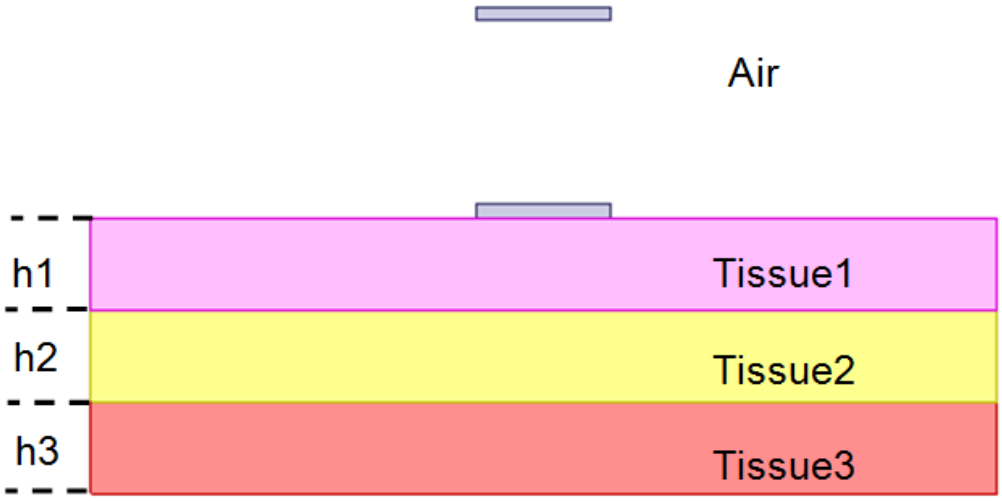

Figure 6.6. CSMCR system with TX element in air and RX element on the surface of tissue.

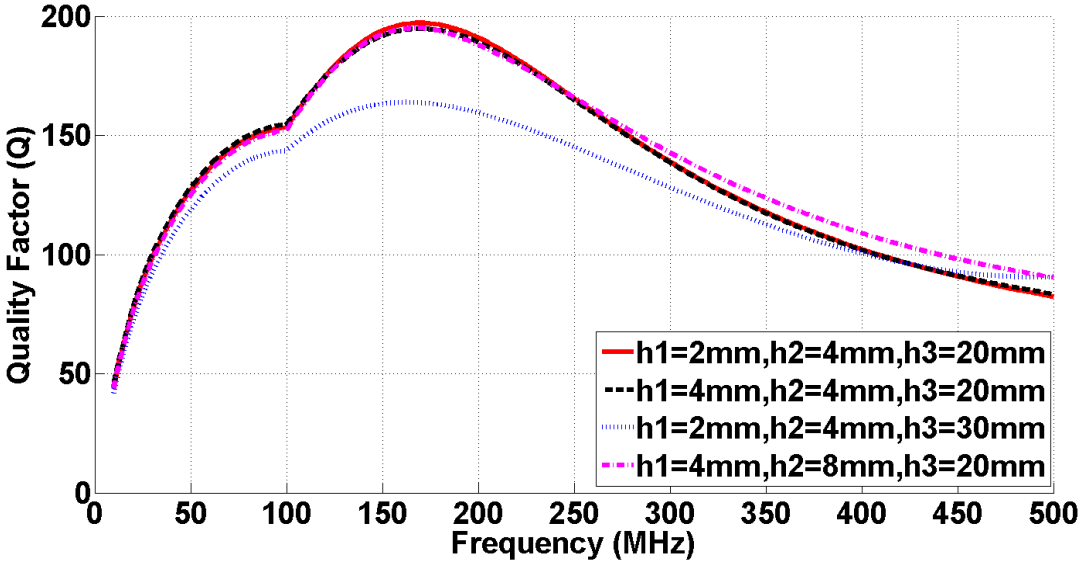

Figure 6.7. Quality-factor of CSMR RX element on multilayered tissue with different thicknesses, h_1, h_2 and h_3 present the thickness of skin, fat and muscle tissues.

B. WPT with RX Element Embedded in Human Tissue

Similar planar layered models are also used to study WPT systems for implantable devices. Considering implantable devices need a compact size and the permittivity of FR4 substrate is much lower than the human tissue, the board thickness is picked to be 0.75 mm, see Figure 6.8. Since the RX element is embedded in human tissue, performance will be significantly affected by various tissues properties, especially the electric conductivity (σ), see Figure 6.9.

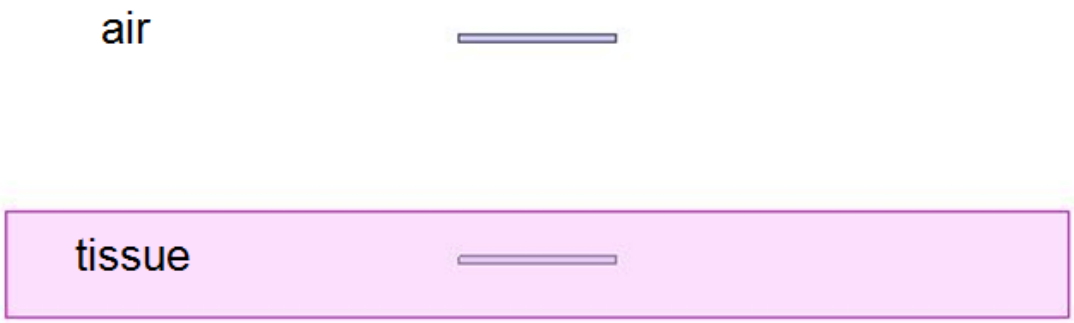

Figure 6.8. WPT system model with TX element is in air and RX element embedded in tissue.

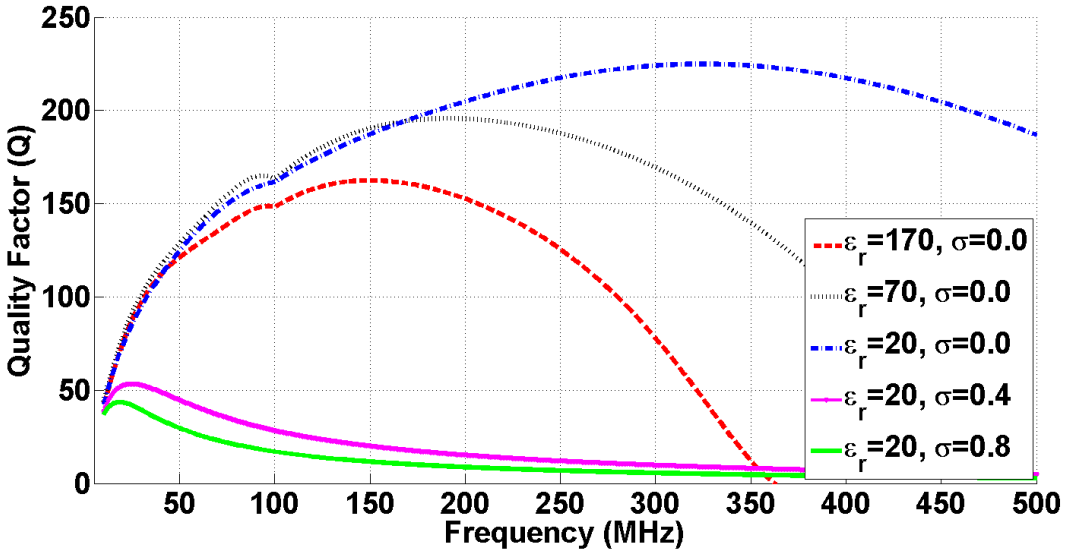

Figure 6.9. Quality-factor variations regarding to various tissues with different permittivity (ε_r) and conductivities (σ).

In order to achieve efficient WPT the TX and RX resonators should work at the same frequency and with high *Q*-factor. A small air-box is used around the RX element to enhance its *Q*-factor (see Figure 6.10). Also, the air-box can be incorporated in the packaging that will protect the RX inside the human body. Figure 6.11 shows that when

an air-box with thickness of 1.5 mm is used around the CSMR RX in muscle tissue, its Q-factor increases significantly from 40 to 120.

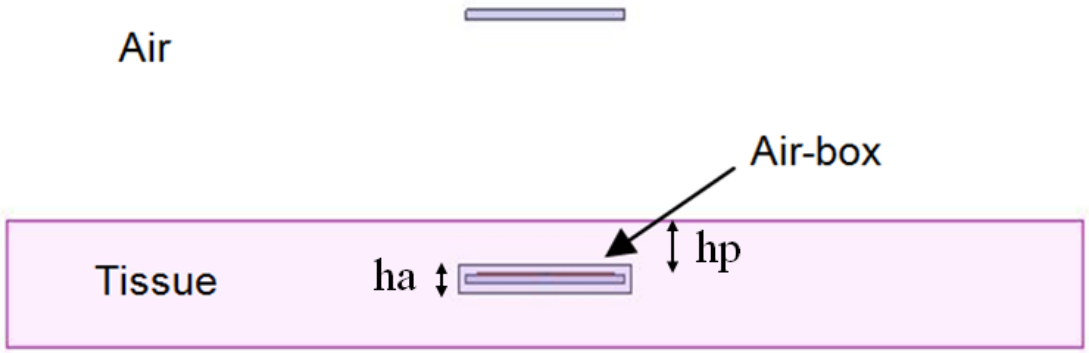

Figure 6.10. WPT system model with TX element is in air and RX element embedded in tissue with an air-box.

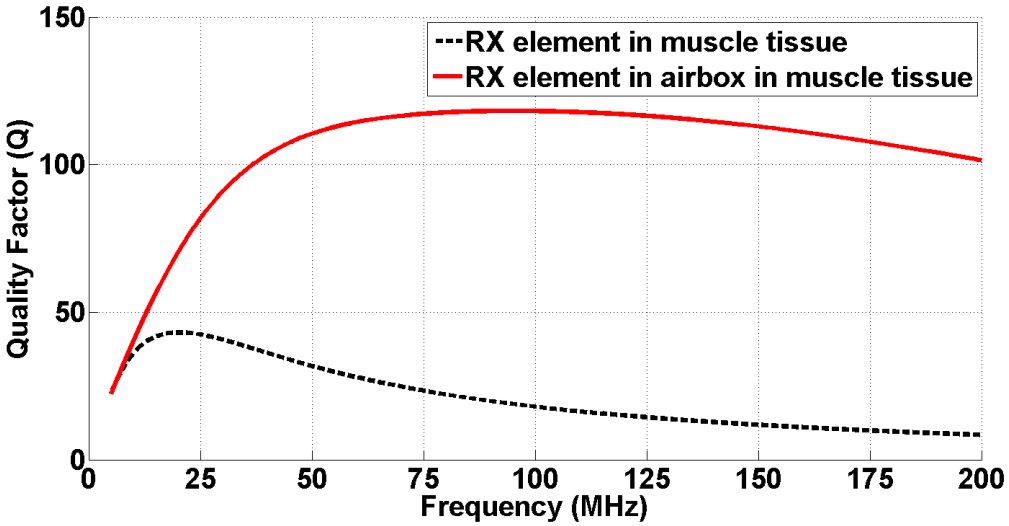

Figure 6.11. Quality-factor of CSMR RX elements in muscle tissue with and without an air-box.

Also, the thickness of the air-box and the implantation depth of the CSCMR RX will also affect the *Q*-factor. Simulation results with various thicknesses of air-box and

implantation depths are shown in Figure 6.12 and Figure 6.13 They show that under implantable biomedical constrains, higher Q-factor will be achieved when the RX element is embedded superficially or with thicker air-box.

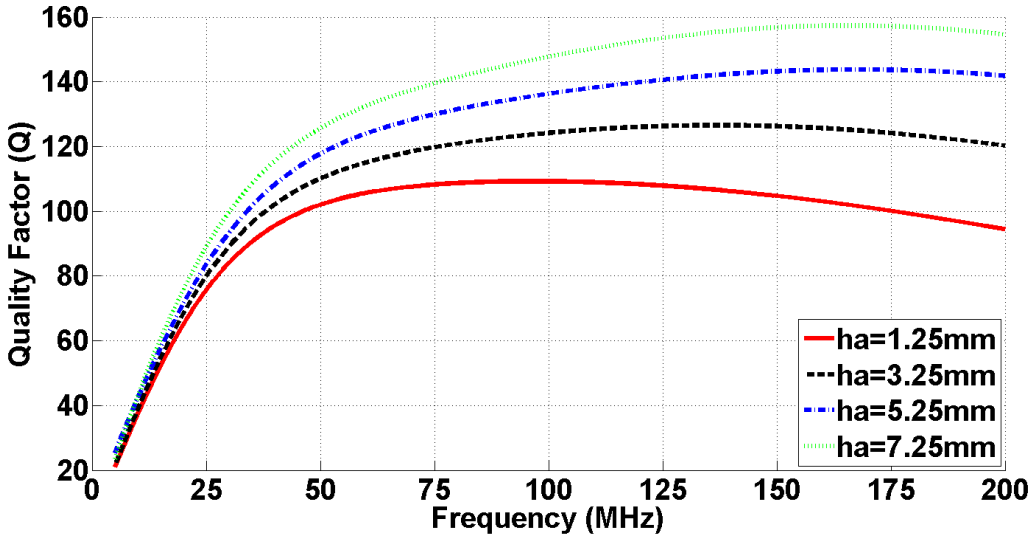

Figure 6.12. Quality-factor of CSMR RX elements in muscle tissue with various thicknesses of air-box.

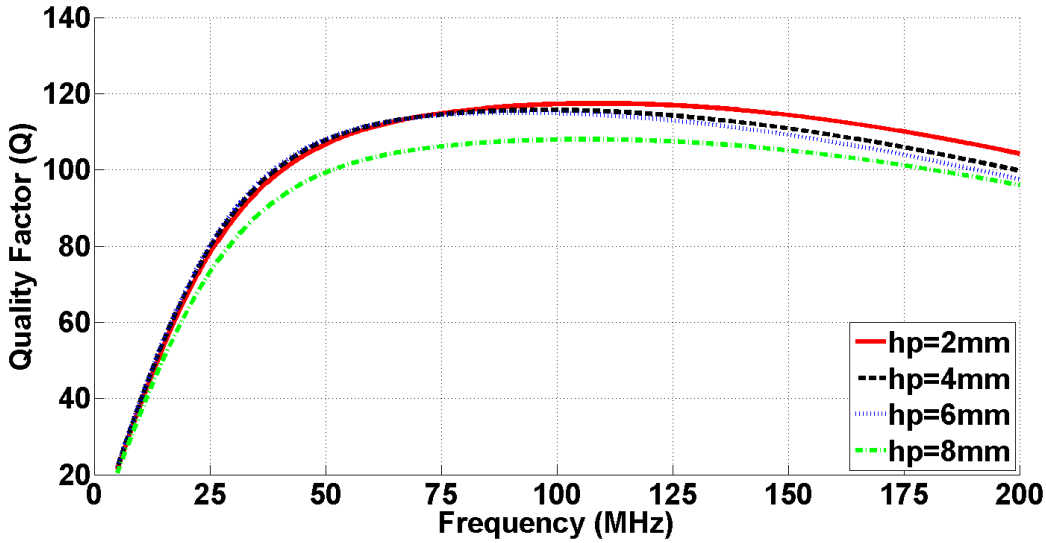

Figure 6.13. Quality-factor of CSMR RX elements in muscle tissue with various embedded depth.

C. CSCMR System with RX Element on Surface of Human Chest

Based on our findings from the previous sections, two optimal CSCMR systems are designed: one with the RX element on surface of human tissue and one with the RX element embedded in human tissue.

The RX element is designed to operate on the surface of human chest. The following layers exist: skin layer, fat layer, muscle layer, cancellous bone layer and heart layer. The thickness of each layer is h_1=2 mm, h_2=4 mm, h_3=20 mm, h_4=10 mm, and h_5=30 mm, respectively. The RX has the following dimensions: D_{o1}=12.8 mm, D_{i1}=7.6 mm, and w=1.2 mm. Simulation model is shown in Figure 6.14.

Based on HFSS analysis, the Q-factor of this CSMR RX resonator is maximum at 140 MHz. Also, its inductance is calculated as L_1=19 nH in Ansoft Designer and the required capacitance is calculated as C_1=68 pF. The TX element is designed with the following parameters: D_{o2}=36 mm, D_{i2}=20 mm, w=3 mm, and C_2=22 pF.

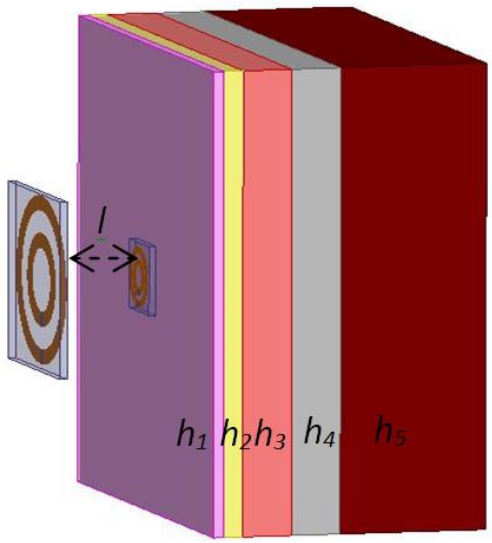

Figure 6.14. CSCMR system with RX element on surface of skin-fat-muscle-bone-heart tissue.

The WPT efficiency of this CSMR system is defined as the square of the magnitude of S_{12} and is calculated using ANSYS HFSS. An efficiency of 56% is achieved when the distance between TX and RX elements is 20 mm. Figure 6.15 also illustrates the efficiency of the CSMR system for different distances between the TX and RX.

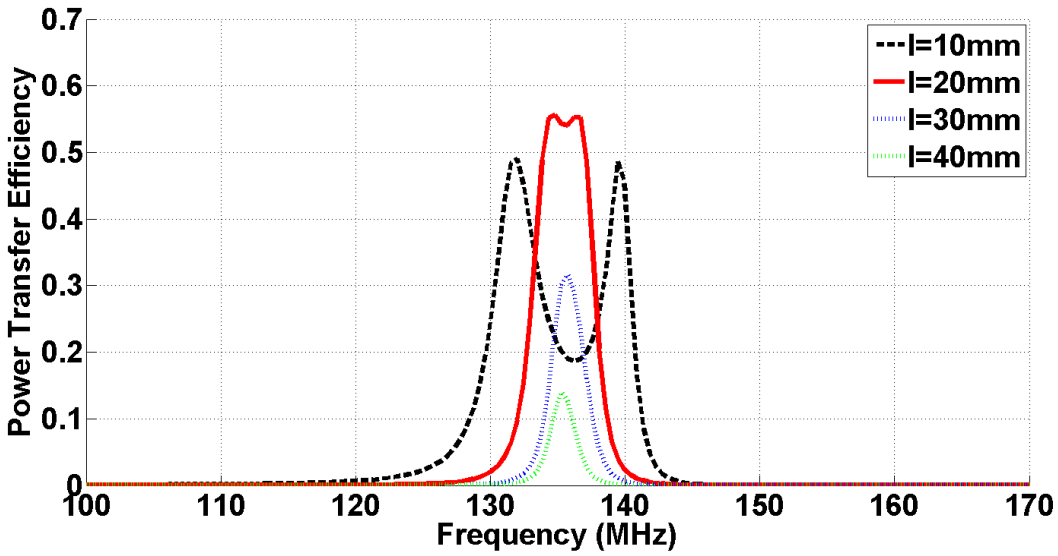

Figure 6.15. Efficiency of wearable CSCMR system for different distances.

D. CSCMR Design with RX Element embedded in Human Heart or Muscle

This implantable CSCMR system uses the same RX element that was used in the wearable case of the previous section. A 1.25 mm-thick air-box surrounds the RX element and the RX is embedded in the heart at a 2 mm depth, as shown in Figure 6.16(a). Based on our simulation results, the RX resonator exhibits maximum Q-factor at 91MHz. Following a similar design procedure as before, the CSCMR system is designed with the following parameters: C_1=149 pF, D_{o2}=55 mm, D_{i2}=29 mm, w=5 mm, C_2=33 pF. This system achieves an efficiency of 24% at 91 MHz when the distance between RX and TX

is 31 mm. Then, the RX element is placed in the human muscle, as shown in Figure 6.16(b). By following a similar design procedure, a CSCMR system is designed with efficiency of 40% at 91 MHz when the distance between TX and RX is 28 mm. The simulation results for both systems are shown in Figure 6.17.

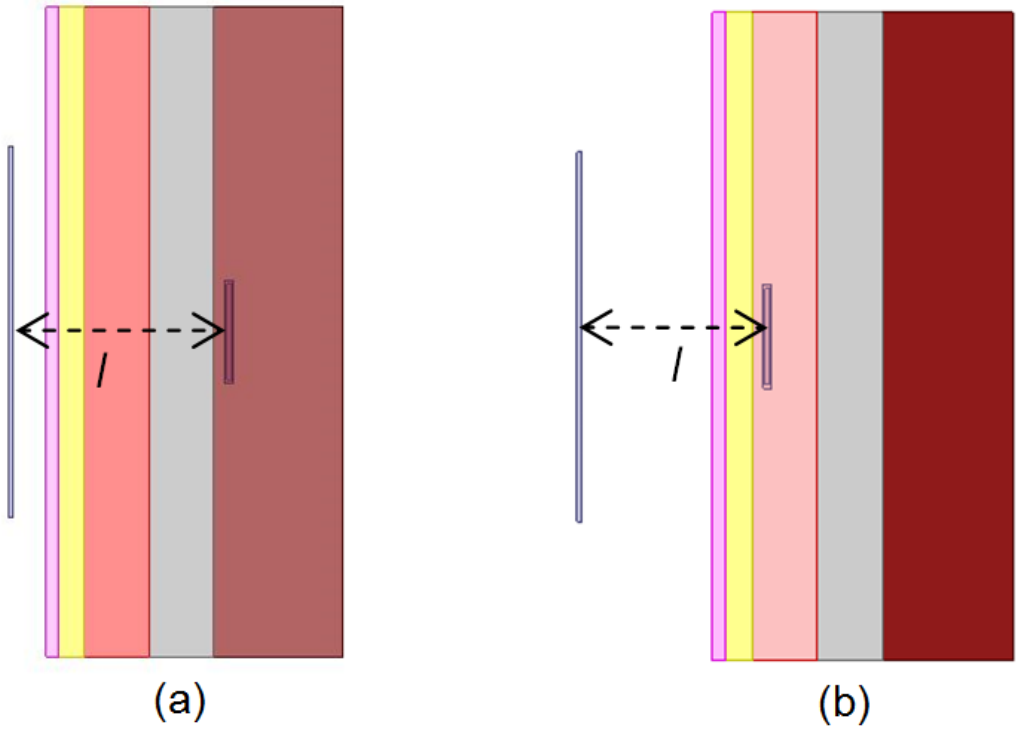

Figure 6.16. CSCMR model with RX element in (a) Human heart and (b) Human muscle.

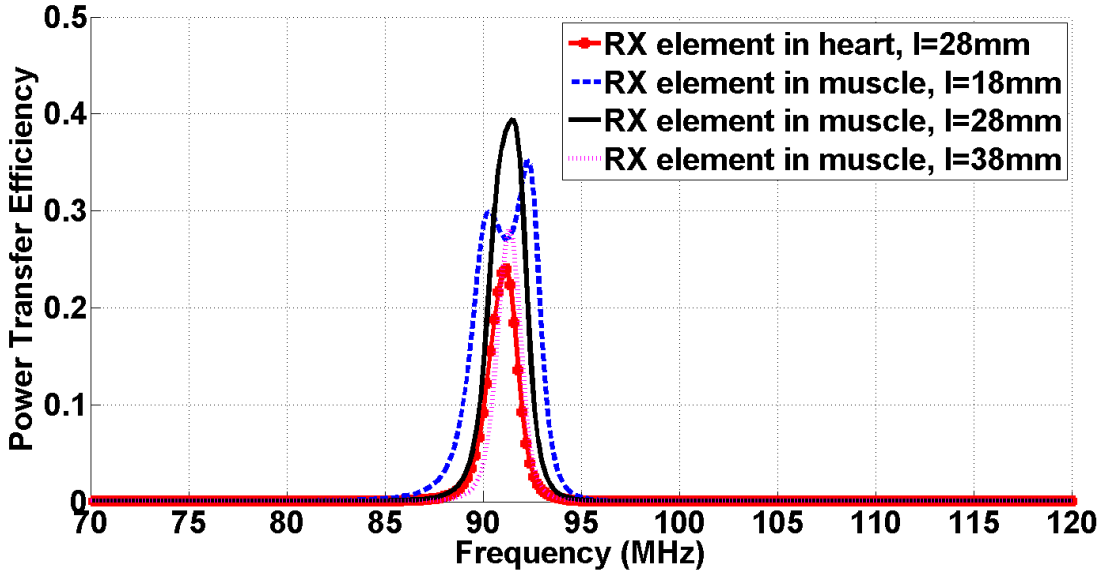

Figure 6.17. Efficiency of CSCMR system embedded in the human body at various depths.

6.2.2 CSCMR using Spiral for Biomedical Implants

Recently, biomedical implantable devices have played important role in monitoring, diagnostic and treatment applications [86-87]. The power supply is one very important aspect of implantable devices. Also, some implantable medical devices, such as, cardiac pacemakers use half of their battery power for cardiac stimulation and the other half for housekeeping tasks, such as, monitoring and data logging [88-90]. Therefore, sufficient power supply must be provided for implantable medical devices to work properly. Typically, batteries are used. However, batteries of biomedical implantable devices cannot be easily replaced. For example, in many implantable devices, batteries are hard wired at the time of manufacturing to the device and the device is hermetically sealed. Also, replacement of batteries requires a surgical operation that imposes risks to patients' health [91].

Therefore, wireless power transfer technology for implantable biomedical devices is greatly needed. Inductive coupling has been traditionally used for wireless power transfer [92-93]. However, the TX element and RX element are required to be placed very close to each other; otherwise, such a system suffers from very poor power transfer efficiency. In addition, transmitting power levels have a limit to avoid overheating of living tissue, which may result in tissue damage. Based on the recommendation of safety level defined in IEEE standard and FCC guidance, the exposure to radio frequency (RF) energy should be limited to a maximum Specific Absorption Rate (SAR) value of 1.6W/kg for 1g of tissue [50-51]. Given this constraint, efficiency is of great importance for wireless power transfer in implantable biomedical devices.

Previous proposed self-resonant CSCMR system is used that does not need lumped capacitors. This proposed system simplifies the fabrication process and is suitable for implantable and wearable biomedical devices. The resonator topology is shown in Figure 6.18. The spacing between each turn of the spiral structure provides the required capacitance and the copper strip provides the distributed inductance. Therefore, by adjusting the width and thickness of the strip (w, t), the distance between the turns (s), and the radius of the first turn (r_1), the spiral resonator can operate at the desired frequency, where its Q factor is maximum. Also, tuning the radius of the source or the load (r_0) can also affect the system performance.

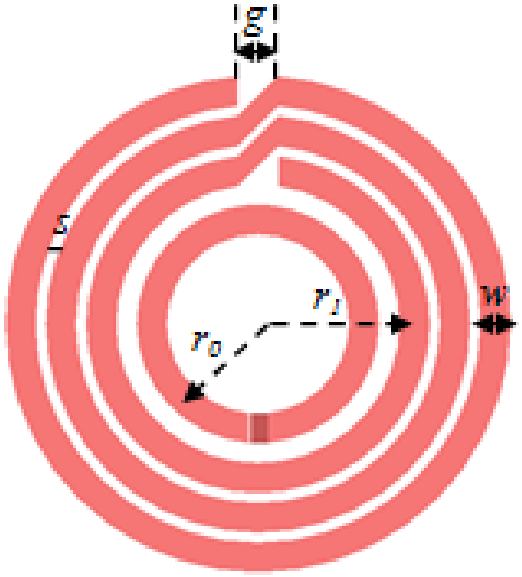

Figure 6.18. Sketch of a three-turn spiral resonator.

When developing a self-resonant CSCMR for biomedical implants, some parameters should be adjusted from the one working in air due to the different material properties of the human body. The geometrical specifications of our design for wireless power transmission to biomedical implants are listed in Table 6.3. The area of the RX element inside the human body is approximately 50 mm × 50 mm. In order to avoid touching the tissue and achieving high efficiency, the RX element is surrounded by a small air box with thickness of 5 mm.

Table 6.3. Parameters of Simulated Model for Biomedical Implants

TX/RX	Structure Parameters (mm)				
	r_0	r_1	s	w	t
TX	9.5	15.5	1	3	1
RX	11	15.5	1	3	1

Our simulation model that includes the human body is displayed in Figure 6.19. Our simulated results for different distances between the implanted RX element and TX element are illustrated in Figure 6.20. It can be seen that an efficiency of 46.7% is achieved at 223 MHz for the distance of 30 mm. Also, the electromagnetic field and SAR distributions are given in Figures 6.21 and 6.22. Different wireless power transfer methods are compared in Table 6.4. It is shown that our proposed CSCMR method requires the least amount of transmitting power in order to deliver the same power inside the human body. Therefore, our method can be used to provide significant amount of power to implantable devices without overheating tissues.

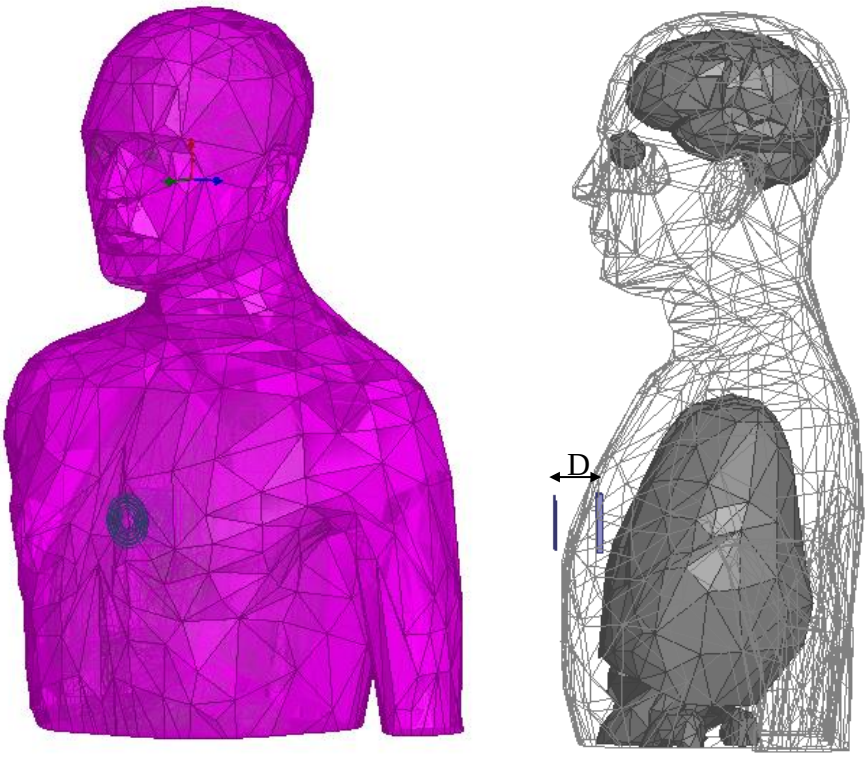

Figure 6.19. Human body with self-resonant CSCMR system.

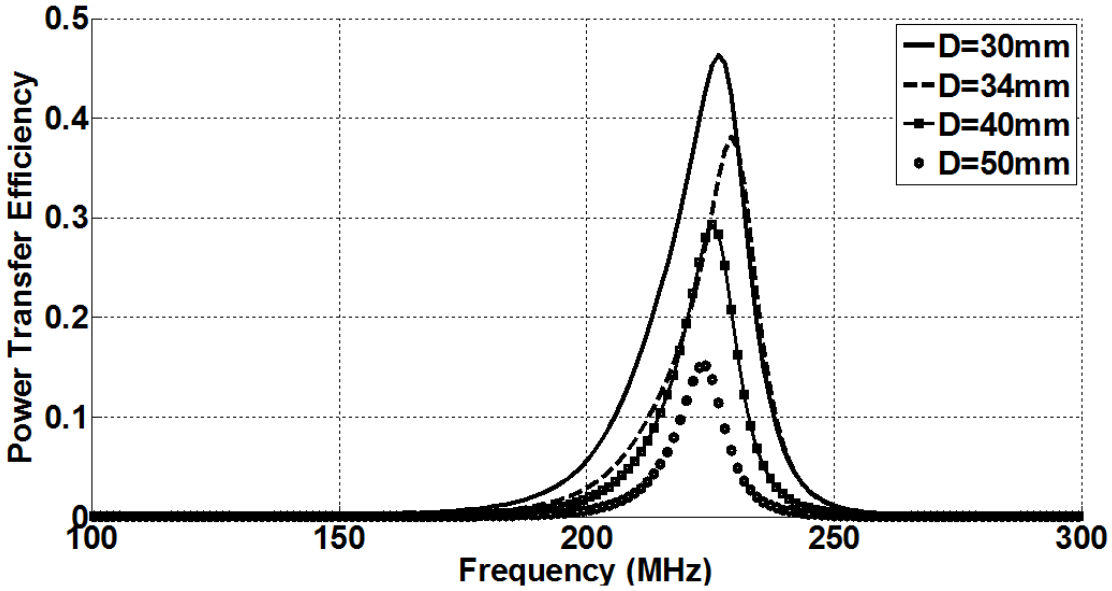

Figure 6.20. Simulated results regarding to different distances for biomedical implants.

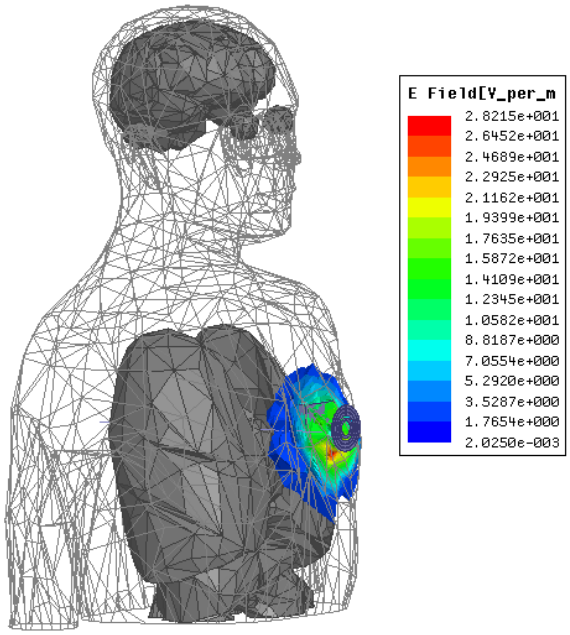

(a)

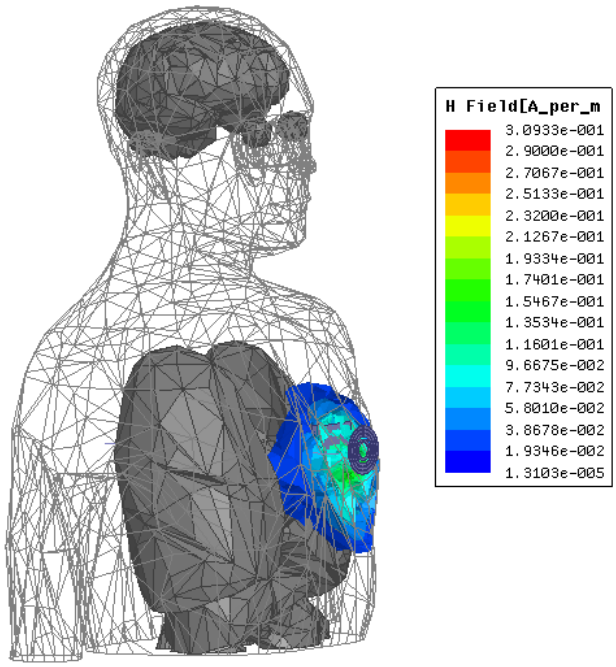

(b)

Figure 6.21. Electromagnetic field distribution. (a) E field. (b) H field.

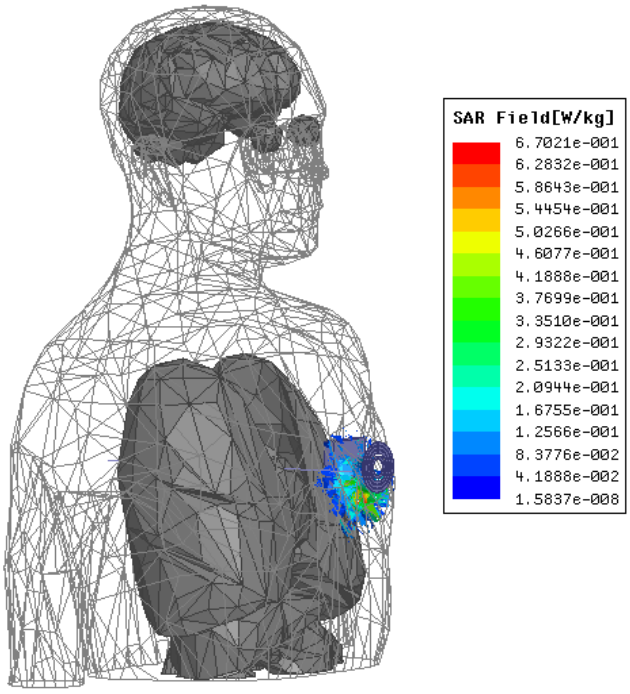

Figure 6.22. Simulated SAR Distribution.

Table 6.4. Comparison of Different Wireless Powering Systems for Output Power of 467 mW.

Coupling Type	Field Parameters and Efficiency			
	Input Power (w)	Max H-field (A/m)	Max SAR (W/kg)	Efficiency (%)
Resonant Coupling	93	35	25	0.5%
SCMR	1.3	5	1	35%
CSCMR	1	0.31	0.67	46.7%

6.3 Misalignment Study of CSCMR

In the study of previous SCMR methods, the TX resonator and RX resonator should be align coaxially in order to achieve maximum coupling between each other. When misalignment happens, the system efficiency drops drastically. This brings great inconvenience in many practical applications.

6.3.1 Misalignment Insensitive

Compared with traditional SCMR, the planar CSCMR achieves excellent misalignment at any position within the plane where all loops located. Two orientation misalignments is illustrated in Figure 6.23. For angular azimuth misalignment, the RX element rotates in the XY-plane around Z-axis from φ=0° to 360°. For angular elevation misalignment, the RX element rotates in the YZ-plane around X-axis from θ=0° to 360°. Performance for various orientation misalignments is simulated in Figure 6.24. It shows that excellent misalignment can be achieved in azimuth plane. Using the proposed

method, RX resonator can be moved around the TX resonator in the same plane without scarifying efficiency, which has great applications in portable communication devices.

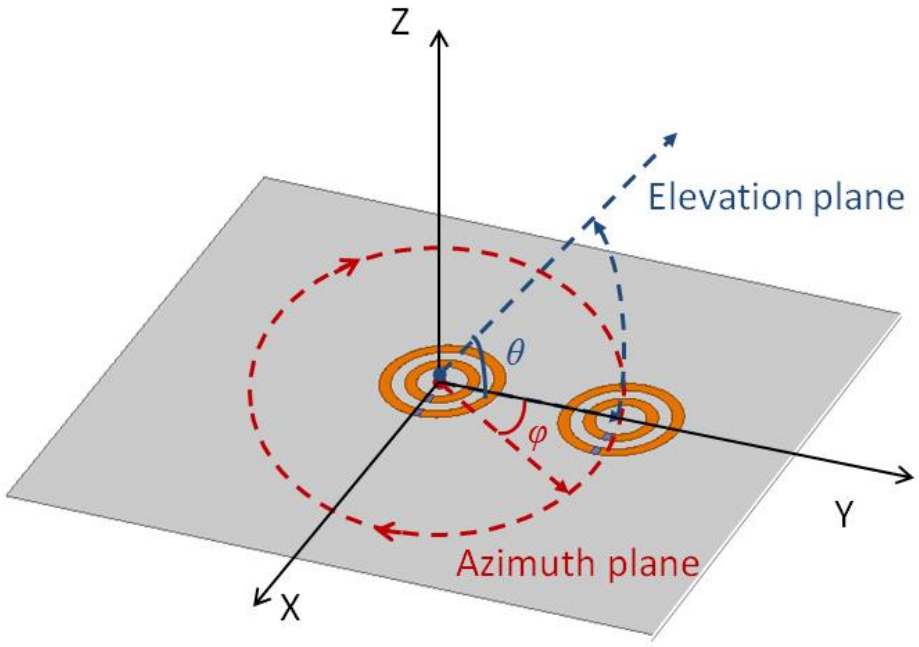

Figure 6.23. The RX element of a planar CSCMR system sweeps in an azimuth plane with misalignment angle, φ, or in an elevation plane with misalignment angle, θ.

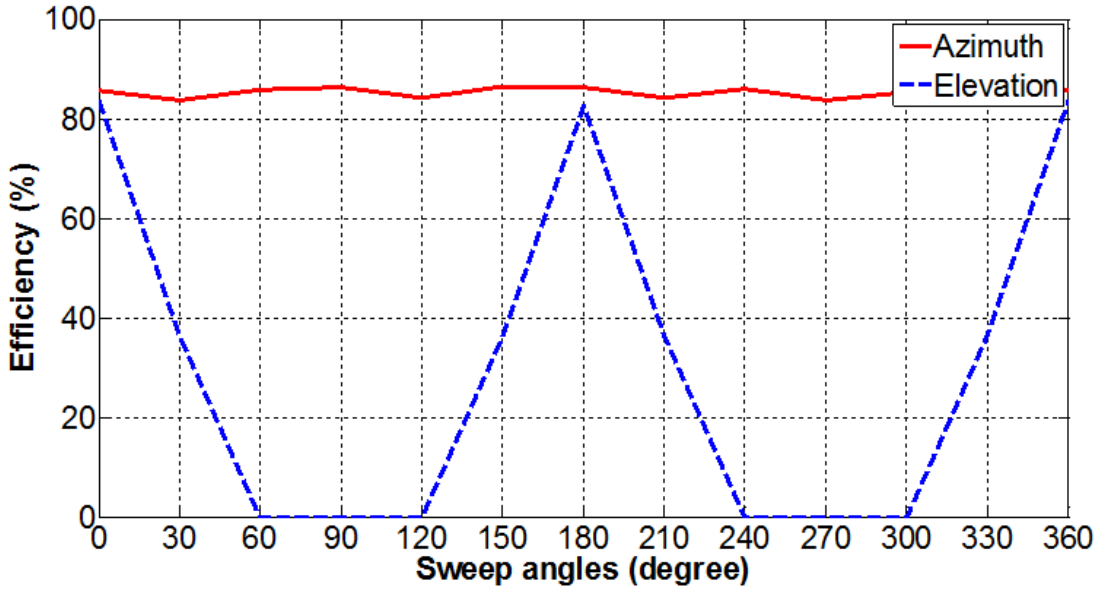

Figure 6.24. Simulated efficiencies of a CSCMR WPT system under azimuth and elevation misalignment conditions.

6.3.2 Charging Multiple Devices Simultaneously

In many applications, one wireless power transmitter and multiple receivers are needed. With only one transmitter, WPT systems can save space and cost, as well as achieve flexibility in use. CSCMR WPT systems can be used to simultaneously charge multiple devices in the same plane or out of the plane due to their high efficiency and misalignment insensitivity for coplanar transmissions, as discussed in the previous section. A prototype system for charging multiple devices is shown in Figure 6.25. The transmitter is located in the center of the lower plane, which is also a typical CSCMR design based on two copper loops. Receivers A-D are all placed on the same plane with transmitter. They can be loaded with different LED devices, circuits or sensors. The Receiver E is 80 mm away on top of the transmitter. In this setup, the receiver E is connected with a temperature sensor.

When this system is operating, all receivers can be powered simultaneously. Figure 6.26 shows that all the LED devices in the same plane with the transmitter are lighting while the temperature sensor is working and room temperature is read.

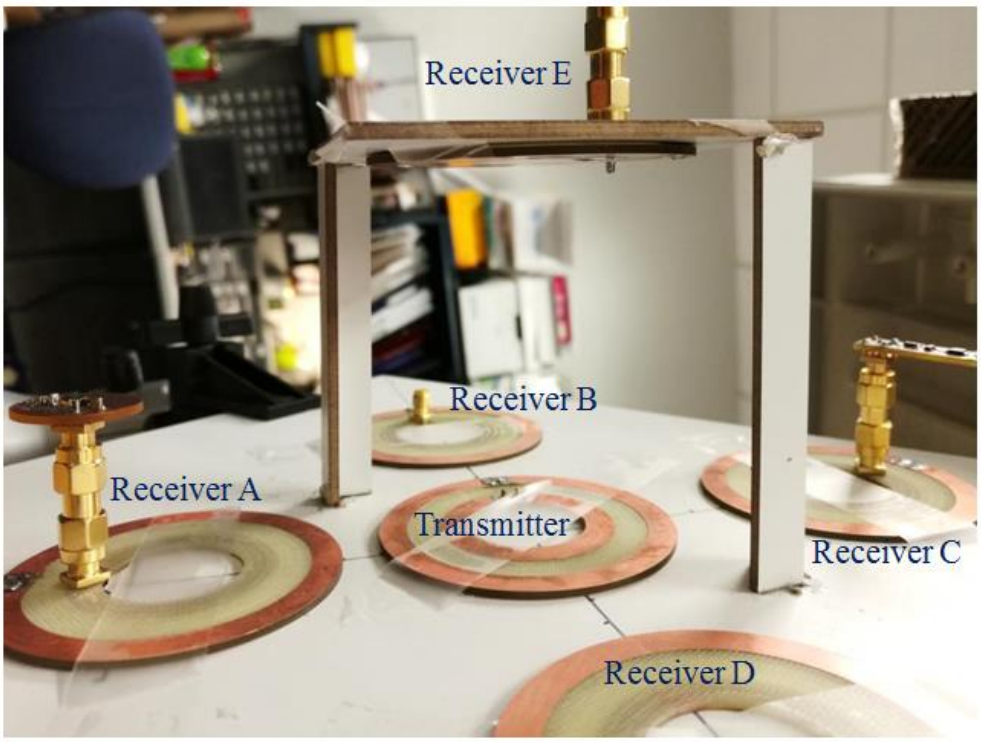

Figure 6.25. Prototype system for charging multiple devices.

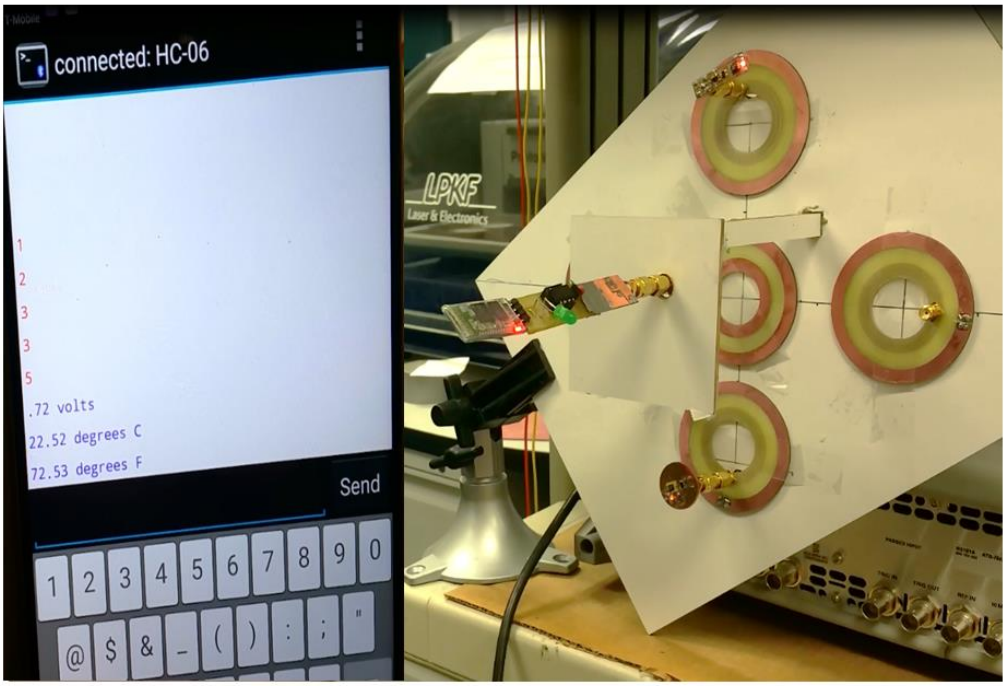

Figure 6.26. Multiple devices operate simultaneously.

CHAPTER 7

CONCLUSION AND FUTURE WORKS

7.1 Conclusions

This dissertation presented a comprehensive analysis of optimal and miniaturized SCMR systems for WPT in various applications, such as multiband, broadband WPT systems, sensors and biomedical implants.

We started our research by developing analytical models for CSCMR systems with multiple resonators, which can be used to study and predict the performance of such systems. The optimal designs were developed using a theoretical analysis based on the proposed equivalent circuit models of CSCMR systems. The efficiency of CSCMR WPT systems was calculated using the proposed analytical model as a function of geometrical and material parameters. Therefore, this analytical model can provide a straightforward way to design SCMR systems that are optimal (in terms of their efficiency and frequency splitting) at the desired frequency.

Multiband and broadband CSCMR WPT systems based on the optimal designs were also investigated. Optimal multiband CSCMR systems with two, three, and four bands were examined in order to validate our analytical results through comparisons with simulations and measurements. These systems can efficiently transmit power in different bands, and can be used for applications where a single WPT TX system needs to power devices or sensors of different sizes at different distances. Also, multiband WPT systems can be used to provide compatibility with different WPT standards. Broadband CSCMR systems are presented and design guidelines for optimal broadband CSCMR systems are

developed and discussed. The proposed broadband CSCMR system significantly broadened the bandwidth of traditional SCMR systems. In fact, the prototyped broadband CSCMR system achieved more than 7 times larger bandwidth compared to the traditional SCMR system at the same frequency. This design can be particularly useful when power and data need to be wirelessly transferred through the same wireless link.

Furthermore, miniaturization based on various methods for SCMR systems was investigated. A printable CSCMR system using large capacitors was firstly studied. New topologies, such as meander, SRRs, spiral and 3-D structures changed the self-inductance or self-capacitance of the resonators. Therefore, the operating frequency was successfully tuned to a lower frequency, thereby reducing the size of the CSCMR system. The miniaturized designs of SCMR systems are suitable for various applications, where maintaining a small size for a device is critical. They will significantly enhance the field of biomedical implants by providing small, highly efficient wireless powering systems that can support safe and wireless operation of bio-implants, thereby eliminating transcutaneous wires that can lead to discomfort and infection.

Finally, the performance of the CSCMR systems was studied in different applications. The results showed that power can go through dielectric materials, such as plastic, water and paper, but will be reflected by media, such as metal or ferrites. The effects of different human tissues on the efficiency of SCMR and the design process were also analyzed and presented. A CSCMR system based on self-resonant spirals was also designed for biomedical implants, which required the least amount of transmitting power in order to deliver the same power inside the human body compared to other different WPT methods. Using the misalignment insensitive property of the CSCMR system, a

WPT system that can power multiple devices simultaneously using only one transmitter was also designed and prototyped. This design saves space and cost, as well as achieves flexibility in many applications.

In conclusion, the new CSCMR systems that are optimally designed and miniaturized in size will significantly enhance technologies in various applications, such as mobile devices, wireless sensors, Integrated Circuit chips (ICs), microelectronics and biomedical implants.

7.2 Future Work

This dissertation has developed optimal and miniaturized SCMR systems for wireless power transmission. However, there are several areas that can be expanded by future research.

Our work focused on theoretical analysis and optimal design of SCMR systems. The SCMR systems were all tested using a VNA. Therefore, the source and load in our designs are the input and output of the VNA with the value of 50 Ohm. In many applications, the input power to the system comes from AC power, battery or DC supply. The AC/DC rectifier block and DC/RF convert block are needed to complete a WPT system. Also, a rectifier which converts the received AC power back into DC power for loads is needed. In addition, a power amplifier must be used. Therefore, impedance matching networks need to be further studied and designed in order to achieve high efficiency for the whole system. Also, the definition of the whole system's efficiency needs to be modified in order to fully describe the performance of the whole system.

Future work can also study on how to improve the range of SCMR systems. For example, metamaterials can be studied to determine if they can increase the range of SCMR systems.

In this dissertation, we developed several methods for the miniaturization design of SCMR systems. However, the efficiencies of some systems drop slightly as the operating frequencies shift to lower frequencies. Therefore, there are still some issues that can be explored in order to maximize trade-offs between power transfer efficiency and miniaturization. The research can be extended to the optimization of novel topologies that have less loss and higher Q-factor.

Finally, the study of multiband and broadband CSCMR systems can be extended to more applications, such as combining data transmission. In this way, powering devices and data communication could be realized through the same link simultaneously. Also, more work can be done on the miniaturized SCMR system for embedded sensing applications and biomedical devices. Given the safety level and other manufacture constraints, the miniaturized SCMR system can be further optimized for improved efficiency and compact size.

REFERENCES

[1] J. Agbinya, *Wireless Power Transfer*. River Publishers, Melbourne: 2012

[2] D. W. Baarman, "Making Wireless Truly Wireless: The Need for a Universal Wireless Power Solution," *Fulton Innovation*, 2009.

[3] A. Kurs, A. Karalis, R. Moffatt, J. Joannopoulos, P. Fisher, and M. Soljacic, "Wireless Power Transfer via Strongly Coupled Magnetic Resonances", *Science*, vol. 317, no. 5834, pp. 83-86, July 2007.

[4] F. Hadley, "MIT Demos Wireless Power Transmission". Techtalk Serving the MIT Community, vol.51, no. 30, June. 2007.

[5] V. Choudhary, A. Kadir, and S. P. Singh, "Wireless Power Transmission 'a Novel Idea'". *International Journal of Scientific & Engineering Research*, vol. 2, pp.1-6, Sept. 2011.

[6] A. Karalis, J. D. Joannopoulos, and M. Soljacic, "Efficient Wireless Non-radiative Mid-range Energy Transfer". *Annals of Physics*, vol. 323, pp.34-38, Jan. 2008.

[7] M. J. Sibakoti and J. Hambleton, "Wireless Power Transmission Using Magnetic Resonance,"[Online],http://www.cornellcollege.edu/physics/files/mandip-sibakoti.

[8] S. J. Mazlouman, A. Mahanfar, and B. Kaminska, "Mid-range Wireless Energy Transfer using Inductive Resonance for Wireless Sensors". *ICCD'09 Proceedings of the IEEE International Conference on Computer design*, pp.517-522, 2009.

[9] J. P. Lynch and K. J. Loh, "A Summary Review of Wireless Sensors and Sensor Networks for Structural Health Monitoring," *The Shock and Vibration Digest*, 38(2), pp. 91–128, 2006.

[10] D. Puccinelli and M. Haenggi, "Wireless Sensor Networks: Applications and Challenges of Ubiquitous Sensing," *Circuits and Systems Magazine, IEEE*, vol. 5, no. 3, pp. 19-31, 2005.

[11] M. Li and H. Lin, "Design and Implementation of Smart Home Control Systems based on Wireless Sensor Networks and Power Line Communications," *IEEE Trans. Ind. Electron.*, vol.62, no. 7, pp. 4430-4442, 2015

[12] K. M. Z. Shams and M. Ali, "Wireless Power Transmission to a Buried Sensor in Concrete," *IEEE J. Sensors*, vol. 7, no. 12, pp. 1573–1577, Dec. 2007.

[13] O. Jonah, S. V. Georgakopoulos, and M. M. Tentzeris, "Multiband Wireless Power Transfer via Resonance Magnetic," *2013 IEEE Antennas Propagat. Society Internat. Symp.*, Lake Buena Vista, FL, Jul. 7-12, 2013.

[14] M. Dionigi and M. Mongiardo, "Multi Band Resonators for Wireless Power Transfer and Near Field Magnetic Communications," *IEEE MTT-S International Microwave Workshop Series on Innovative Wireless Power Transmission: Technologies, Systems, and Applications (IMWS),* pp.61-64, May 10-11, 2012.

[15] A. P. Sample, D. T. Meyer, and J. R. Smith, "Analysis, Experimental Results, and Range Adaptation of Magnetically Coupled Resonators for Wireless Power Transfer". *IEEE Transactions on Industrial Electronics*, vol. 58, no. 2, pp. 544-554, 2011.

[16] B. L. Cannon, J. F. Hoburg, D. D. Stancil, and S. C. Goldstein, "Magnetic Resonant Coupling as a Potential Means for Wireless Power Transfer to Multiple Small Receivers". *IEEE Transactions on Power Electronics*, vol. 24, no. 7, Jul. 2009.

[17] O. Jonah, and S. V. Georgakopoulos, "Wireless Power Transmission to Sensors Embedded in Concrete via Magnetic Resonance," *IEEE 12th Annual Wireless and Microwave Technology Conference (WAMICON),* pp.1-6, Apr. 2011.

[18] D. Watters, P. Jayaweera, A. Bahr, and D. Huestis, "Design and Performance of Wireless Sensors for Structural Health Monitoring," [Online]: http://www.dot.ca.gov /newtech/ maintenance/docs/qnde.pdf.

[19] Y. P. T. Theilmann and P. M. Asbeck, "An Analytical Model for Inductively Coupled Implantable Biomedical Devices with Ferrite Rods". *IEEE Trans. Biomedical Circuits and Systems*, vol. 3, no. 1, Feb. 09.

[20] S. Kopparthi and P. K. Ajmera, "Power Delivery for Remotely Located Microsystems". *Proc. of IEEE Region 5, 2004 Annual Tech. Conference*, pp. 31-39, Apr. 2004.

[21] Y. Kim, J. Kim, and H. Lee, "Electrically Small Square Loop Antenna with a Capacitive SRR Cover Structure". *Microwave Conferenc, EuMC 2008. 38th European*, pp. 893-896, Oct. 2008.

[22] C. A. Balanis, *Antenna Theory: Analysis and Design*, 3rd. Hoboken, NJ: John Wiley & Sons, 2005.

[23] F. Bilotti, A. Toscano, and L. Vegni, "Design of Spiral and Multiple Split-Ring Resonators for the Realization of Miniaturized Metamaterial Samples". *IEEE. Trans. Antennas and Propagation*, vol.55, no.8, pp. 2258-2265, Aug. 2007.

[24] M. Lee, B. A. Kramer, C. Chen, and J. L. Volakis, "Distributed Lumped loads and Lossy Transmission Line Model for Wideband Spiral Antenna Miniaturization and Characterization". *IEEE. Trans. Antennas and Propagation*, vol.55, no.10, pp. 2671-2678, Oct. 2007.

[25] W. C. Brown, “The History of Power Transmission by Radio Waves,” *IEEE Transactions on Microwave Theory and Techniques*, vol. 32, no. 9, pp. 1230-1242, Sep. 1984.

[26] S. Ahson and M. Ilyas, *RFID Handbook: Applications, Technology, Security, and Privacy*. Boca Raton, FL: CRC Press, 2008.

[27] Y. Jang and M. M. Jovanovic, “A Contactless Electrical Energy Transmission System for Portable-telephone Battery Chargers,” *IEEE Trans. Ind. Electron.*, vol. 50, no. 3, pp. 520–527, Jun. 2003.

[28] J. Shin, S. Shin, Y. Kim, S. Ahn, S. Lee, G. Jung, S. Jeon, and D. Cho, “Design and Implementation of Shaped Magnetic-resonance-based Wireless Power Transfer System for Roadway-powered Moving Electric Vehicles,” *IEEE Trans. Ind. Electron.*, vol. 61, no. 3, pp. 1179-1192, Mar. 2014.

[29] W. X. Zhong, X. Liu, and S. Y. Hui, “A Novel Single-layer Winding Array and Receiver Coil Structure for Contactless Battery Charging Systems with Free-Positioning and Localized Charging Features,” *IEEE Trans. Ind. Electron.*, vol. 58, no. 9, pp. 4136–4144, Sep. 2011

[30] P. E. Glaser, "Power From the Sun: Its Future," *Science Magazine*, vol. 162, no. 3856, pp. 857–861, Nov. 22, 1968.

[31] P. E. Glaser, United States Patent 3781647, "Method and Apparatus For Converting Solar Radiation To Electrical Power," Dec. 25, 1973.

[32] W. C. Brown and E. E. Eves, "Beamed Microwave Power Transmission and Its Application to Space," *IEEE Transactions on Microwave Theory and Techniques*, vol. 40, no. 6, pp. 1239-1250, Jun. 1992.

[33] J. O. McSpadden and J. C. Mankins, "Space Solar Power Programs and Microwave Wireless Power Transmission Technology," in *IEEE Microwave Magazine*, vol. 3, no. 4, pp. 46-57, Dec. 2002.

[34] J. Benford, "Space Applications of High-Power Microwaves," in *IEEE Transactions on Plasma Science*, vol. 36, no. 3, pp. 569-581, Jun. 2008.

[35] M. Catrysse, B. Hermans, and R. Puers, “An Inductive Power System with Integrated Bi-directional Data-transmission,” *Sensors and Actuators A:Phys*ical, vol. 115, iss. 2-3, pp, 221–229, Sep. 21, 2004.

[36] J. C. Schuder, “Powering an Artificial Heart: Birth of the Inductively Coupled-Radio Frequency System in1960,” *Artificial Organs*, vol. 26, iss. 11, pp. 909-915, Nov.1, 2002.

[37] A. Sample and J. R. Smith, “Experimental Results with Two Wireless Power Transfer Systems,” *IEEE Radio and Wireless Symposium*, pp. 16-18, San Diego, CA, 2009.

[38] U. K. Madawala and D. J. Thrimawithana, “A Bidirectional Inductive Power Interface for Electric Vehicles in V2G systems,” *IEEE Transactions on Industrial Electronics*, vol. 58, iss. 10, pp. 4789-4796, 2011.

[39] Z. Wei, W. Siu-Chong, C. K. Tse, C. Qianhong, “Analysis and Comparison of Secondary Series- and Parallel-compensated Inductive Power Transfer Systems Operating for Optimal Efficiency and Load-independent Voltage-transfer Ratio,” *IEEE Transactions on Power Electronics,* vol. 29, iss. 6, pp. 2979–90, 2014.

[40] S. D. Barman, A. W. Reza, N. Kumar, M. E. Karim, and A. B. Munir, “Wireless Powering by Magnetic Resonant Coupling: Recent Trends in Wireless Power Transfer System and Its Applications,” *Renewable and Sustainable Energy Reviews 51*, pp. 1525-1552, 2015.

[41] X. Lu, P. Wang, D. Niyato, D. I. Kim, and Z. Han, "Wireless Charging Technologies: Fundamentals, Standards, and Network Applications," in *IEEE Communications Surveys & Tutorials*, vol. 18, no. 2, pp. 1413-1452, Secondquarter 2016.

[42] X. Wei, Z. Wang, and H. Dai, “A Critical Review of Wireless PowerTransfer via Strongly Coupled Magnetic Resonances,” *Energies*, vol. 7, no. 7, pp. 4316-4341, Jul. 2014.

[43] C. S. Wang, G. A. Covic, and O. H. Stielau, “Power Transfer Capability and Bifurcation Phenomena of Loosely Coupled Inductive Power Transfer Systems,” *IEEE Trans. Ind. Electron.*, vol. 51, no. 1, pp. 148-157, Feb. 2004.

[44] X. Lu, P. Wang, D. Niyato, D. I. Kim, and Z. Han, “Wireless Networks with RF Energy Harvesting: A Contemporary Survey,” *IEEE Communications Surveys and Tutorials*, vol. 17, no. 2, pp. 757-789, May 2015.

[45] A. Kurs, R. Karalis, M. Moffatt, and S. Marin, "Simultaneous Midrange Power to Multiple Devices". *Appl. Phys. Lett.* vol. 96, 044102, 2010.

[46] D. M. Pozar, *Microwave Engineering*, 4th edition. John Wiley &Sons, 2011.

[47] S. J. Orfanidis, *Electromagnetic Waves and Antennas* [online]. Available:http://www.ece.rutgers.edu/~orfanidi.ewa.

[48] IEEE, *IEEE Standard for Safety Levels with Respect to Human Exposure to Radio Frequency Electromagnetic Fields, 3 kHz to 300 GHz*, 2006, IEEE Std C95.1-2005.

[49] IEEE, *IEEE Recommended Practice for Measurements and Computations of Radio Frequency Electromagnetic Fields With Respect to Human Exposure to Such Fields, 100 kHz-300 GHz*, IEEE Std C95.3-2002.

[50] "Evaluating Compliance With FCC Guidelines for Human Exposure to Radio Frequency Electromagnetic Fields," *Federal Communications Commission (FCC)*, Washington, DC, 1997, Tech. Rep. OET Bull. 65.

[51] D. C. Ng, X. Wang, G. K. Felic, S. Bai, C. S. Boyd, M. Halpern and E. Skafidas , "Specific Absorption Rate Distribution on a Human Head Model from Inductive Power Coils," *EMC Europe 2011 York* , pp.79-83, Sep. 26-30, 2011.

[52] M. Kesler, "Highly Resonant wireless power transfer: safe, efficient, and over distance," *WiTricity Corporation*, 2013.

[53] J. Hartford, "Wireless Power for Medical Devices", *Electronic Components* [online], Jun. 20, 2013.

[54] "Wireless Electric Charging: The Future of Plug-In Electric Vehicles is Going Cordless," *Office of Energy Efficiency and Renewable Energy,* http://energy.gov/ [online], Mar. 7, 2016.

[55] C. Morris, "WAVE Wireless Charging Helps Transit Agencies Save Money by Going Electric", *Charge Electric Vehicles Magazine,* Apr. 25, 2016.

[56] S. Cheon, Y. Kim, S. Kang, M. L. Lee, J. Lee, and T. Zyung, "Circuit-model-based Analysis of a Wireless Energy-transfer System via Coupled Magnetic Resonances," *IEEE Trans. Ind. Electron.*, vol. 58, no. 7, pp. 2906–2914, Jul. 2011.

[57] H. Hu and S. V. Georgakopoulos, "Wireless Powering based on Strongly Coupled Magnetic Resonance with SRR Elements," *IEEE Antennas Propagat. Society Internat. Symp.*, Chicago, IL, Jul. 8-13, 2012.

[58] T. C. Beh, M. Kato, T. Imura, S. Oh, and Y. Hori, "Automated Impedance Matching System for Robust Wireless Power Transfer via Magnetic Resonance Coupling," *IEEE Trans. Ind. Electron.*, vol. 60, no. 9, pp. 3689-3698, Sep. 2013.

[59] Q. Zhu, L. Wang, and C. Liao, "Compensate capacitor optimization for kilowatt-level magnetically resonant wireless charging system," *IEEE Trans. Ind. Electron.*, vol. 61, no. 12, pp. 6758-6768, Dec. 2014.

[60] D. Ahn and S. Hong, "Wireless Power Transfer Resonance Coupling Amplification by Load-modulation Switching Controller," *IEEE Trans. Ind. Electron.*, vol. 62, no. 2, pp. 898-909, Feb. 2015.

[61] D. Ahn and S. Hong, “A Transmitter or a Receiver Consisting of Two Strongly Coupled Resonators for Enhanced Resonant Coupling in Wireless Power Transfer,” *IEEE Trans. Ind. Electron*., vol. 61, no. 3, pp. 1193-1203, Mar. 2014.

[62] T. Imura and Y. Hori, “Maximizing Air Gap and Efficiency of Magnetic Resonant Coupling for Wireless Power Transfer using Equivalent Circuit and Neumann Formula,” *IEEE Trans. Ind. Electron.*, vol. 58, no. 10, pp. 4746– 4752, Oct. 2011.

[63] W. Lee, W. Son, K. Oh, and J. Yu, “Contactless Energy Transfer Systems using Antiparallel Resonant Loops,” IEEE Trans. Ind. Electron., vol. 60, no. 1, pp. 350–359, Jan. 2013.

[64] D. Ahn and S. Hong, “A Study on Magnetic Field Repeater in Wireless Power Transfer,” *IEEE Trans. Ind. Electron.*, vol. 60, no. 1, pp. 360–371, Jan. 2013.

[65] W. Zhong, C. K. Lee, and S.Y.R. Hui, “General Analysis on the Use of Tesla's Resonators in Domino Forms for Wireless Power Transfer,” *IEEE Trans. Ind. Electron.*, vol. 60, no. 1, pp. 261-270, Jan. 2013.

[66] R. Johari, J. V. Krogmeier, and D. J. Love, "Analysis and Practical Considerations in Implementing Multiple Transmitters for Wireless Power Transfer via Coupled Magnetic Resonance," *IEEE Trans. Ind. Electron.*, vol. 61, no. 4, pp. 1774-1783, Apr. 2014

[67] D. Ahn and S. Hong, “Effect of Coupling between Multiple Transmitters or Multiple Receivers on Wireless Power Transfer,” *IEEE Trans. Ind. Electron.*, vol. 60, no. 7, pp. 2602–2613, Jul. 2013.

[68] M. Kiani and M. Ghovanloo, "The Circuit Theory Behind Coupled-Mode Magnetic Resonance-Based Wireless Power Transmission," *IEEE Trans. Circuits Syst. I, Reg. Papers,* vol. 59, no. 9, pp. 2065-2074, Sept. 2012.

[69] O. Jonah, S. V. Georgakopoulos, and M. M. Tentzeris, “Strongly Coupled Wireless Power Transfer with Conformal Structures,” *29th Annual Review of Progress in Applied Comput. Electromagnetics,* Monterey, CA, Mar. 24-28, 2013

[70] O. Jonah, S. V. Georgakopoulos, and M. M. Tentzeris, “Optimal Design Parameters for Wireless Power Transfer by Resonance Magnetic,” *IEEE Antennas Wireless Propag. Lett.*, vol.11, pp. 1390-1393, 2012.

[71] S. Ramo, J. R. Whinnery, and T. V. Duzer, *Fields and Waves in Communication Electronics*, 3rd. New York: John Wiley & Sons, 1994.

[72] F. W. Grover, *Inductance Calculations*. New York: Dover, 1962.

[73] S. Liao, P. Dourmashkin, and J. Belcher, Visualizing Electromagnetism, *MIT Class Note* [Online]. Available: http://web.mit.edu/viz/EM/visualizations/notes.

[74] C. T.-C. Nguyen, "Communications Applications of Micromechanical Systems," *Proceedings, 1998 Sensors Expo*, pp.447-455, San Jose, CA, May 19-21,1998.

[75] M. A. G. Darrin, B. G. Carkhuff, and T. S. Mehoke, "Future Trends in Miniaturization for Wireless Applications, " *Johns Hopkins APL Technical Digest*, vol. 25, no. 4, 2004.

[76] J. Kim, A. Banks, Z. Xie, S. Y. Heo, P. Gutruf, J. W. Lee, S. Xu, K.-I. Jang, F. Liu, G. Brown, J. Choi, J. H. Kim, X. Feng, Y. Huang, U. Paik, and J. A. Rogers, "Miniaturized Flexible Electronic Systems with Wireless Power and Near-Field Communication Capabilities," *Advanced Functional Materirals*, vol. 25, iss. 30, pp: 4761–4767, Aug. 12, 2015.

[77] K. Bao, H. Hu, and S. V. Georgakopoulos, "Design Considerations of Conformal SCMR System," *IEEE Wireless Power Transfer Conference 2015*, Boudler, Colorado, May 13-15, 2015.

[78] H. Hu and S. V. Georgakopoulos, "Wireless Powering based on Strongly Coupled Magnetic Resonance with SRR Elements," *IEEE Antennas Propagat. Society Internat. Symp.*, Chicago, IL, Jul. 8-13, 2012.

[79] F. E. Terman, *Radio Engineers' Handbook*. New York and London: McGraw-Hill Book Company, 1st edition, 1943.

[80] O. Jonah, and S.V. Georgakopoulos, "Wireless Power Transmission to Sensors Embedded in Concrete via Magnetic Resonance," *IEEE 12th Annual Wireless and Microwave Technology Conference (WAMICON)*, pp.1-6, 18-19 Apr. 2011.

[81] J. D. Baena, J. Bonahce, F. Martin, R. M. Sillero, F. Falcone, T. Lopetegi, M. A. G. Laso, J. Garcia-Garcia, I. Gil, M. F. Portillo, and M. Sorolla, "Equivalent-circuit Models for Split-ring Resonators and Complementary Split-ring Resonators Coupled to Planar Transmission Lines," *IEEE Trans. Microwave Theory & Tech.*, vol. 53, no4, pp. 1451-1461, Apr. 2005.

[82] T. Akin, K. Najafi, and R. Bradley, "A Wireless Implantable Multichannel Digital Neural Recording System for a Micromachined Sieve Electrode," *IEEE J. Solid-State Circuits*, vol. 33, pp. 109–118, 1998.

[83] A. Yakovlev, K. Sanghoek, and A. Poon, "Implantable Biomedical Devices: Wireless Powering and Communication," *Communications Magazine, IEEE* , vol.50, no.4, pp.152,159, Apr. 2012.

[84] B. Lenaerts and R. Puers, "An Inductive Power Link for a Wireless Endoscope," *Biosens. Bioelectron.*, vol. 22, pp. 1390–1395, 2007.

[85] S. Gabriel, R. Lau, and C. Gabriel, "The DielectricP of Biological Tissues: III. Parametric Models for the Ddielectric Spectrum of Tissues," *Phys. Med. Biol.*, vol. 41, pp. 2271–2293, 1996.

[86] A. N. Laskovski, T. Dissanayake, and M. R. Yuce, *Wireless Power Technology for Biomedical Implants, Biomedical Engineering*, InTech, 2009.

[87] R. Bashirullah, "Wireless Implants," in *IEEE Microw. Mag.s*, pp. 14–23, Dec. 2010.

[88] A. K. RamRakhyani and G. Lazzi, "On the Design of Efficient Multi-Coil Telemetry System for Biomedical Implants," *Biomedical circuits and systems, IEEE Transactions on*, vol. 7, no. 1, pp. 11-23, Feb. 2013.

[89] M. V. Sarma, V. Ilankumaran, and N. S. Rao. "Trends in Cardiac Pacemaker Batteries," *Indian pacing and electrophysiology Journal.*, Oct. 2004.

[90] A. Yakovlev, K. Sanghoek and A. Poon, "Implantable Biomedical Devices: Wireless Powering and Communication," *IEEE Communications Magazine*, vol.50, no.4, pp.152-159, Apr. 2012.

[91] R. Xue, K. Cheng, and M. Je, "High-Efficiency Wireless Power Transfer for Biomedical Implants by Optimal Resonant Load Transformation," *Circuits and Systems I: Regular Papers, IEEE Transactions on* , vol.60, no.4, pp.867,874, Apr. 2013.

[92] K. Van Schuylenbergh and R. Puers, *Inductive Powering: Basic Theory and Application to Biomedical Systems*. New York: Springer Science.

[93] Z. Yang, W. Liu, and E. Basham, "Inductor Modeling in Wireless Links for Implantable Electronics," *IEEE Trans. Magn.*, vol. 43, no. 10, pp. 3851–3860, Oct. 2007.

VITA

HAO HU

1984	Born, Shaanxi, China.
2002	B. E. Electronic & Information Engineering Xi'an Jiaotong University Xi'an, China
2006	M. S., Electronic & Information Engineering Xi'an Jiaotong University Xi'an, China
2011	Ph. D. Candidate, Electrical Engineering Florida International University Miami, Florida

PUBLICATIONS AND PRESENTATIONS

[1] Hao Hu and Stavros V. Georgakopoulos, "Multiband and Broadband Wireless Power Transfer Systems using the Conformal Strongly Coupled Magnetic Resonance Method*," IEEE Transactions on Industrial Electronics*, no. 99, May, 2016

[2] Daerhan Liu, Hao Hu, and Stavros V. Georgakopoulos, "Misalignment Sensitivity of Strongly Coupled Wireless Power Transfer Systems", *IEEE Transactions on Power Electronics*, no.99, Sep. 2016.

[3] Hao Hu and Stavros V. Georgakopoulos, "Miniaturization Design of SCMR Systems for Wireless Power Transmission", *IEEE microwave and communication letters* (to be submitted).

[4] Hao Hu, Daerhan Liu and Stavros V. Georgakopoulos, "Miniaturized Strongly Coupled Magnetic Resonant Systems for Wireless Power Transfer," *IEEE Antennas and Propagation Society International Symposium*, Fajardo, Puerto Rico, Jun. 26-30, 2016.

[5] Hao Hu and Stavros V. Georgakopoulos, "Wireless Powering of Biomedical Implants by Conformal Strongly Coupled Magnetic Resonators," *IEEE Antennas and Propagation Society International Symposium*, Vancouver, BC, Canada, Jul. 19-25, 2015.

[6] Hao Hu, Shun Yao, Kun Bao, and Stavros V. Georgakopoulos, "Misalignment Insensitive WPT with Conformal SCMR Systems," *IEEE Antennas and*

Propagation Society International Symposium, Vancouver, BC, Canada, Jul. 19-25, 2015.

[7] Hao Hu and Stavros V. Georgakopoulos, “Wireless Power Transfer in Human Tissue via Conformal Strongly Coupled Magnetic Resonance,” *IEEE Wireless Power Transfer Conference 2015*, Boudler, Colorado, May 13-15, 2015.

[8] Hao Hu, Stavros V. Georgakopoulos, and Kun Bao, “Optimal Conformal SCMR Wireless Power Transfer Systems in Human Tissue,” *16th Annual IEEE Wireless and Microwave Technology Conference*, Cocoa Beach, FL, Apr. 13-15, 2015.

[9] Hao Hu and Stavros V. Georgakopoulos, "Analysis and Design of Conformal SCMR WPT Systems with Multiple Resonators", *IEEE Antennas and Propagation Society International Symposium*, Memphis, TN, Jul. 6-12, 2014.

[10] Hao Hu and Stavros V. Georgakopoulos, "Design of Optimal and Broadband Conformal SCMR Systems", *IEEE Antennas and Propagation Society International Symposium*, Memphis, TN, Jul. 6-12, 2014.

[11] Hao Hu and Stavros V. Georgakopoulos, "Analysis and Design of Broadband Wireless Power Transmission System via Conformal Strongly Coupled Magnetic Resonance," *15th Annual IEEE Wireless and Microwave Technology Conference*, Tampa Bay, FL, Jun. 6, 2014.

[12] Hao Hu, Kun Bao, John Gibson and Stavros V. Georgakopoulos, "Printable and Conformal Strongly Coupled Magnetic Resonant Systems for Wireless Powering," *15th Annual IEEE Wireless and Microwave Technology Conference*, Tampa Bay, FL, Jun. 6, 2014.

[13] Hao Hu and Stavros V. Georgakopoulos, "Wireless Power Transfer Through Strongly Coupled Electric Resonance," *IEEE Antennas and Propagation Society International Symposium*, Lake Buena Vista, FL, Jul. 7-12, 2013.

[14] Hao Hu and Stavros V. Georgakopoulos, “Optimal Design of Conformal Strongly Coupled Magnetic Resonant Systems,” *30th Annual Review of Progress in Applied Computational Electromagnetics*, Jacksonville, FL, Mar. 23–27, 2014.

[15] Hao Hu and Stavros V. Georgakopoulos, “Miniaturized Strongly Coupled Magnetic Resonance Design based on Dielectric Split-ring Resonator for Wireless Power Transmission,” *29th Annual Review of Progress in Applied Computational Electromagnetics*, Monterey, CA, Mar. 24-28, 2013.

[16] Hao Hu and Stavros V. Georgakopoulos, “Wireless Powering based on Strongly Coupled Magnetic Resonance with SRR Elements,” *IEEE Antennas and Propagation Society International Symposium*, Chicago, IL, Jul. 8-13, 2012.